

**ELECTRIC BREAKDOWN AND IONIZATION  
DETECTION IN NORMAL LIQUID AND  
SUPERFLUID  $^4\text{He}$  FOR THE SNS nEDM  
EXPERIMENT**

Maciej Karcz

Submitted to the faculty of the University Graduate School  
in partial fulfillment of the requirement  
for the degree  
Doctor of Philosophy  
in the Department of Physics,  
Indiana University

August 2014

UMI Number: 3634313

All rights reserved

INFORMATION TO ALL USERS

The quality of this reproduction is dependent upon the quality of the copy submitted.

In the unlikely event that the author did not send a complete manuscript and there are missing pages, these will be noted. Also, if material had to be removed, a note will indicate the deletion.



UMI 3634313

Published by ProQuest LLC (2014). Copyright in the Dissertation held by the Author.

Microform Edition © ProQuest LLC.

All rights reserved. This work is protected against unauthorized copying under Title 17, United States Code



ProQuest LLC.  
789 East Eisenhower Parkway  
P.O. Box 1346  
Ann Arbor, MI 48106 - 1346

Accepted by the Graduate Faculty, Indiana University, in partial fulfillment of the requirement for the degree of Doctor of Philosophy.

Doctoral  
Committee

---

Chen-Yu Liu, Ph.D. (Chairperson)

---

Joshua C. Long, Ph.D. (Co-Chair)

---

Charles J. Horowitz, Ph.D.

---

W. Michael Snow, Ph.D.

June 9, 2014

---

Scott W. Wissink, Ph.D.

Copyright ©2014 by  
Maciej Karcz

## Acknowledgements

First and foremost I would like to thank my advisor, Dr. Chen-Yu Liu. Dr. Liu's enthusiasm and energy have been an inspiration to me again and again. Her patience, exuberant perspective and capacity for sharp insight have created a research environment that I will sorely miss. I also wish to thank my co-advisor, Dr. Josh Long. Dr. Long's tenacious and thorough approach to research have made an indelible impression on me. I can only hope to emulate some of the great spirit that Drs. Liu and Long have always demonstrated around me.

I would also like to express my gratitude to the great technical staff in ISAT and Swain Halls. John Vanderwerp for the myriad help around the lab over the years. Dr. Bill Lozowski for the careful instruction in electron beam evaporation, interesting discussions and a tiny fraction of his encyclopedic chemistry experience. Dr. Keith Solberg for his helpful discussions and analysis of my ionization chamber concept. Phil Childress and the machine shop team for their very impressive fabrication skills and experience.

I had the distinct pleasure to work alongside great colleagues. Dr. Adam Holley with whom I have had so many thought-provoking discussions and whose extraordinary writing skills always fascinated me. I have also benefited greatly from Dr. Holley's help with the dilution refrigerator and neutron experiments. I also received various help around the lab from Young Jin Kim with whom I also had the pleasure of carrying on a tradition spanning several years of afternoon tea accompanied by stimulating discussions. Over the years I have enjoyed working with various talented undergraduates: Craig Huffer, Alex Jacobs, Thomas Nevitt, Kyle Kaericher, Andrew Peckat and Thomasina O'Connor.

I am grateful to my best friend since childhood, Yevgeny Binder, who inspired me with physics and math. I always recall with pleasure our 8<sup>th</sup> grade discussions about cosmology, relativity and calculus that frequently landed us in trouble with teachers. Fortunately back then, a la Mark Twain, we did not let school interfere with our education, but I think some of those library books may still have sand in them.

I am also grateful to the many terrific friends from the Indiana University Badminton Club: Raymond, Vichea, Ding, Chunfeng, Jayne, Soumya, Ivy, Michael L., Hui-Jung for much joy on and off the court.

I wish to thank my fiancé Dr. Tianhuan Luo for her companionship, support and patience.

Finally, I wish to thank my family for their unyielding patience and support over the years.

Maciej Karcz

# ELECTRIC BREAKDOWN AND IONIZATION DETECTION IN NORMAL LIQUID AND SUPERFLUID $^4\text{He}$ FOR THE SNS nEDM EXPERIMENT

A new experiment to search for the neutron electric dipole moment (nEDM) is under construction at the Spallation Neutron Source (SNS) at Oak Ridge National Laboratory. The SNS nEDM experiment is a national collaboration spanning over 20 universities and laboratories with more than 100 physicists and engineers contributing to the research and development. The search for a nEDM is a precision test of time reversal symmetry in particle physics, in the absence of a discovery, the SNS nEDM experiment seeks to improve the present limit on the nEDM value by two orders of magnitude. A non-zero value of the nEDM would help to explain the asymmetry between matter and anti-matter in the universe by providing an additional source of charge conjugation and parity symmetry violation, a necessary ingredient in the theory of baryogenesis in the early universe.

The nEDM experiment will measure the Larmor precession frequency of neutrons by detecting scintillation from neutron capture by a dilute concentration of  $^3\text{He}$  inside a bath of superfluid  $^4\text{He}$ . Neutron capture by  $^3\text{He}$  is spin-dependent and the magnetic moments of the neutron and the  $^3\text{He}$  nucleus are comparable. A direct measurement of the precession frequency of polarized  $^3\text{He}$  and scintillation from neutron capture allows for the relative precession frequencies of  $^3\text{He}$  and the neutron to be determined. The experiment will then look for changes in the relative precession of  $^3\text{He}$  and neutrons under the influence of strong electric fields.  $^3\text{He}$  has negligible EDM and therefore any deviation due to an applied electric field would be from a nEDM.

The nEDM experiment will need to apply strong electric fields inside superfluid

$^4\text{He}$  and it was necessary to investigate the ability of superfluid (SF)  $^4\text{He}$  to sustain electric fields. An experiment to study electric breakdown in superfluid  $^4\text{He}$  was constructed at the Indiana University Center for Exploration of Energy and Matter (CEEM). The experiment studied the electric breakdown behavior of liquid Helium throughout the pressure-temperature phase space, between 1 bar and the saturation curve and between 4.2 K and 1.7 K. A new breakdown hysteresis in liquid helium was discovered and is attributed to the suppression of heterogeneous nucleation sites inside the liquid. A phenomenological model involving the Townsend breakdown mechanism and Paschen's Law in liquid helium is proposed.

In addition, the many challenges faced by efficient scintillation detection in the cryogenic environment of the nEDM experiment motivated additional studies at CEEM. To test the effect of an electric field on scintillation in superfluid, a SF test cell was constructed inside a dilution refrigerator and it was found that the scintillation intensity from a  $^{241}\text{Am}$  source in the cell, is reduced at high electric fields. Alternatives to scintillation detection for the nEDM experiment were also explored and the test cell was reconfigured to operate as a superfluid ionization chamber. The superfluid ionization chamber was tested with  $^{241}\text{Am}$  in pulse mode and current mode configurations. While the pulse mode in superfluid, which relies on the drift velocity of charges, is hindered by quasi-particle excitations in superfluid, results of current mode measurements appear promising.

To further explore the prospect of cryogenic ionization detection, a detector cryostat capable of detecting neutrons using a  $^{10}\text{B}$  converter was also constructed at CEEM and tested at the Indiana University Low Energy Neutron Source (LENS). The neutron detector cryostat has the benefit of being able to modulate the ionization source which was not possible with the superfluid ionization chamber. Tests with argon gas led to the development of more efficient boron targets. The cryogenic test of ionization detection in current mode will be discussed.



# Contents

<b>Acceptance</b>	<b>ii</b>
<b>Acknowledgments</b>	<b>iv</b>
<b>Abstract</b>	<b>vi</b>
<b>1 Introduction</b>	<b>1</b>
<b>2 Symmetries</b>	<b>3</b>
2.1 Symmetries in Nuclear Physics . . . . .	3
2.1.1 Parity . . . . .	4
2.1.2 Charge Conjugation . . . . .	5
2.1.3 Time-reversal symmetry . . . . .	5
2.2 Symmetry Violation . . . . .	7
2.2.1 Observations of symmetry violation . . . . .	7
2.2.2 Baryogenesis . . . . .	7
2.2.3 Particle Electric Dipole Moments . . . . .	9
2.3 nEDM in the Standard Model and New Physics . . . . .	11
2.4 nEDM Experiments . . . . .	13
2.4.1 Separated Oscillatory Fields Method . . . . .	15
2.4.2 Neutron Beam Experiments . . . . .	16
2.4.3 Ultracold Neutron Storage Experiments . . . . .	19
<b>3 The SNS nEDM Experiment</b>	<b>23</b>
3.1 The Search for nEDMs . . . . .	23
3.2 SNS nEDM Experiment . . . . .	25
3.2.1 High voltage in the SNS nEDM . . . . .	32

---

<b>4</b>	<b>Electric Breakdown in Normal Liquid and Superfluid Helium</b>	<b>34</b>
4.1	High Voltage in the SNS nEDM Experiment . . . . .	34
4.2	Liquid Helium & Superfluidity . . . . .	35
4.3	Electric Breakdown in Gases . . . . .	41
4.3.1	Paschen law of breakdown . . . . .	46
4.4	Nucleation theory . . . . .	48
4.4.1	Heat transfer hysteresis . . . . .	49
4.4.2	Nucleation, wetting & pre-breakdown . . . . .	51
4.5	Apparatus . . . . .	60
4.6	Breakdown in helium gas . . . . .	69
4.7	Electric Breakdown in Liquid Helium . . . . .	82
4.8	Procedure . . . . .	86
4.8.1	System Preparation and Cooling . . . . .	86
4.8.2	Pressure and Temperature Control in the $^4\text{He}$ Phase Space . .	87
4.8.3	High Voltage Measurements . . . . .	92
4.9	Results & Discussion . . . . .	93
4.9.1	Electric Breakdown Hysteresis . . . . .	93
4.9.2	Pressurization Cycle in He-I . . . . .	97
4.9.3	Agitated Superfluid . . . . .	98
4.9.4	Wetting Transition in Superfluid . . . . .	103
4.9.5	Paschen trends in liquid helium . . . . .	105
4.10	Discussion . . . . .	111
<b>5</b>	<b>Liquid Helium Ionization Detection</b>	<b>118</b>
5.1	nEDM Cell as Ionization Chamber . . . . .	118
5.1.1	Charged particle interactions with matter . . . . .	119
5.1.2	Energy loss in matter . . . . .	120

---

5.2	Ions and electrons in liquid Helium . . . . .	121
5.3	Design . . . . .	126
5.3.1	The dilution refrigerator . . . . .	127
5.3.2	Operation of the CF650 Dilution Refrigerator . . . . .	131
5.3.3	Test chamber . . . . .	134
5.3.4	Test chamber gas handling & liquefaction . . . . .	140
5.4	Signal generation . . . . .	143
5.5	Simulated ionization pulse distribution . . . . .	148
5.6	Interface for pulse acquisition . . . . .	153
5.7	Gas ionization measurements . . . . .	154
5.7.1	Helium gas ionization current . . . . .	158
5.7.2	Pulse mode in gas . . . . .	162
5.8	Liquid Helium Ionization Current . . . . .	167
5.9	Discussion . . . . .	168
<b>6</b>	<b>Neutron Detection Cryostat</b>	<b>171</b>
6.1	Low Energy Neutron Source . . . . .	171
6.2	Design . . . . .	173
6.3	Neutron transmission of ionization cell . . . . .	182
6.4	Gas-based pulse mode neutron detection . . . . .	188
6.5	Liquid-based ionization detection . . . . .	193
6.6	Discussion & prospects . . . . .	194
<b>7</b>	<b>Concluding remarks</b>	<b>197</b>
	<b>References</b>	<b>203</b>
	<b>Curriculum Vita</b>	

# Chapter 1

## Introduction

The investigations described here were part of the research and development for the neutron electric dipole moment experiment being constructed at the Spallation Neutron Source at Oak Ridge National Laboratory (SNS nEDM experiment). The document is organized as follows:

The scientific motivation behind the nEDM experiment is described in Chapter 2. The importance of EDM searches is also highlighted. Chapter 3 gives an overview of the SNS nEDM experiment and defines the motivation behind the particular investigations described in subsequent chapters. Studies of electric breakdown in liquid helium at Indiana University are described in Chapter 4. Measurements of breakdown in He-I/He-II and also He vapor are discussed. The impact of the results on the nEDM experiment is also covered. A phenomenological model for breakdown in the liquid/vapor helium system is presented. Chapter 5 describes efforts to investigate ionization detection in liquid helium at low temperature. A drift chamber with *in situ*  $\alpha$  particle source mounted inside a dilution refrigerator is operated in pulse and current modes. Chapter 6 covers the development of a cryostat for neutron detection as a more accurate model of the nEDM system since the lower  $Q$ -value is a better

approximation of the energy output of  $n$ - $^3\text{He}$  absorption in the nEDM. The experiment has the important advantage, compared with chamber described in Chapter 5, of operating in a neutron beam line and thus the source can be modulated. Finally Chapter 7 offers concluding remarks as well as some reflections on the experiments of Chapters 4-6. The prospects of each investigation are also discussed in the frame of their respective fields.

## Chapter 2

# Symmetries

Hermann Weyl, in his book *Symmetry*, remarked “As far as I see, all a priori statements in physics have their origin in symmetry.” [1]. Indeed there exists among physicists an acquired tendency to regard systems with apparent symmetry as naturally simple or elegant. Symmetries in dynamic systems have also played an important role in our understanding of Nature. The presence of a symmetry in a physical system can lead to laws of conservation and conserved quantities which can simplify analysis such as conservations of charge, momentum, and probability to name a few. It is therefore a worthwhile endeavor to understand the nature of symmetry through experiments with symmetry in Nature.

### 2.1 Symmetries in Nuclear Physics

Arguably the most eloquent and pervasive application of symmetry principles can be found in particle physics. Symmetries in particle physics are rigorous and aesthetic expressions of pattern at the most fundamental level of Nature. Symmetries at this level also give rise to quantum numbers and selection rules for transitions between

states.

### 2.1.1 Parity

The parity transformation is a reflection of all coordinates of a system through the origin, e.g., in spherical coordinates this means

$$P(r, \theta, \phi) \longrightarrow (r, \pi - \theta, \pi + \phi) . \quad (2.1)$$

A system which is invariant under parity is said to be indistinguishable from its mirror-reflected counterpart. The parity transformation is typically denoted by  $P$  and it is Hermitian:  $P = P^\dagger$ , i.e.,  $P$  is equal to its complex conjugate transpose.  $P$  is a conserved quantum number if  $[P, H] = 0$ , where  $H$  is the Hamiltonian energy operator.

In general, for a state function  $\psi$ ,

$$P\psi(\mathbf{r}, t) = \eta_P \psi(-\mathbf{r}, t) \quad (2.2)$$

where  $\eta_P = \pm 1$  if the state is bosonic and  $\eta_P = \pm 1, \pm i$  if the state is fermionic. For bosonic systems, two successive  $P$  transformations return the original state whereas for fermionic systems four successive  $P$  transformations are required to obtain the original state.

In quantum field theory one acquires an additional matrix term:

$$P\psi(\mathbf{r}, t) = \eta_P \gamma^0 \psi(-\mathbf{r}, t) , \quad (2.3)$$

and for the positive and negative energy spinors

$$Pu = \eta_P \gamma^0 u = \eta_P u \quad (2.4)$$

$$Pv = \eta_P \gamma^0 v = -\eta_P v . \quad (2.5)$$

From Eqs. 2.4, 2.5 it follows that a particle and its antiparticle have opposite parities.

### 2.1.2 Charge Conjugation

Charge conjugation, or particle-anti-particle conjugation, is the transformation which interchanges a particle with its anti-particle. In addition to reversing the sign of the charge of the particle, additive quantum numbers, such as lepton or baryon number, are also reversed. Essentially, charge conjugation symmetry is the principle that particles and their respective anti-particles behave identically apart from the reversed charge and quantum numbers such as baryon number [2]. In this way, a universe made entirely of anti-matter would be indistinguishable from a universe made entirely of matter. It is for this reason that the choice of name for matter and anti-matter is completely arbitrary. The effect of  $C$  on a state with momentum  $\mathbf{p}$ , spin  $s$  and charge  $q$  is [2]

$$C|q, \mathbf{p}, s\rangle = \eta_C | -q, \mathbf{p}, s\rangle \quad (2.6)$$

where  $\eta_C$  is a phase factor.

In quantum field theory,  $C$  transforms field operators which create particles into operators which create anti-particles and vice versa [2]:

$$C\phi(t, \mathbf{x})\phi_C(t, \mathbf{x}) = \eta_C\phi^\dagger(t, \mathbf{x}) \quad (2.7)$$

where  $\phi$  is a charged scalar field and  $\phi_C$  its charge conjugate field. And in general

$$C^\dagger\phi(t, \mathbf{x})C = \eta_C\phi^\dagger(t, \mathbf{x})$$

$$C^\dagger\phi^\dagger(t, \mathbf{x})C = \eta_C^*\phi(t, \mathbf{x}) .$$

### 2.1.3 Time-reversal symmetry

The time reversal operation  $T : t \rightarrow -t$  is the inversion of the time coordinate. Classically, the  $T$  operation means that for any allowed motion of a dynamic system there exists a motion in which the same sequence of events is traversed in the opposite



order [2].  $T$  reverses the dynamic parameters of a system such as momentum and angular momentum, reversing the trajectory through configuration space.

In quantum mechanics  $T$  is anti-unitary, acting on a wavefunction  $T\psi(\mathbf{r}, t) = \psi^*(\mathbf{r}, -t)$ . The application of  $T$  twice reverts to the original system and for a system with  $n$  spin-1/2 particles

$$T^2|x_1, s_1; \dots; x_n, s_n\rangle = (-1)^n|x_1, s_1; \dots; x_n, s_n\rangle. \quad (2.8)$$

If  $|E\rangle$  and  $T|E\rangle = |E_T\rangle$  are eigenstates with the same eigenvalue of a system consisting of an odd number of fermions which is invariant under  $T$  then  $|E\rangle$  and  $|E_T\rangle$  are orthogonal. This is known as Kramer's theorem and can be stated

$$\langle E|E_T\rangle = \langle E_T|T^\dagger T|E\rangle = \langle E|(T^\dagger)^2 T|E\rangle = -\langle E|T|E\rangle \quad (2.9)$$

$$\implies \langle E|T|E\rangle = 0. \quad (2.10)$$

Thus  $E$  and  $E_T$  are degenerate and describe different physical states which means that there is an internal degree of freedom that is affected by  $T$  [3]. This holds only for systems with an odd number of fermions and not for systems with  $T^2$  eigenvalue  $+1$ . This property of  $T$  symmetry is used as a sensitive probe of electronic states of paramagnetic crystals with odd numbers of electrons since the degeneracy is lifted when electrons interact with an external magnetic field since it is not  $T$  invariant.

The combined operation  $CPT$  is thought to be an exact symmetry of Nature and quantum field theory is built on this assumption. Any system which is acted upon by all three symmetry operations  $CPT$  is thought to be unchanged; this is known as the  $CPT$  theorem. Since the combined symmetry is thought to be an invariant of Nature, when a system violates one part, e.g.  $CP$ , then it must also violate the remaining part, e.g.  $T$ , so that the combined  $CPT$  remains intact.

## 2.2 Symmetry Violation

Any statement of physical symmetry must be verifiable using experiment. There are some symmetries which are not always true except for certain classes of physical systems such as conservation of baryon or lepton numbers.

### 2.2.1 Observations of symmetry violation

In 1956, Lee and Yang [4] called for verification of parity conservation in the weak interaction by proposing several possible experiments. One such experiment was carried out by Wu [5] using the decay of  ${}^{60}_{27}\text{Co} \rightarrow {}^{60}_{28}\text{Ni} + e^- + \bar{\nu}_e + 2\gamma$ . Wu found that electrons were emitted preferentially antiparallel to the spin of  ${}^{60}\text{Co}$ .

First experimental evidence for  $C$  violation appeared together with  $P$  violation also in 1957 [6]. The close relationship between  $C$  and  $P$  symmetries, by the  $CPT$  theorem, meant that  $C$  and  $P$  violation often appeared together [2].

Most tests of  $T$  symmetry violation have been indirect insofar as  $T$  violation was implied when  $CP$  violation was detected. It was not until 1998 that  $T$  violation was observed directly [7] by the CPLEAR collaboration at CERN which found an asymmetry in the decay rates of neutral Kaons

$$\frac{\Gamma(\bar{K}^0 \rightarrow e^+\pi^-\nu_e) - \Gamma(K^0 \rightarrow e^-\pi^+\bar{\nu}_e)}{\Gamma(\bar{K}^0 \rightarrow e^+\pi^-\nu_e) + \Gamma(K^0 \rightarrow e^-\pi^+\bar{\nu}_e)} = (6.6 \pm 1.3 \pm 1.0) \times 10^{-3}, \quad (2.11)$$

which measures the effective value of the oscillation  $K^0 \rightarrow \bar{K}^0$  relative to the reversed process.

### 2.2.2 Baryogenesis

Baryogenesis is the name given to the process in the early universe by which the universe acquired the observed excess of matter over antimatter. The observed ratio

is given by [8]

$$\frac{N_B}{N_\gamma} \simeq \frac{N_B - N_{\bar{B}}}{N_B + N_{\bar{B}}} \simeq 10^{-9} \quad (2.12)$$

where  $B$  and  $\bar{B}$  denote baryons and anti-baryons and  $\gamma$  denotes photons.

In his seminal paper [9], Andrei Sakharov listed three conditions necessary for the generation of the baryon asymmetry:

- baryon nonconserving interactions must exist in nature
- both C and CP must be violated
- there must be a departure from thermal equilibrium.

Grand unified theories (GUTs) provide a theoretical framework that can accommodate C and CP violation and includes baryon nonconservation. Together with a non-equilibrium evolution of the universe, GUTs provide a plausible mechanism for baryogenesis.

At  $10^{-35}$  sec after the big bang matter is thought to have existed in the form of quarks and leptons. Baryon decay  $10^{-35}$  sec after the big bang and temperature  $T \simeq 10^{27}$  is assumed to have been mediated by a superheavy boson  $X$ ,  $M_X > 10^{14}$  GeV, which has baryon nonconserving interactions. When the temperature cooled below the GUT-scale,  $X$  and  $\bar{X}$  began to decay and if C and CP were violated then their decay rates may have been different [8]:

$$\frac{\Gamma(X \rightarrow q + q)}{\Gamma(X \rightarrow \text{all})} \neq \frac{\Gamma(\bar{X} \rightarrow \bar{q} + \bar{q})}{\Gamma(\bar{X} \rightarrow \text{all})} , \quad (2.13)$$

where  $q$ ,  $\bar{q}$  are quarks and antiquarks. When C is violated then the rate of production of baryons  $B$  corresponds to the difference of the two rates [10]:

$$\frac{dB}{dt} \propto \Gamma(X \rightarrow q + q) - \Gamma(\bar{X} \rightarrow \bar{q} + \bar{q}) . \quad (2.14)$$

Tests of discrete symmetries have been important for the establishment of the SM [10]. The observation of CP violation via the mixing of neutral kaons provided strong evidence for the presence of three quark and lepton generations, via the KM mechanism, prior to direct experimental evidence for the third generation. The level of CP violation in the kaon system, however, was not sufficient to account for the baryon asymmetry of the universe. The search for additional symmetry violating processes continued with new fervor.

### 2.2.3 Particle Electric Dipole Moments

Particles with electric dipole moments which are independent of the direction and magnitude of the applied electric field have *intrinsic* electric dipole moments. Induced electric dipole moments will not be considered.

In 1949 Purcell and Ramsey observed that parity violation in strong interactions would allow for an EDM of the neutron [11]. They also argued that there was no way to derive parity invariance and it should be validated experimentally [10]. Their pioneering work began a long history of EDM research. This warrants a closer look at particle electric dipole moments.

Classically, the EDM  $\vec{d}$  of a continuous charge distribution  $\rho$  is

$$\mathbf{d} = \int \mathbf{r}' \rho(\mathbf{r}') d\mathbf{r}. \quad (2.15)$$

A nonzero EDM exists when there is a net displacement between the positive and negative charges. We will focus on the EDM of the neutron. It is possible for the neutron to possess an EDM because its quark constituents carry charges. If the charges inside the neutron have some preferential displacement this would create an EDM of the form

$$\mathbf{d} = \int d^3x \langle \psi | \sum_i q_i \mathbf{r}_i | \psi \rangle = e d_n \vec{\sigma}. \quad (2.16)$$

The EDM, like the magnetic dipole moment, must lie along a particle's spin vector otherwise the ground state would become degenerate and additional quantum numbers would be needed. Thus the two possible orientations for the EDM are parallel or anti-parallel to the spin vector

$$\mathbf{d}_e = \pm d \frac{\mathbf{S}}{|\mathbf{S}|} . \quad (2.17)$$

Magnetic dipole moments are a consequence of charged particles having spin, but EDMs are forbidden by parity and time reversal symmetry, for example [12]. Figure 2.1 shows the actions of  $T$  and  $P$  symmetries on a particle with an EDM, the EDM is denoted as displaced charges. Under time reversal the direction of the spin is reversed (e.g. spin up becomes spin down) and the EDM is flipped as well. Under a parity transformation the EDM is reversed but the direction of spin does not change. The  $T$  and  $P$  transformed states are related by a rotation. Neither  $T$  nor  $CP$  returns the particle to its original state. The combined operation of  $CPT$  is conserved because charge conjugation does not affect the spin but reverses the EDM.

For a particle with spin  $J > 0$  and no extra degeneracies the static EDM violates separately  $T$  and  $CP$  symmetries. Using the Wigner-Eckart theorem the expectation value of the EDM vector operator  $\mathbf{d}_e$  for eigenstates of  $J$  can be written [2]

$$\langle j, m | \mathbf{d}_e | j, m \rangle = \langle j, m | \mathbf{J} | j, m \rangle \frac{\langle j | \mathbf{d}_e \cdot \mathbf{J} | j \rangle}{j(j+1)} . \quad (2.18)$$

Time reversal symmetry implies that  $T|j, m\rangle = \eta_T|j, -m\rangle$ , for some phase  $\eta_T$ , and  $T^\dagger \mathbf{d}_e T = \mathbf{d}_e$  then

$$\langle j, -m | \mathbf{d}_e | j, -m \rangle = -\langle j, -m | \mathbf{J} | j, -m \rangle \frac{\langle j | \mathbf{d}_e \cdot \mathbf{J} | j \rangle}{j(j+1)} \quad (2.19)$$

and therefore it follows that  $\langle j, m | \mathbf{d}_e | j, m \rangle = 0$ .

In more intuitive terms, the Hamiltonian of a spin-1/2 particle in electric and magnetic fields is written

$$\mathcal{H} = -\boldsymbol{\mu} \cdot \mathbf{B} - \mathbf{d}_e \cdot \mathbf{E} \quad (2.20)$$

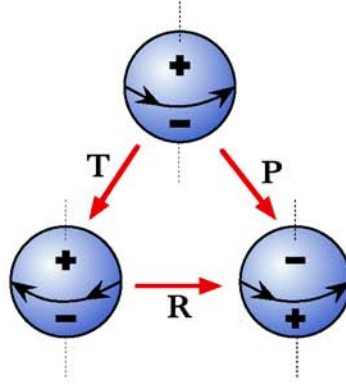


**Figure 2.1:** Action of  $P$  and  $T$  symmetries on a particle with EDM. The direction of spin is denoted by the arrow along the equator and the EDM is symbolized by the charged hemispheres. Under  $T$  the direction of spin is reversed but the EDM does not change and under  $P$  the EDM is flipped but the spin does not change. The two states are related by a rotation.

where  $\boldsymbol{\mu}$  is the magnetic moment and  $\mathbf{d}_e$  is the EDM. Under  $P : \mathbf{B} \rightarrow \mathbf{B}$  and  $\mathbf{E} \rightarrow -\mathbf{E}$  while under  $T : \mathbf{B} \rightarrow -\mathbf{B}$  and  $\mathbf{E} \rightarrow \mathbf{E}$ . Thus both  $P$  and  $T$  are violated in this system.

## 2.3 nEDM in the Standard Model and New Physics

The primary objective of EDM theories is the calculation of the EDMs of quarks and leptons. To a first approximation, the quark EDMs in the neutron add vectorially [13]

$$d_n = \frac{4}{3}d_d - \frac{1}{3}d_u \quad (2.21)$$

where  $d_d$  and  $d_u$  are the down and up quark EDMs and the coefficients reflect the presence of two down quarks and one up quark and also the expectation that the  $d_d$

is twice the size of  $d_u$ . In higher order  $d_n$  must have contributions from the presence of gluons,  $q\bar{q}$  pairs and even a 10% content of strange quarks.

$T$ -violation in QCD, and hence  $CP$  violation, is possible via a dimension four topological boundary  $\theta$  term [10]. If  $\theta \sim \mathcal{O}(1)$  then  $d_n > 10^{-18}$  e·cm and the nEDM would have been detected long ago, however  $\theta$  is known to be much smaller. The tuning of the  $\theta$  term is known as the strong  $CP$  problem. When QCD is coupled with the electroweak sector in the framework of the SM then the overall phase of the quark mixing matrix contributes to the  $\theta$  term [10]. The strong  $CP$  problem represents the absence of  $CP$  violation in flavor diagonal interactions whereas experimentally observed  $CP$  violation in the neutral Kaon system [14] is well-accounted for within the flavor changing sector by mixing of the quark generations. The Cabbibo-Kobayashi-Maskawa (CKM) flavor mixing matrix is the only source of  $CP$  violation in the Standard Model [15]. Confirmation of the CKM flavor mixing mechanism, and an additional  $CP$  violating mechanism, was found in the decay of neutral  $B$  mesons, [16] and [17].

There is little hope for finding flavor-diagonal  $CP$  violation at the level induced by CKM mixing. On the basis of CKM quark mixing, the nEDM prediction of the SM [12]

$$d_n \sim 10^{-32} \text{ e} \cdot \text{cm} \quad (2.22)$$

is far, far below the capabilities of any foreseeable experiments.

While the SM is incomplete, as for example it does not have a mechanism to give neutrinos mass and cannot explain dark matter, the predictions of the SM which have been verified experimentally have been resounding successes. There exist many extensions to the SM, such as supersymmetric theories, and success of the SM in some areas but not others has compelled searches for New Physics beyond the SM. The breadth of EDM experiments internationally is testament to the importance of

EDM research as a promising tool for exploring New Physics beyond the SM.

## 2.4 nEDM Experiments

Intrinsic EDMs violate  $T$  and  $CP$  directly and since the first measurements of Ramsey and Purcell still provide the most sensitive probes of CP violation in the flavor-diagonal sector. The neutron EDM first came into question after the seminal investigation by Ramsey and Purcell [11] of  $P$  conservation in the nuclear force. If the neutron ground state had a definite parity then its EDM would vanish [18]. Smith, Purcell and Ramsey [19] used a neutron beam magnetic resonance technique looking for a shift in the neutron Larmor frequency when an electric field was applied in addition to a magnetic field:

$$\omega_{\pm} = \gamma B_0 \pm 2ed_n E/\hbar \quad (2.23)$$

where  $\pm$  denotes the relative orientation of the  $E$  and  $B_0$  fields and  $\gamma$  is the gyromagnetic ratio. The first experiment produced a null result. However measurements of parity violation in the weak interaction garnered great attention from the community at about the same time, so further nEDM research gathered focus.

When a spin-1/2 particle precesses for a time  $T$  in a field  $B_0$  it acquires a net phase  $2n\pi + \phi$  where  $n$  is an integer [15]. The uncertainty in the precession frequency  $f$ , is

$$\delta f = \frac{\delta\phi}{2\pi T} \quad (2.24)$$

where  $\delta\phi$  is the uncertainty in  $\phi$ . If  $B_0$  is along the  $\hat{z}$  direction then to determine  $\phi$  it is necessary to use a spin analyzer in a direction perpendicular, such as  $\hat{y}$ . The probability to measure the spin along  $\pm\hat{y}$  when the final spin is nearly along  $\hat{x}$ ,  $\phi$  small, can be approximated by

$$P_{\pm} = (1 \pm \sin \phi)/2 \approx (1 \pm \phi)/2. \quad (2.25)$$



Repeating the measurement many times then gives

$$P_+ - P_- = 2P_+ - 1 = \phi. \quad (2.26)$$

It follows that since the average of  $P_+ = 1/2$  and its uncertainty is  $1/2$  then  $\delta\phi = 1$  [15]. The best possible Heisenberg-limited resolution is

$$\delta f = \frac{1}{2\pi T} \quad (2.27)$$

and if the measurement is made  $m$  times the uncertainty can be reduced to  $\delta f/\sqrt{m}$ . From the perspective of measuring a nEDM, or any measurement involving neutrons, it is beneficial to conduct the measurement with an ensemble of  $N$  systems measured simultaneously which gives the same  $1/\sqrt{N}$  reduction in uncertainty.

The EDM contribution to the precession frequency is  $f_e = 2d_n E/\hbar$ . The EDM measurement uncertainty then is

$$f_e = \frac{\hbar}{2eET\sqrt{mN}} \quad (2.28)$$

where  $E$  is the electric field. Taking into account the measurement time  $t$  and counting rate  $I$  then  $mN = It$  is the total number of systems measured to the desired sensitivity. The figure of merit for EDM-type measurements is given by

$$M = \alpha\beta ET\sqrt{I} \quad (2.29)$$

where  $\beta$  takes into account various inefficiencies and  $\alpha$  denotes any internal  $CP$ -odd contributions. If  $N$  particles are stored for a time  $T$  then the figure of merit increases only as  $\sqrt{T}$ . The limit on the EDM after a measurement time  $t$  becomes [15]

$$\delta d = \frac{\hbar}{2eM\sqrt{t}}. \quad (2.30)$$

### 2.4.1 Separated Oscillatory Fields Method

The early work of Ramsey pioneered the now famous method of separated oscillatory fields. Figure 2.2 summarizes the concept in the classical vector model of a spin-1/2 particle. Following the summary given in [15], a static magnetic field  $B_0$  is applied along the  $z$ -axis and an oscillating magnetic field  $B_1$  is applied along the  $y$ -axis. The Larmor frequency is given by  $\omega_0 = \gamma B_0$  and the oscillating field is set to  $2B_1 \cos(\omega t)\hat{y}$  such that  $|\omega - \omega_0| \ll \gamma B_1$ . The oscillating field can be written

$$B_1(\sin \omega t \hat{x} + \cos \omega t \hat{y}) + B_1(-\sin \omega t \hat{x} + \cos \omega t \hat{y}) \quad (2.31)$$

which can be understood as two counter-rotating fields. A rotating frame can be chosen corresponding to the direction of spin precession where the static field appears to decrease from  $B_0$  to  $B_0 - \omega/\gamma$ . When viewed from the rotating frame, the spin appears to precess around  $\hat{y}$  at the rate  $\gamma B_1/2$ .

In Ramsey's method, the oscillating field is switched on for a time  $\tau$  such that  $\gamma B_1 \tau/2 = \pi/2$ . This  $\pi/2$  pulse causes the spin to lie along the  $\hat{x}$  direction, perpendicular to  $\hat{y}$ , as seen from the rotating frame. After time  $\tau$  the spin is left to precess in the  $x-y$  plane at a rate  $\Delta\omega = \gamma\Delta B$ , where  $\Delta B = B_0 - \omega/2\gamma$ , for a time  $T$ . The spin makes an angle  $\phi = \Delta\omega T$  relative to  $\hat{x}$ . After time  $T$ , provided  $\Delta\omega \neq 0$ , as seen from the rotating frame the spin will not be perpendicular to  $\hat{y}$ . Then a second  $\pi/2$  pulse causes the spin component along  $\hat{x}$  to precess and lie along  $-\hat{z}$ . The spin projection along  $\hat{x}$  is  $\cos \phi$  and the difference of the probability of finding the spin along  $\hat{z}$  and  $-\hat{z}$  is given by

$$P_+ - P_- = -\cos \phi = -\cos \Delta\omega T. \quad (2.32)$$

This method gives a way of determining the spin precession frequency in relation to a known, stable oscillator and is sensitive to the accumulated phase of the spin relative to the oscillating magnetic field. More details about the Ramsey method are available in his book [20].

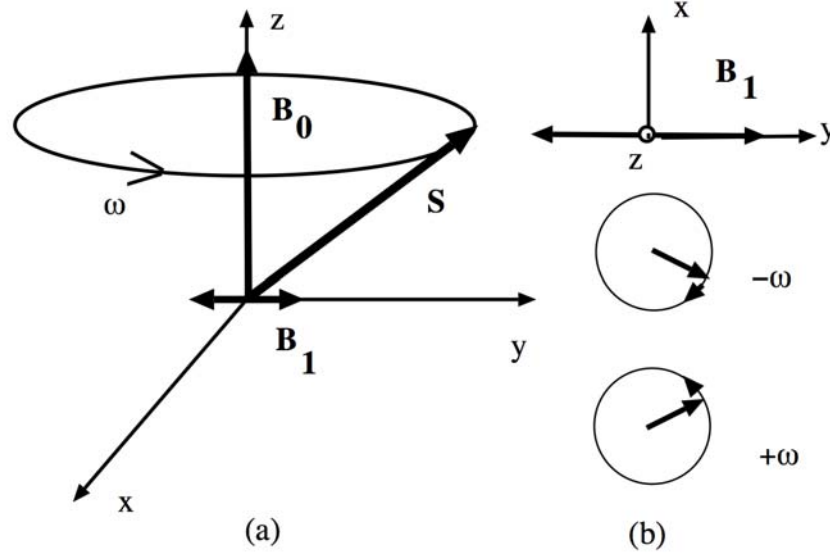


**Figure 2.2:** *a. Static magnetic field applied along the  $z$ -axis and an oscillating magnetic field along the  $y$ -axis in a classical vector model of spin-1/2 precession. b. Oscillating magnetic field represented as two counter-rotating fields, after [15]*

### 2.4.2 Neutron Beam Experiments

Neutron EDM experiments have been of two varieties: beam experiments and storage experiments. The first known nEDM experiment used a neutron beam at the Oak Ridge reactor around 1949-1951 as the Ph.D. thesis of J. H. Smith. It was not until 1957 that Smith, Purcell and Ramsey published their findings [19]. Figure 2.3 highlights the main features of the Oak Ridge nEDM experiment which included Ramsey's method of separated oscillatory fields.

A polarized neutron beam passed through a static magnetic field of 250 G which gave a Larmor frequency of 750 kHz and an electric field near 72 kV/cm. The two coils in Fig. 2.3 supplied the oscillating field. Figure 2.4 shows resonance curves of the

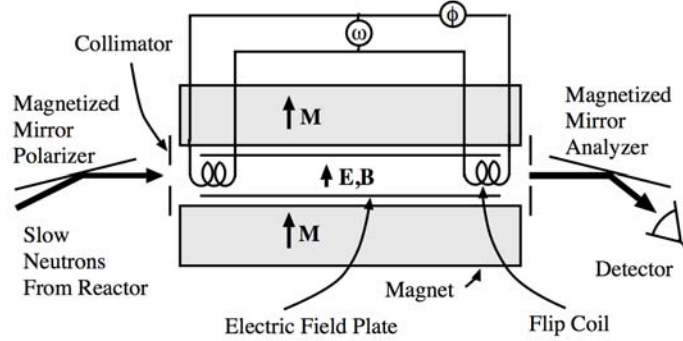


**Figure 2.3:** *Outline of Oak Ridge nEDM experiment from 1950, figure from [15].*

neutron counting rate against the magnetic field oscillation frequency for faster (top) and slower (bottom) neutrons. The angle of the magnetized mirror polarizer selected the average velocities of incoming neutrons. By setting the oscillating frequency to a value corresponding to the side of the central peak or valley the effect of the electric field polarity on counting rate could be determined. The experiment reported the upper limit

$$d_n < 5 \times 10^{-20} \text{ e cm.} \quad (2.33)$$

A second nEDM experiment [21] also at Oak Ridge a decade after the first was reported used improved neutron moderation and polarization techniques to produce neutrons of 60 m/s average velocity resulting in an interaction time 20 times longer [15]. The reported upper limit was

$$d_n < 6 \times 10^{-22} \text{ e cm.} \quad (2.34)$$

That same year Schull and Nathans published results of the MIT nEDM experiment [22]. This was a Bragg scattering experiment which used the electric field near in the CdS crystal to scatter neutrons using the  $\mathbf{v} \times \mathbf{E}$  field and the neutron magnetic

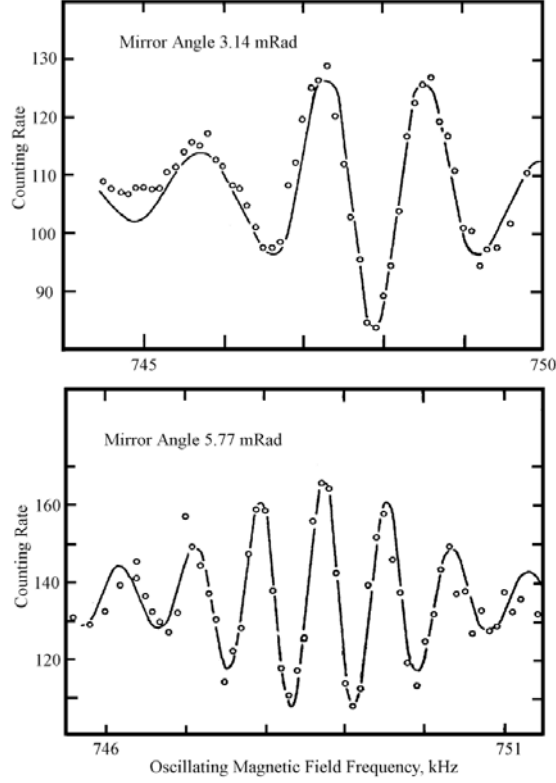


**Figure 2.4:** *Resonance curves from the first nEDM experiment, figure from [15].*

moment [23]. The nEDM contribution to the scattering potential is of the form  $V(\mathbf{r}) = -\mathbf{d}_n \cdot \mathbf{E}(\mathbf{r})$  where the electric field has the form  $Zer/r^3$  modulo electron screening effects. Each crystal plane makes a contribution to the scattered wave. Although the electric field is of order 10 MV/cm the interaction time is only of order  $10^{-7}$  s. Variation of the reflected intensity correlated with the neutron spin direction relative to the momentum transfer would imply a nEDM [15]. The experiment reported the upper limit

$$d_n < 8 \times 10^{-22} \text{ e cm.} \quad (2.35)$$

A better understanding of systematic errors at Oak Ridge in 1968 resulted in an improved limit of  $d_n < 3 \times 10^{-22}$  e cm [24] and again in 1969 [25] with the limit  $d_n < 5 \times 10^{-23}$  e cm. Although other nEDM experiments sprung up outside of Oak Ridge they tended to be limited by low neutron flux. The dominant position of the Oak Ridge nEDM apparatus continued until 1973 when a final set of improvements yielded the limit [26]

$$d_n < 1.0 \times 10^{-23} \text{ e cm.} \quad (2.36)$$

The Oak Ridge apparatus was eventually moved to the Institut Laue-Langevin (ILL) in Grenoble, France where the cold neutron flux was three orders larger than at Oak Ridge. With the higher flux and improved sensitivity some of the major systematics became sparks, leakage currents and forces between electrodes due to the electric field. Indeed the final result in 1977 [27] was limited by systematic effects and not by counting statistics:

$$d_n < 3 \times 10^{-24} \text{ e cm.} \quad (2.37)$$

### 2.4.3 Ultracold Neutron Storage Experiments

The second, and more successful, type of nEDM measurements used storage of slow neutrons. It was predicted in 1959 [28] that if the neutron kinetic energy was below some material threshold energy then neutrons could be stored by total reflection from material surfaces. The typical Fermi potential for material surfaces is  $U_F \sim 200$  neV which means for total reflections neutrons should have velocities near 5 m/s and effective temperature near 2 mK [15]. Neutrons which meet these criteria are termed ultracold neutrons (UCN). UCN have been useful not just for nEDM experiments but have contributed to many tests of fundamental principles; an excellent review of UCN technology can be found in [29].

A major advantage of storage experiments over beam experiments is the suppression of the  $\mathbf{v} \times \mathbf{E}$  effect, also called the motional field effect. Special relativity predicts that moving relative to a source of a static electric field generates a magnetic field  $\mathbf{B}_m$  in the moving frame:

$$\mathbf{B}_m \simeq \mathbf{v}/c \times \mathbf{E}. \quad (2.38)$$

$\mathbf{B}_m$  is on the order of a few tens of  $\mu\text{G}$  for a typical atomic thermal velocity of 300 m/s and static electric field strength 10 kV/cm [15]. For an EDM experiment with an applied magnetic field  $\mathbf{B}_0$  the effective field strength would be  $\mathbf{B} = \mathbf{B}_0 + \mathbf{B}_m$  with magnitude

$$B = B_0 + \theta_{\text{EB}} B_m + \frac{1}{2} \frac{B_m^2}{B_0} \quad (2.39)$$

where  $\theta_{\text{EB}}$  is the angle between  $\mathbf{E}$  and  $\mathbf{B}$  in the plane perpendicular to  $\mathbf{v}$  [15]. This produces a change in the Larmor frequency

$$\delta\omega = \frac{\gamma\theta_{\text{EB}}v}{c} E + \frac{\gamma v^2}{2c^2} \frac{E^2}{B_0}. \quad (2.40)$$

Thus when  $\theta_{\text{EB}} \neq 0$  a spurious shift in the frequency is generated which mimics the EDM. The motional field effect proved to be the limiting factor for beam experiments and could be suppressed in neutron storage experiments.

The capacity for a much longer interaction time with stored neutrons as opposed to a neutron beam meant that there was significant potential for improvement of the nEDM limit. Figure 2.5 shows a schematic of the UCN storage apparatus used at for the nEDM experiment at ILL. Using a UCN density around  $90 \text{ cm}^{-3}$  the experiment improved the limit in 1990 [30] to  $-(3 \pm 5) \times 10^{-26} \text{ e cm}$  giving the upper limit  $|d_n| < 12 \times 10^{-26} \text{ e cm}$  (90% CL).

In the 1990 ILL experiment the 5 liter storage chamber was filled with a polarized UCN density of  $10/\text{cm}^3$  through a door in the ground electrode (although the effective UCN density was closer to  $4/\text{cm}^3$  after each measurement cycle). A 10 mG magnetic

field was present parallel to the axis of the chamber and electric fields up to 1.6 MV/m were used. After filling with UCN, a Ramsey pulse was applied for four seconds which turned neutron spins perpendicular to the magnetic field. After 70 seconds the second Ramsey pulse was applied and then the chamber was allowed to empty. Neutrons in the appropriate spin state passed through a polarizer / analyzer to the detector. The spins of the remaining UCN were reversed adiabatically allowing them to also reach the detector. One measurement cycle took about 124 seconds and one run consisted of about 1000 measurements of the resonant frequency. A shift of the resonant frequency with applied electric field would indicate an EDM:  $\Delta\nu_n = [\nu_n(\mathbf{E}) - \nu_n(-\mathbf{E})]/2$ .

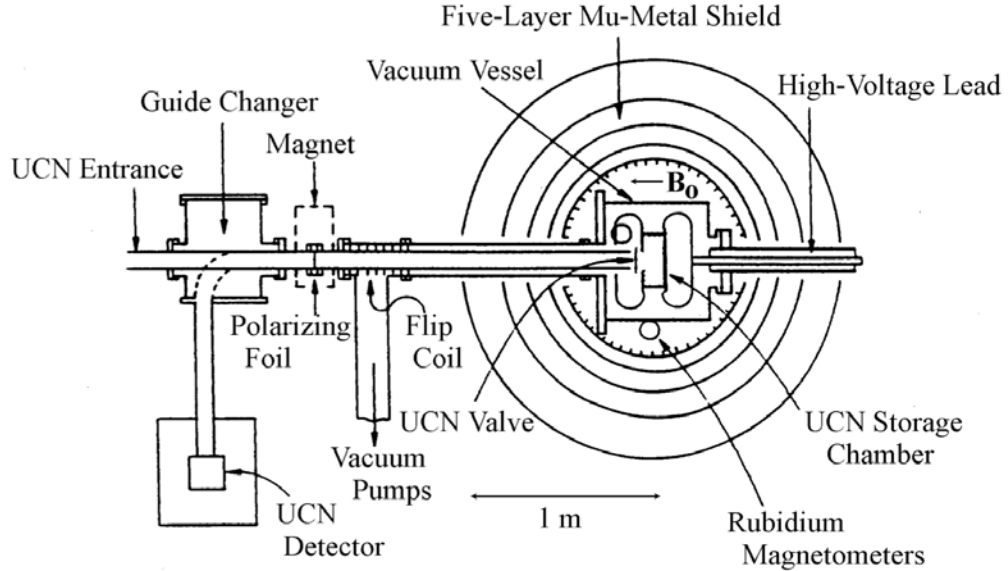


**Figure 2.5:** *Schematic of UCN storage nEDM experiment at the ILL, figure from [15].*

In 1992 a UCN nEDM experiment at the Petersburg Nuclear Physics Institute (PNPI) reported the limit  $1.1 \times 10^{-25}$  e cm [31].





## Chapter 3

# The SNS nEDM Experiment

### 3.1 The Search for nEDMs

The search for nEDMs has three facets: it tests for violation of time reversal symmetry, tests supersymmetry predictions and could help account for the baryon asymmetry of the universe. A nice historical survey of nEDM experiments can be found in [15].

The Standard Model (SM) prediction for the value of the nEDM is  $10^{-31}$  e·cm while the present experimental limit on the size of the nEDM is  $3 \times 10^{-26}$  e·cm [32]. The SM prediction is well-beyond the reach of present technology, however the five decades of sensitivity between the SM value and the present limit is fertile ground for new discoveries. The SM is not a complete description of the universe as, for example, in the case of symmetry violation. Many theoretical models exist beyond the SM which seek to solve the puzzles left behind by the SM. These models, such as supersymmetry, have their own predictions for the size of the nEDM and these predictions lie between  $10^{-26}$  and  $10^{-31}$  e·cm.

Figure 3.1 shows the recent progress in nEDM experiments and the relation to

theoretical predictions. In 1950 Purcell and Ramsey pointed out the absence of experimental evidence for parity symmetry in nuclear forces. As a first test of nuclear parity symmetry they sought to measure the nEDM and placed the first limit on its value [19]. Specifically, the nEDM is a probe of parity symmetry in the strong force but not the weak force. In 1956 T. D. Lee and C. N. Yang asked for experimental verification of parity symmetry in the weak interaction. Not long after that, Wu and Ambler observed that parity was violated in the decay of polarized  $^{60}\text{Co}$  [5]. Note the gap in nEDM experiments in Fig. 3.1 which resulted from opposition to nEDM experiments founded on the additional  $T$ -violating property of the nEDM and the popular consensus that a nEDM would be very unlikely. The discovery of  $CP$  violation (and indirectly also  $T$ -violation) in the decay of the  $K_0$  in 1964 [33] set off a bevy of nEDM experiments. Techniques using ultracold neutrons (UCNs) allowed for steady progress in nEDM research and, in particular, recent advancements in the production of UCNs at high densities have allowed rapid progress in the last decade.

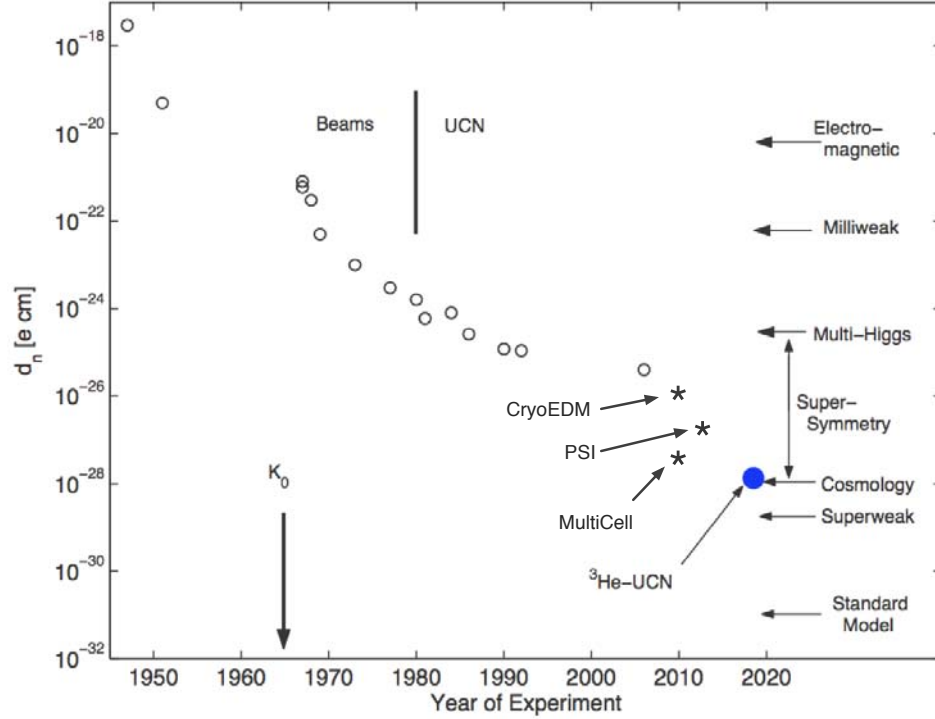


**Figure 3.1:** *Historical progress of neutron EDM measurements and relation to theoretical predictions of  $n$ EDMs. Experiments marked with \* are ongoing. The  $^3\text{He}$ -UCN experiment is described in the next section. [?]*

## 3.2 SNS nEDM Experiment

A recently proposed nEDM experiment is being constructed at the Spallation Neutron Source (SNS) in Oak Ridge National Laboratory [34]. Using new experimental techniques, the SNS nEDM experiment seeks to improve the present limit of the nEDM to the  $10^{-28}$  e·cm level. The present limit on the nEDM is  $d_n < 3 \times 10^{-26}$  e·cm (90% C.L.) measured in Grenoble at the Institute Laue-Langevin reactor [32].

A 2011 Report to the Nuclear Science Advisory Committee submitted by the Sub-

committee on Fundamental Physics with Neutrons said “...the scientific motivation for EDM searches remains as compelling as ever. In particular, a measurement with sensitivity at the anticipated reach of the US nEDM experiment ( $\sim 5 \times 10^{-28} \text{e}\cdot\text{cm}$ ) would have profound impact on nuclear physics, particle physics and cosmology, even in the event of a negative result.”

The SNS nEDM experiment is qualitatively different from the nEDM experiments which preceded it. The experiment uses the magnetic resonance technique where neutrons are polarized in a plane perpendicular to applied parallel magnetic and electric fields. The experiment relies on a three-component fluid made of ultracold neutrons and a dilute solution of  $^3\text{He}$  in a bath of superfluid  $^4\text{He}$ . The polarized  $^3\text{He}$  will act as a neutron spin analyzer by utilizing the large absorption cross-section for the spin singlet state. In addition, polarized  $^3\text{He}$  will also act as a co-magnetometer since its precession can be measured using Superconducting Quantum Interference Devices (SQUIDs), providing information about the *in situ* magnetic field. The polarized  $^3\text{He}$  within the same storage volume will provide accurate spatial and temporal averages of the magnetic field experienced by the neutrons. This is possible since  $d_{\text{atomic}}(^3\text{He}) < 10^{-32} \text{e}\cdot\text{cm}$  [35].

Ultracold neutrons for the experiment will be produced from the Fundamental Neutron Physics Beamline at the SNS which will deliver  $8.9 \text{ \AA}$  neutrons to the cryostat shown in Fig. 3.3. The incoming neutrons are polarized and downscattered to less than  $165 \text{ neV}$  in the superfluid  $^4\text{He}$  by emitting a phonon (Fig. 3.4). The  $8.9 \text{ \AA}$  neutrons are necessary so that the emission of a single phonon excitation will reduce the neutron energy to a minimum. The absorption of phonons by slow moving UCN is strongly suppressed below  $1 \text{ K}$ .

Inside the measurement cell (Fig. 3.3) ultracold neutrons and  $^3\text{He}$  are made to precess in the plane perpendicular to the weak magnetic holding field [36]. The gyromagnetic ratio of  $^3\text{He}$  is about 10% larger than that of neutrons and neutron

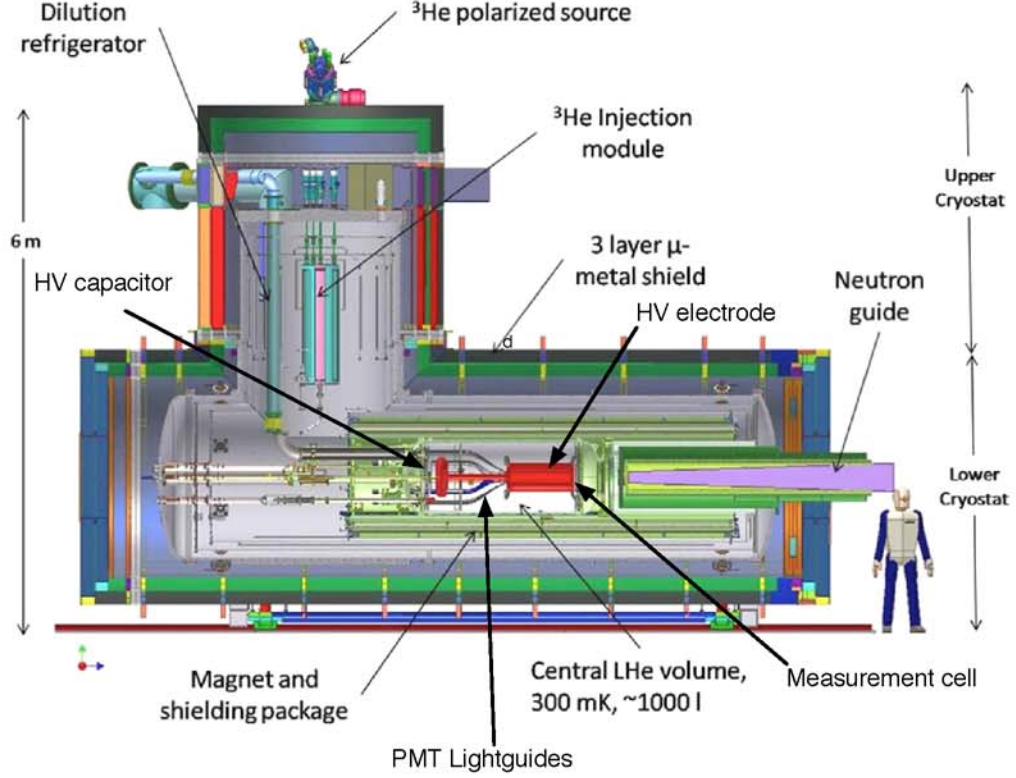


**Figure 3.2:** *The SNS nEDM experimental cryostat highlighting the main components. [36]*

absorption by  $^3\text{He}$  is very highly spin dependent. The cross-section for the spin singlet state is about 5.5 Mb, roughly 200 times higher than for the spin triplet state. The relative precession frequency of the UCN and  $^3\text{He}$  are monitored using the reaction



which produces ultraviolet light with wavelength 80 nm. The light is wavelength shifted so it can be detected by photomultiplier tubes. A strong electric field may influence the Larmor precession frequency of the neutrons if they possess an EDM

and thereby influence the rate of capture by  $^3\text{He}$ . Since  $^3\text{He}$  does not posses an EDM at the level of precision then any change in the frequency of detected scintillation light would be due to a change in the neutron precession. The precession frequency of neutrons is given by

$$\nu_n = -\frac{2\mu_n B_0 \pm 2d_n E_0}{h} = \nu_0 \pm \frac{\Delta\nu}{2} \quad (3.2)$$

where  $B_0$  is the weak magnetic holding field (10 mG),  $E_0$  is the applied electric field and  $h$  is Planck's constant. The nominal Larmor frequency is 29.2 Hz. The  $\pm$  reflects the fact that  $E_0$  is applied parallel or anti-parallel to  $B_0$ . By taking the difference between the two measurements the frequency shift is

$$\Delta\nu_n = -\frac{4d_n E_0}{h} . \quad (3.3)$$

The expected frequency shift for  $E_0 = 50$  kV/cm is

$$\Delta\nu_n = -1.6 \times 10^{-9} \frac{d_n}{1 \times 10^{-27} \text{ e}\cdot\text{cm}} . \quad (3.4)$$

The following example illustrates well the challenge of measuring a small EDM [37]. For a neutron in magnetic and electric fields the Hamiltonian is

$$\mathcal{H} = -(\mu_n \mathbf{s} \cdot \mathbf{B} + d_n \mathbf{s} \cdot \mathbf{E})/s . \quad (3.5)$$

On reversing the electric field relative to the magnetic field, one can look for an energy shift  $\Delta W = W_+ - W_-$ ,

$$W_{\pm} = 2\mu_n B \pm 2d_n E = \hbar\omega_B \pm \hbar\omega_E , \quad (3.6)$$

or a change in precession frequencies  $\omega_{\pm} = \omega_B \pm \omega_E$  from

$$\frac{d\mathbf{s}}{dt} = (\mu_n \mathbf{s} \times \mathbf{B} + d_n \mathbf{s} \times \mathbf{E})/s . \quad (3.7)$$

Using  $E = 10$  kV/cm and  $d_n \sim 10^{-26}$  e·cm the energy shift is  $\Delta W = 8 \times 10^{-22}$  eV and  $\Delta\omega = 7 \times 10^{-7}$  Hz. Compared with  $d_n$ ,  $\mu_n = 6 \times 10^{-12}$  eV/G and  $\omega_B = \omega_E$

when  $B \sim 10^{-10}$  G. This magnetic field is about the size of that produced by a small magnet 100 meters away!

EDM experiments, by their very nature, push the boundaries of what is physically possible to measure. The ultimate precision of a nEDM measurement can be deduced [37]. The energy difference under reversal of the electric field,  $\pm E$ , is  $\Delta W = 4d_n E$  and the uncertainty in the  $W_{\pm}$  is given by  $\hbar/t$  from the uncertainty principle, where  $t$  is the duration of the measurement. Then with  $N$  total neutrons, the uncertainty  $\delta d_n$  becomes

$$\delta d_n \sim \frac{\hbar}{2Et\sqrt{N}}. \quad (3.8)$$

Thus the highest precision will be possible with large  $E$ , long storage time and a large number of neutrons. The figure of merit for nEDM measurements is  $E\sqrt{N}\tau$  where  $N$  is the number of neutrons in the measurement cell and  $\tau$  is duration of the measurement [36]. Practical limitations place upper bounds on  $E$  and the neutron lifetime places a limit on  $\tau$ . This is the reason much effort has been spent in recent years on improving the neutron density for experiments which use UCN. The main advantages of using superfluid  $^4\text{He}$  as the working medium for the SNS nEDM experiment are its ability to sustain large electric fields and the *in situ* UCN production which helps maximize the number of UCN.

In superfluid  $^4\text{He}$  at 0.4 K the upscattering of neutrons by phonons is negligible and with an anticipated UCN production rate of 0.3 UCN/cm<sup>3</sup>/s the neutron density should reach up to 150 UCN/cm<sup>3</sup> during each 500 second measurement cycle. An accumulation of  $3\text{--}4 \times 10^5$  neutrons per measurement cell is expected.

The scintillation produced by the proton and triton products is in the extreme ultraviolet which is wavelength-shifted using deuterated tetraphenyl butadiene into light which can be detected by photomultiplier tubes (PMTs). It is expected that around 5 photoelectrons per capture would be observed by the PMTs. A number only



slightly lower would be insufficient to distinguish between the particles that produced the light, such as protons / tritons or electrons from beta decay or Compton-scattered capture  $\gamma$  rays [36] which could affect the background in the nEDM experiment and hence its sensitivity. An alternate detection method will be discussed in Chapters 5 and 6.

There are two complementary detection methods in the SNS nEDM experiment. The first is the free precession method which uses the dilute solution of polarized  $^3\text{He}$  in the superfluid  $^4\text{He}$  bath with a ratio  $N_3/N_4 \sim 10^{-10}$  and density  $\rho \sim 10^{12}/\text{cc}$ . The nEDM signal appears as a change in the relative precession frequencies of  $^3\text{He}$  and the UCN upon reversal of the electric field with respect to the magnetic field. The precession frequency of  $^3\text{He}$  should not change.

The second detection method uses dressed spin. A strong non-resonant rf field is applied as to ‘dress’ the spin of  $^3\text{He}$  by modifying its gyromagnetic ratio until the relative precession between  $^3\text{He}$  and the UCN is zero. Any departure from zero corresponding to changes in the electric field would indicate a nEDM. The advantage of this method is that the measurement becomes independent of variations in the ambient magnetic field since both  $^3\text{He}$  and the UCN respond in the same way to any variations.

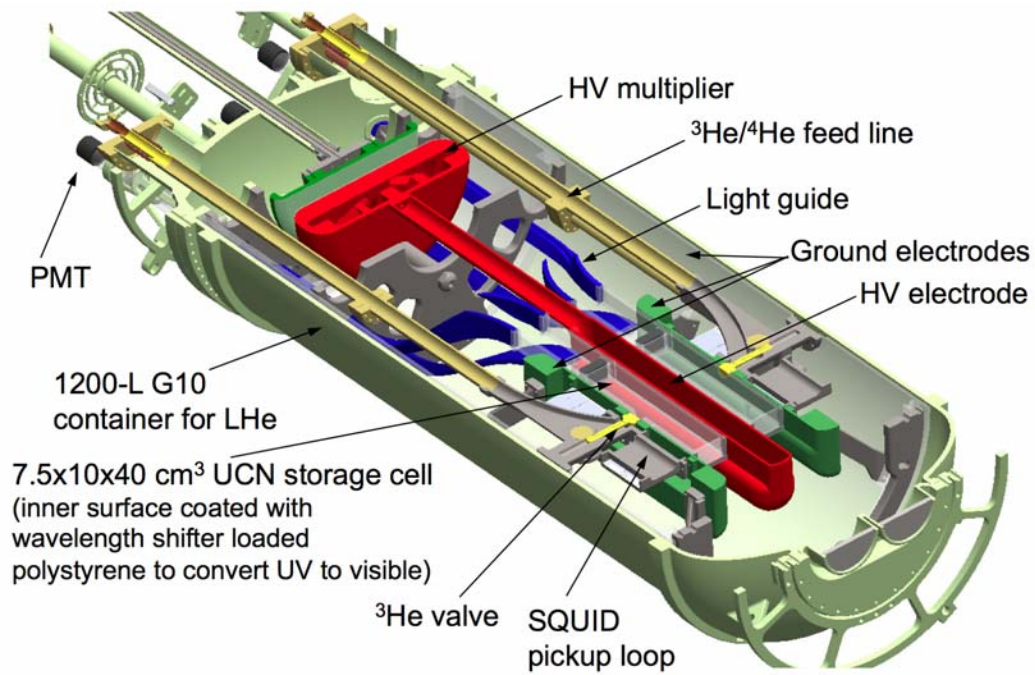


**Figure 3.3:** Closeup of the central volume of the nEDM cryostat showing the components surrounding the measurement cell.

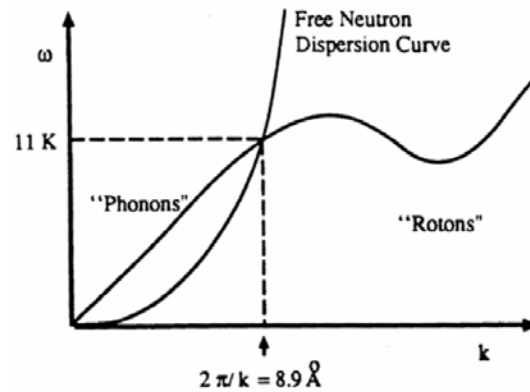


**Figure 3.4:** Dispersion curves for free neutrons and liquid  $^4\text{He}$ . The intersection of the curves is used for producing ultracold neutrons.

### 3.2.1 High voltage in the SNS nEDM

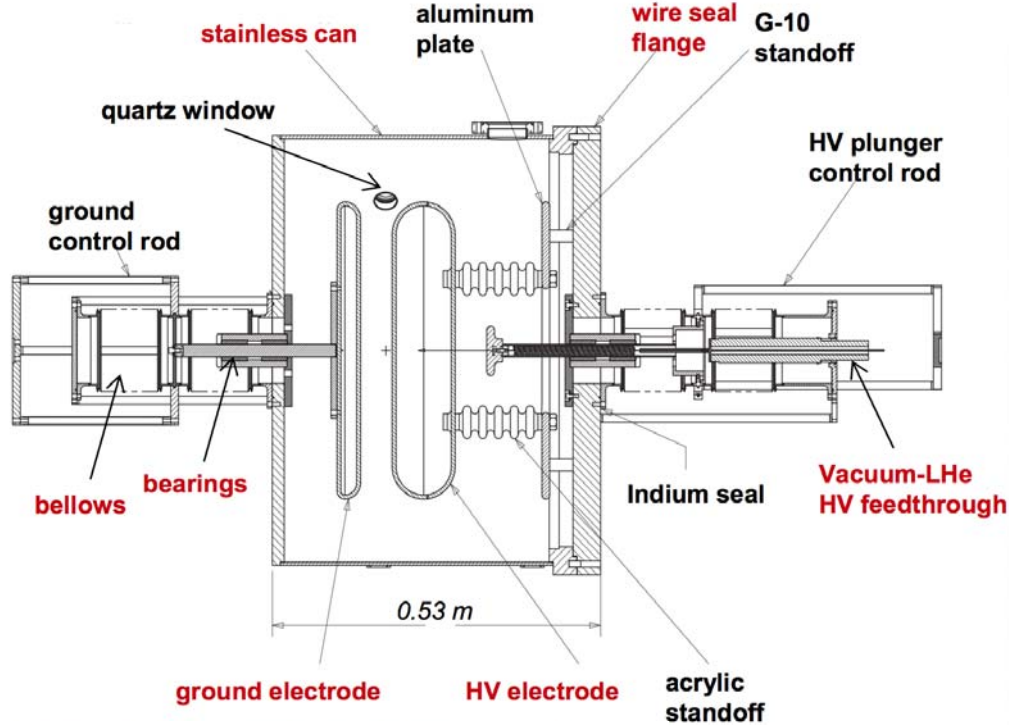


**Figure 3.5:** *High voltage multiplication system at LANL for characterizing the breakdown strength of liquid helium.*

The electric field in the SNS nEDM experiment is produced using a HV multiplier method [36]. The method works by connecting a pair of fixed electrodes to a variable capacitor, the variable capacitor is charged using a power supply and then the power supply is removed. The plates of the variable capacitor are then manually separated and, because the amount of charge is fixed, the voltage across the plates is increased because the capacitance is decreased. This method eliminates several potential complications including feedthroughs and cables which would need to be capable of handling hundreds of kV as well as any supply instabilities. Instead, the

---

HV multiplication method can use standard commercial feedthroughs and still be capable of supplying several hundred kV. Measurements of breakdown in superfluid  $^4\text{He}$  using this system however were not encouraging at the saturated vapor pressure. This motivated additional breakdown studies at and above saturation which will be discussed in the next chapter.

## Chapter 4

# Electric Breakdown in Normal Liquid and Superfluid Helium

### 4.1 High Voltage in the SNS nEDM Experiment

The increasing popularity of ultracold neutrons (UCNs) for EDM measurements means that significant focus is placed on the production of UCNs in this and the next generation of nEDM measurements. The advantages of using UCNs for studying nEDMs were discussed in the previous chapter. UCNs have in recent decades spurred progress in nEDM research and an additional several orders of improvement in sensitivity can be achieved with a corresponding increase in UCN density. Also of fundamental importance to nEDM (or any EDM investigation) is the electric field which couples to the particle's EDM and hence a larger magnitude electric field can generate a more sensitive measurement of the nEDM.

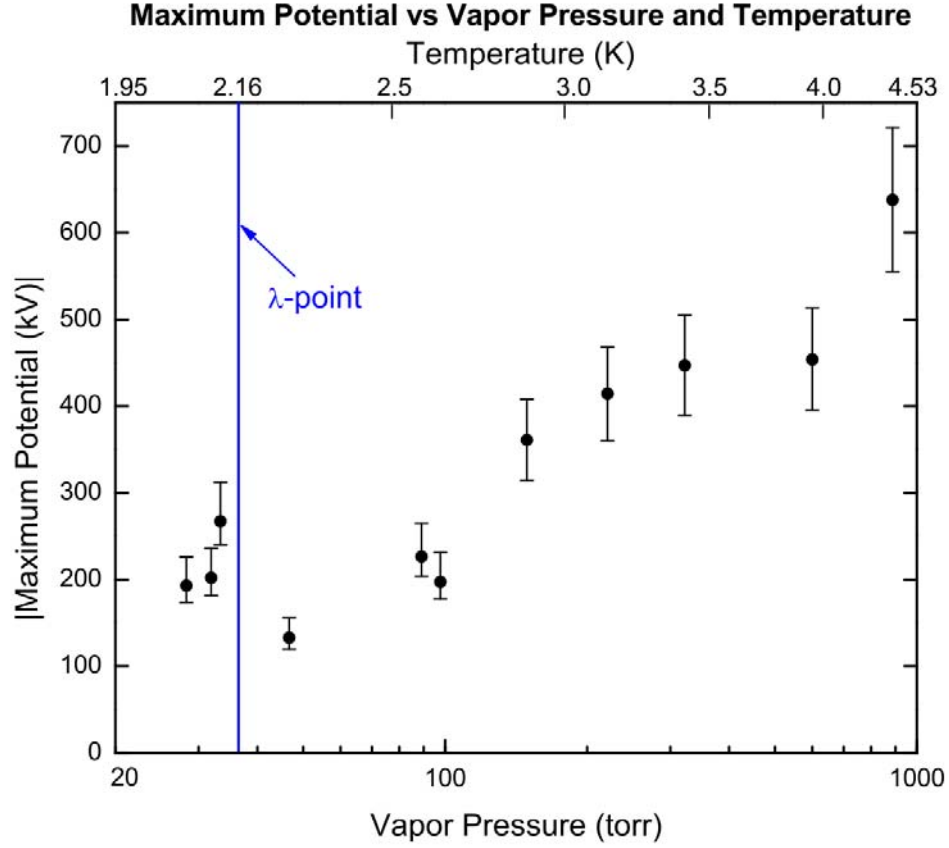


**Figure 4.1:** *Results of electric breakdown tests in liquid helium using the LANL setup [38].*

## 4.2 Liquid Helium & Superfluidity

Liquid helium (LHe) has been an attractive medium in physics experiments for many decades. Not long after helium was first liquefied at 4.2 K, it was observed that below about 2.17 K LHe underwent a transition to what came to be known as a superfluid, also known as He-II, to distinguish it from normal LHe, or He-I above 2.17 K. Since then, LHe has made possible the discovery and study of superconductivity, has been a model system in myriad experiments and low temperature applications, and of

interest for its many intrinsic properties such as macroscopic quantum behavior. A century after the first liquefaction of helium, LHe continues to be an important tool in physics research.

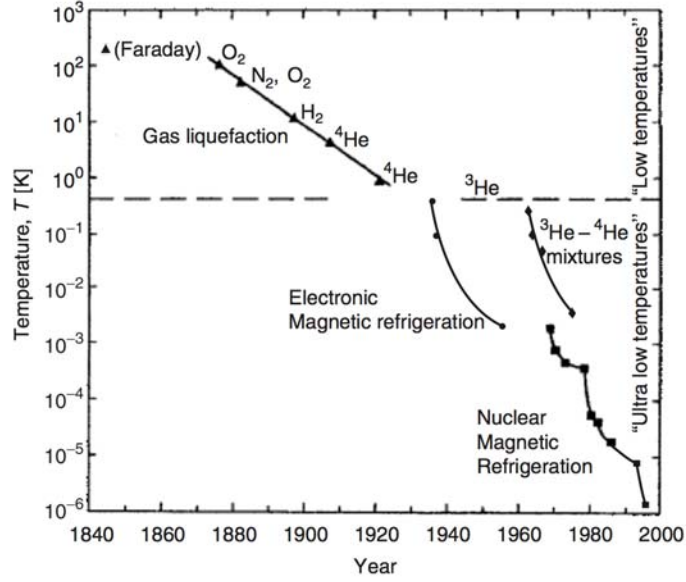


**Figure 4.2:** *Progress in low temperature technology, from [39].*

Despite the spherical shape of the  $1s^2$  shell of helium, and hence the absence of a permanent electric dipole moment, helium atoms still experience Van der Waals forces. Zero-point fluctuations in the charge distribution of the helium atom give rise to fluctuating electric dipole moments and attractive dipole-dipole interactions between neighboring atoms. Due to the very small atomic polarizability of helium atoms the binding force between neighboring atoms is weak. For a volume  $V$  containing a helium atom, the ground state energy is

$$E_0 = \frac{3\hbar^2\pi^2}{2mV^{2/3}} \quad (4.1)$$

and it can be seen that the small mass and atomic polarizability (binding energy)

means helium atoms have a large zero-point energy. For this reason helium has the lowest boiling temperature and is the only substance that remains liquid under saturation<sup>1</sup> in the limit  $T \rightarrow 0$ . Helium has a solid phase only at pressures above 25 bar.

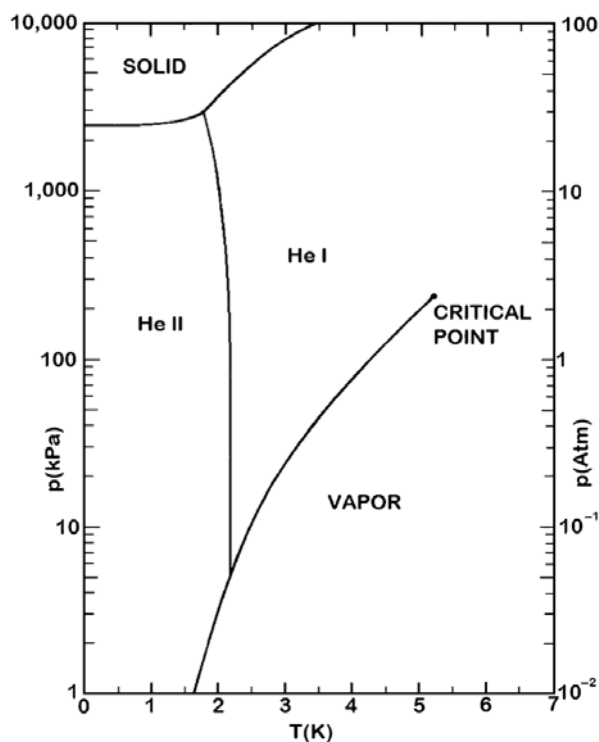


**Figure 4.3:** *Helium-4 pressure-temperature phase diagram, from [40].*

The specific heat of liquid helium was first measured by Dana and Onnes [41] and though they found an abnormality at 2.17 K it was not until the measurement was repeated by Keesom and Clusius [42] that the abnormality was attributed to a second

---

<sup>1</sup>Saturation means saturated vapor pressure or the vapor-liquid coexistence curve where vapor and liquid are always in equilibrium.



order phase transition. The second order phase transition at 2.17 K came to be called the  $\lambda$ -transition due to the shape of the specific heat curve as seen in Fig. 4.4.

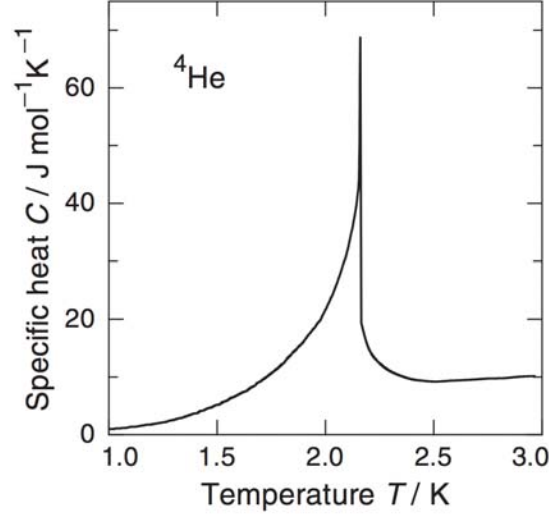


**Figure 4.4:** *Specific heat of saturated liquid helium, from [43].*

Experiments with liquid helium below  $T_\lambda = 2.17$  K showed that it was in many ways significantly different from liquid above  $T_\lambda$ . Simultaneous studies by Kaptiza [44] (who also coined the term *superfluidity* in analogy to superconductivity) and Allen and Misener [45] found He-II could flow through very narrow capillaries without any measurable friction. Following this, London suggested that superfluidity could be the manifestation of a Bose-Einstein condensate [46] which allowed Tisza to propose the two-fluid model of liquid helium [47].

The two-fluid model provides a phenomenological description of He-II and has been successful at explaining the various anomalous properties of He-II. Below  $T_\lambda$ , liquid helium behaves as if it is a mixture of two interpenetrating fluids with distinct properties [43]. Although this model does not provide a physical picture (since the two fluids are not physically separate) it is useful to express the density of He-II as

the sum of two components

$$\rho = \rho_n + \rho_s \quad (4.2)$$

where  $n$  and  $s$  denote the normal-fluid and superfluid components respectively, Fig. 4.5.

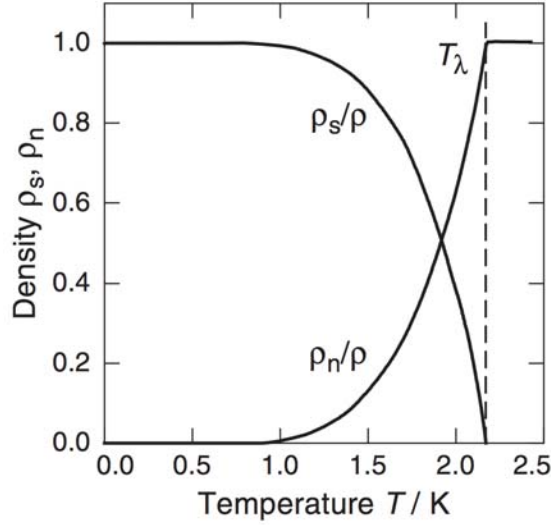


**Figure 4.5:** *Normal-fluid and superfluid fractions in He-II, from [43].*

In the two-fluid picture, the superfluid component does not carry entropy and exhibits no friction while the normal fluid carries all the entropy and exhibits viscosity. Below  $T_\lambda$  the temperature dependence of the normal fluid density is well-approximated by

$$\rho_n = \rho_\lambda \left( \frac{T}{T_\lambda} \right)^{5.6} \quad (4.3)$$

where  $\rho_\lambda$  is the total density at the  $\lambda$ -transition. The two-fluid model has been useful in understanding He-II flow through narrow capillaries where the normal-fluid component is blocked (such narrow channels are also known as superleaks). This gives

rise to the thermomechanical effect in He-II: when two containers of He-II are joined by a superleak and the pressure of one container is increased then the superfluid component will flow from one container to the other. This alters the  $\rho_s/\rho$  fraction of both containers and thus a temperature gradient results. The two-fluid model has also been successful in describing other He-II properties including heat transport and sound propagation.

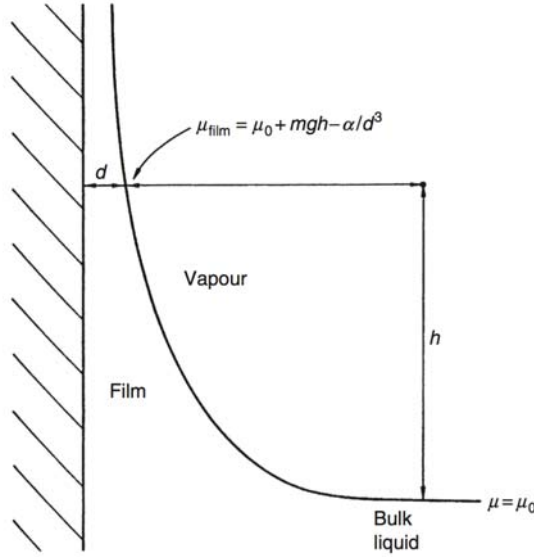


**Figure 4.6:** *Superfluid film on a vertical wall, from [39].*

Superfluid inside a container has the ability to coat all the inner surfaces with a film. Vapor atoms above the superfluid are adsorbed onto surfaces due to the strong Van der Waals interaction and the first layer of helium atoms forms a solid with the liquid film above it [39]. Film thickness is typically around 30 nm at SVP. Figure 4.6 shows a superfluid film on a vertical wall. For a thin film the thickness  $d$  is given by

$$d = (\alpha/mgh)^{1/3} \quad (4.4)$$

where  $\alpha$  is the van der Waals constant:  $\alpha/k_B = 10 - 200 \text{ K} \times (\text{number of He layers})^3$  [39], and  $mgh$  is the usual gravitational potential. Superfluid film should have interesting consequences for high voltage studies in He-II as will be discussed later. In principle, helium vapor should not be able to ‘see’ solid surfaces since they should be coated with film which should preclude heterogeneous nucleation of vapor from cavities in the solid surface but our data seem to show otherwise.

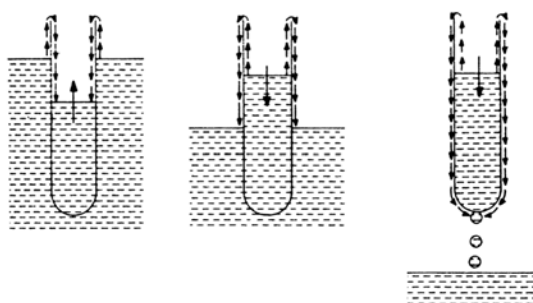


**Figure 4.7:** *The flow inside superfluid film allows it to travel into and out of containers, from [39].*

## 4.3 Electric Breakdown in Gases

Generally speaking, gases make good insulators. Electric breakdown is typically viewed as the sudden transition from an insulating to a purely conducting state.

When a small voltage is applied between two electrodes enclosing a gas then a small current will flow through the gas. When the voltage is increased then there is a corresponding increase in the flowing current. At sufficiently high voltage the current increases rapidly and the gas becomes temporarily conducting via a runaway process of charge multiplication known as breakdown.

The drift of charged particles in an electrically stressed gas gives rise to what is known as the dark current. Charged particles in the electrode gap originate from ionization of the gas due to naturally present radioactive substances and cosmic rays. Additional charges will be produced when the electric field is large enough to impart sufficient energy to moving charges so that neutral gas molecules can become ionized by collision. Impact ionization by electrons, when it becomes dominant and self-sustaining at large fields, is the reason breakdown occurs.

In this section the basic theory of electric breakdown will be outlined. Also discussed are empirical studies of breakdown in liquids with particular emphasis on cryogenics.

At small voltages and normal temperature and pressure gases are good insulators with low leakage currents. When the voltage between two electrodes is increased beyond some critical value there is a sharp increase in the current until an electrical breakdown occurs and the insulating gas transitions rapidly to a conducting state. The current which occurs between electrodes at different potentials is known as the ionization current and is due to the production and subsequent drift of electrons and ions. Mechanisms which produce ionization of the gas include collisions, photo-ionization and secondary ionization.

Ionization by collision is due to energetic electrons which gain energy from the electric field between collisions. When the energy gained between collisions exceeds the ionization potential of some gas species  $A$  then ionization by collision takes place



The initial electrons can be supplied by various means such as ultraviolet light striking the cathode, ionization due to cosmic rays or field emission from sharp points on the cathode. It is clear that this mechanism can produce an increasing number of electrons and ions and hence a rising ionization current (viz. the number of electrons striking

the anode is greater than the number of electrons liberated from the cathode). The efficiency of this primary ionization depends on the energy the electrons can acquire along its mean free path in the direction of the electric field. Positive ions striking the cathode can also liberate additional electrons which contribute to the ionization process.

Secondary ionization is the mechanism which causes discharges to be self-sustaining and leads to breakdown. The additional, or secondary, emission of electrons from the cathode is due to the impact of positive ions and ultraviolet photons. Secondary ionization by ion impact is described by the second Townsend ionization coefficient  $\gamma$  which is the probability that one electron will be liberated from the cathode upon impact. Similarly only a portion of electrons with energies above the ionization energy will ionize the gas since ionization by impact is a probability phenomenon and the ionization cross-section depends strongly on the electron energy [48]. Depending on the gas species, there exists an optimal electron energy for which the ionization cross-section is maximized, which could be a few times the ionization energy.

The average energy gained by an electron along the mean free path in the direction of the field is  $\Delta W = eE\bar{\lambda}_e$  where  $\bar{\lambda}_e$  is the mean free path along the direction of the field  $E$ . The energy  $\Delta W$  is proportional to the quantity  $E/p$ , where  $p$  denotes the gas pressure, since  $\lambda_e \propto 1/p$ . For the electron to ionize a neutral atom  $\Delta W \geq eV_i$  where  $V_i$  is the ionization potential. It is still possible, however, for electrons with energies less than the ionization energy to ionize atoms since the electron can excite the neutral atom and a subsequent collision with a second electron, whose energy is also less than the ionization energy, could ionize the atom.

The Townsend model of breakdown begins with the number of electrons  $n_0$  emitted from the cathode [49]. If at a distance  $x$  away from the cathode the number of electrons is  $n_x$  then a further distance  $dx$  there will be  $\alpha n_x dx$  electrons. Here  $\alpha$  is the first Townsend ionization coefficient and denotes the average number of ionizing

collisions between an electron and neutral atoms in a distance of one centimeter. It follows that

$$\frac{dn_x}{dx} = \alpha n_x \quad (4.6)$$

and thus

$$n_x = n_0 \exp(\alpha x) . \quad (4.7)$$

If the distance to the anode is  $d$  then the number of electrons reaching the anode will be  $n_d = n_0 \exp(\alpha d)$ . It follows that if  $I_0$  is the average current at the cathode then the average current  $I$  between the electrodes is given by

$$I = I_0 \exp(\alpha d) . \quad (4.8)$$

This process describes the electron multiplication due solely to first ionization, i.e. it does not take into account secondary electrons. The second ionization coefficient,  $\gamma$ , is the probability of electrons being emitted from the cathode by secondary means: it is a sum of contributions from the various possible means of secondary emission:  $\gamma = \gamma_1 + \gamma_2 + \gamma_3 + \dots$ . Both the first and second ionization coefficients are functions of the gas pressure  $p$  and reduced electric field  $E/p$  [49].

When secondary ionization is included then the number of electrons leaving the cathode can be written

$$n_0'' = n_0' + n_0 \quad (4.9)$$

where  $n_0'$  is the number of secondary electrons and  $n_0$  is defined as before. If  $n_d$  electrons reach the anode then

$$n_0' = \gamma[n_d - (n_0 + n_0')] \quad (4.10)$$

and

$$n_d = (n_0 + n_0') \exp(\alpha d) . \quad (4.11)$$

Combining the two equations above then gives

$$n_d = \frac{n_0 \exp(\alpha d)}{1 - \gamma[\exp(\alpha d) - 1]} \quad (4.12)$$

or in terms of current

$$I = \frac{I_0 \exp(\alpha d)}{1 - \gamma[\exp(\alpha d) - 1]} . \quad (4.13)$$

As seen in the equation above, below some threshold value of  $d$  if the initial current  $I_0$  is removed then the total current tends to zero. However, as the electrode separation  $d$  is *increased* then the total number of charges created is increased and the denominator tends to zero and this will lead to breakdown. Above some critical value of the separation

$$1 - \gamma[\exp(\alpha d) - 1] = 0 \quad (4.14)$$

depicting a runaway current and corresponding to a breakdown. This is known as Townsend's breakdown criterion [49] and is often written

$$\gamma[\exp(\alpha d) - 1] = 1 \quad (4.15)$$

$$\gamma \exp(\alpha d) \simeq 1 . \quad (4.16)$$

For some configuration of gas pressure and electrode separation there will be some voltage  $V$  for which values of  $\alpha$  and  $\gamma$  satisfy the breakdown criterion. It should also be noted that the Townsend mechanism is considered valid for values of  $pd$  (the product of gas pressure and electrode separation) less than about 1000 torr-cm. The investigation described in this chapter is consistent with the Townsend  $pd$  region of validity. For higher values of  $pd$  the more correct picture is provided by the streamer theory of breakdown.



### 4.3.1 Paschen law of breakdown

The first and second Townsend coefficients are functions of  $E/p$

$$\alpha/p = f_1(E/p) \quad (4.17)$$

$$\gamma = f_2(E/p) \quad (4.18)$$

and  $E = V/d$ . The breakdown criterion can thus be written

$$f_2\left(\frac{V}{pd}\right) \left\{ \exp \left[ pd f_1\left(\frac{V}{pd}\right) \right] \right\} = 1 . \quad (4.19)$$

The expression for the first ionization coefficient is determined experimentally to be

$$\frac{\alpha}{p} = A \exp \left[ - B/(E/p) \right] \quad (4.20)$$

where  $A = \sigma_i/kT$  and  $B = V_i\sigma_i/kT$  and  $\sigma_i$  is the ionization energy. The constants  $A$ ,  $B$  have to be determined experimentally and the expression for  $\alpha$  is only valid for a range of  $E/p$  values. Table 4.1 shows the measured values  $A$ ,  $B$  for various gas types. The experimental values of  $A$ ,  $B$  however rarely agree with the theoretical values defined above due to many simplifications which are made in the derivation.

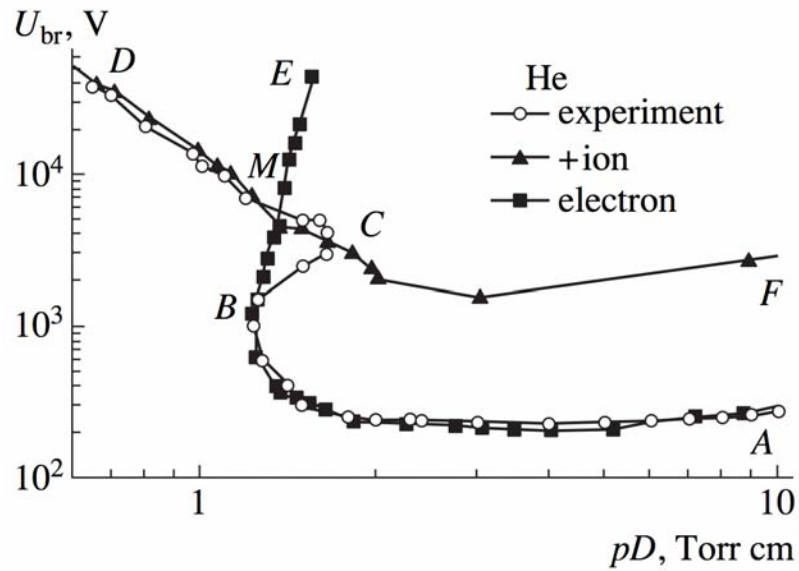
Because for a given  $pd$  the voltage which satisfies the breakdown criterion is the breakdown voltage  $V_b$  then the equation above implies that  $V_b$  is a function of  $pd$ ,

$$V_b = f(pd) . \quad (4.21)$$

The relationship in Eq. 4.21 is known as the Paschen law. Fig. 4.8 shows the Paschen curve for helium gas. It is straightforward to establish the Paschen curve by measuring the breakdown voltage for a series of  $pd$  values if the pressure and electrode spacing are known accurately.

**Table 4.1:** *Experimental values for  $A$ ,  $B$  at STP, from [48].*

<i>Gas</i>	<i>A</i> <i>ion pairs</i> <i>cm<sup>-1</sup> Torr<sup>-1</sup></i>	<i>B</i> <i>V cm<sup>-1</sup></i> <i>Torr<sup>-1</sup></i>	<i>E/p range</i> <i>V cm<sup>-1</sup> Torr<sup>-1</sup></i>	<i>V<sub>i</sub></i> <i>volts</i>
H <sub>2</sub>	5	130	150-600	15.4
He	3	34	20-150	24.5
N <sub>2</sub>	12	342	100-600	15.5
Air	15	365	100-800	—
CO <sub>2</sub>	20	466	500-1000	12.6
Hg	20	370	200-600	—

**Figure 4.8:** *The theoretical and experimental Paschen curves for helium gas, from [50].*

There are several noteworthy features of the Paschen curve which are true for Paschen curves for all gas types. Above the Paschen minimum (for larger values of  $pd$ ), the breakdown strength is a linear function of  $pd$  and below the minimum the breakdown strength increases rapidly. The Paschen law is summarized by the equation

$$V_B = \frac{Bpd}{\ln \left( \frac{Apd}{\ln(1+1/\gamma)} \right)} \quad (4.22)$$

where  $A, B$  are empirical constants and  $\gamma$  is the second ionization coefficient.

While most gases have similarly shaped Paschen curves, the shape of the helium curve however is peculiar, as shown in Fig. 4.8. Hartmann and colleagues [51] analyzed the shape of the helium Paschen curve using experiment and simulation. The position of  $(pd)_{\min}$  and its corresponding voltage are determined by the gas type and cathode material. For helium, it was found that at low pressure (left of the Paschen minimum) breakdown can occur at three different voltages [52]. The span of voltages is as much as two orders of magnitude and the manifestation of one of the three voltages can depend on the preponderance of different charge generating processes

- electron collisions with He atoms (elastic scattering, excitation, ionization)
- $\text{He}^+$  ion collisions with He atoms (elastic scattering, charge transfer,  $2^1\text{P}$  excitation, ionization)
- collisions of fast He atoms with He gas (elastic scattering,  $2^1\text{P}$  excitation, ionization).

## 4.4 Nucleation theory

Nucleation theory describes the germination and growth of phase nuclei when a system undergoes a phase transition. Nucleation theory can be used to model a variety of

systems which undergo phase transitions ranging from solid-liquid-vapor transitions to magnetic domains and growth of nanofilms. This discussion will focus on nucleation in the liquid-vapor transition and discuss its relevance to electric breakdown.

A transformation of a system from phase  $A$  to phase  $B$  occurs in two ways: via the *homogeneous* and *heterogeneous* nucleation of phase  $B$ . Homogeneous nucleation of a new phase occurs inside the bulk of a pure material (e.g. away from the walls of the container) and is the result of random density fluctuations due to thermal motion. Homogeneous nucleation is an intrinsic property of the material and represents the limit of stability of phase  $A$ . Observing homogeneous nucleation in a substance requires very careful experimental conditions.

Nearly all phase transitions in ordinary experience are heterogeneous in nature. Heterogeneous nucleation of phase  $B$  inside of phase  $A$  occurs due to the presence of container walls, impurities or other disturbances which reduce the energy barrier for the formation of phase  $B$ . The accepted parameters (such as temperature and pressure) for phase transitions of ordinary substances are always in terms of heterogeneous nucleation of the second phase.

#### 4.4.1 Heat transfer hysteresis

An abundance of studies has been done on heat transfer dynamics in liquids. In particular, liquid helium has been of great interest for its myriad applications in cooling and intrinsic properties. He-I has a relatively small thermal conductivity and relatively large specific heat [53]. Steady state heat transport is dominated by convection rather than conduction in He-I. For studies of heat flux and heat transfer the primary determining factor is surface roughness and involve measuring the relationship between heat flux and change in temperature. The significance of the surface roughness to wetting and heat transfer will be discussed.

There are three principal regimes of heat transfer

1. natural convection: density-driven currents without phase change
2. nucleate boiling: activation of vapor nucleation sites on surface
3. film boiling: continuous vapor film on heated surface

which are distinguished by their critical heat fluxes [53]. The nucleate boiling regime marks the onset of the phase change when heat flux is increased beyond the convection limit.

Figure 4.9 shows typical heat transfer hysteresis in He-I. Below a certain heat flux heat is transferred by convection. As the heat flux is increased vapor nucleation sites become ‘activated’. The activation of vapor nucleation sites is the formation and growth of vapor bubbles on irregularities on the heated surface. As the heat flux is raised or lowered, nucleation sites can become activated and de-activated: it is this process which causes hysteresis. For heat flux near the convection limit more nucleation sites are activated and as the heat flux is reduced some of the sites can remain activated, i.e., can trap small vapor bubbles. A subsequent increase in heat flux can meet with a larger number of activated sites. Beyond a critical heat flux  $q^*$ , the high rate of bubble growth and detachment creates a continuous vapor film on the heated surface. To recover the nucleate boiling regime it is then necessary to reduce the heat flux to below  $q^*$ .

The values of critical heat fluxes which distinguish between the three regimes vary by 2-3 factors among different investigations [53] and depend greatly on the surface preparation (which determines nucleation site density). The orientation of the heated surface also influences heat transfer since the gravitational force aids in bubble detachment. Highest values of critical heat fluxes are measured in surfaces facing upward. This bodes well for a ground electrode which faces upward and a

spherical high voltage electrode which can reduce vapor trapping inside the gap in the HV cryostat. Finally, the bath pressure affects the heat flux boundaries between the regimes through the deactivation of nucleation sites.

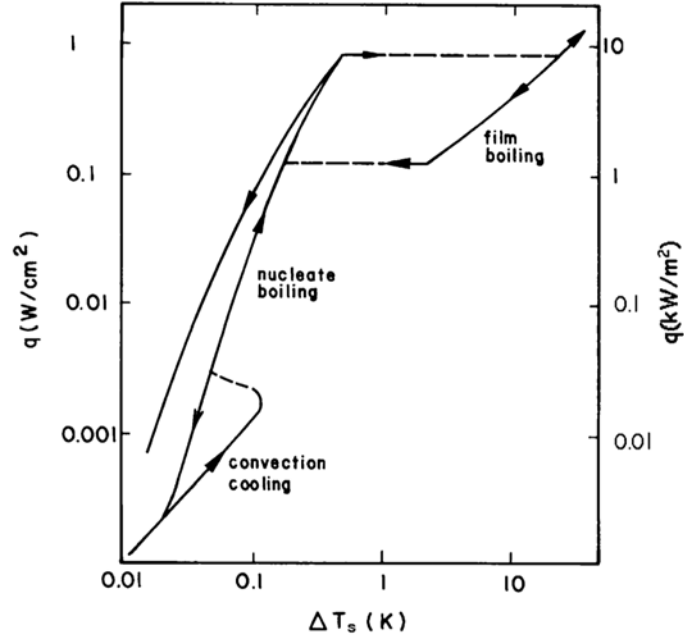


**Figure 4.9:** *Typical heat transfer hysteresis in He-I, from [53].*

#### 4.4.2 Nucleation, wetting & pre-breakdown

In classical nucleation theory, in the homogeneous case, the critical bubble radius is given by the relation

$$P_V = P_L + \frac{2\sigma}{R_c} \quad \text{or} \quad R_c = \frac{2\sigma}{\Delta P} \quad (4.23)$$

where  $P_V$  is the vapor pressure, inside the bubble  $P_L$  the pressure of the liquid medium,  $\sigma$  the surface energy per unit area and  $R_c$  the critical bubble radius in chemical equilibrium with the liquid, for example [54]. Equation 4.23 is known as the

Laplace-Kelvin equation. The critical bubble is in mechanical equilibrium with the surrounding liquid while bubbles smaller than  $R_c$  will tend to collapse and bubbles larger than critical tend to grow spontaneously (Fig. 4.10). The relative improbability of homogeneous nucleation is due to the work necessary to overcome the critical bubble size, known as the nucleation energy barrier. Homogeneous bubbles form by density fluctuations in the liquid when the localized density is temporarily lower than the average density. Molecules that travel into this region can undergo evaporation and molecules that travel from this region into denser fluid undergo condensation. The number of critical sized nuclei is given by the Boltzmann distribution

$$n = N \exp(-\Delta F_{max}/kT) \quad (4.24)$$

where  $N$  is the number of molecules and  $\Delta F_{max}$  is the nucleation barrier [55]. The rate of molecule transfer to bubbles of critical size, which cause spontaneous growth, determines the nucleation rate. The nucleation rate, whether homogeneous or heterogeneous, is a measure of the level of superheat that a liquid can sustain. More generally, the energy required for the formation of a spherical vapor bubble of radius  $R$  is

$$\Delta F = 4\pi R^2 \sigma - \frac{4\pi}{3} R^3 f \quad (4.25)$$

where  $f$  is the unit volume.

For free bubbles in liquid equilibrium can be of two forms: mechanical and chemical. In practice, the actual equilibrium is something in between, depending on relaxation times of bubble evolution. In liquids with low viscosity, where the bubble radius can adjust rapidly, mechanical equilibrium is favored while chemical equilibrium prevails at higher viscosity if evaporation is also rapid.

If the molecules in a vapor bubble are treated as an ideal gas, kinetic theory predicts that the number distribution of molecules having velocities between  $v$  and

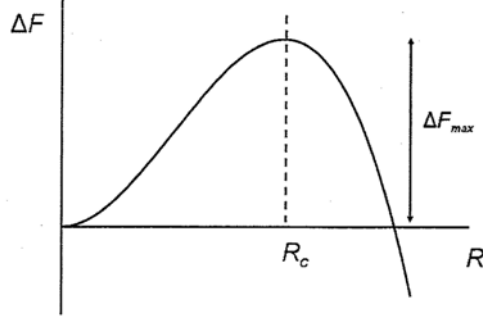


**Figure 4.10:** *Free energy barrier for spherical bubble formation, from [55].*

$v + dv$  is given by the Maxwell distribution

$$dn_v = 4\pi n \left( \frac{m}{2\pi k_B T} \right)^{3/2} v^2 e^{-mv^2/2k_B T} dv . \quad (4.26)$$

The corresponding Maxwell energy distribution is given by

$$dN_\epsilon = 2\pi N (\pi k_B T)^{-3/2} \epsilon^{1/2} e^{-\epsilon/k_B T} d\epsilon \quad (4.27)$$

where  $dN_\epsilon$  is the number of molecules having kinetic energies between  $\epsilon$  and  $\epsilon + d\epsilon$ . It follows that the number of molecules with kinetic energies greater than  $\epsilon^*$  is given by

$$N_{>\epsilon^*} = \int_{\epsilon^*}^{\infty} dN_\epsilon . \quad (4.28)$$

For systems with a phase boundary it is useful to define the fraction of molecules with energies greater than  $\epsilon^*$  which, after carrying out the above integral, is given by

$$\frac{N_{>\epsilon^*}}{N} = \left( \frac{4\epsilon^*}{\pi k_B T} \right)^{1/2} e^{-\epsilon^*/k_B T} + \operatorname{erfc}(\sqrt{\epsilon^*/k_B T}) \quad (4.29)$$

where  $\operatorname{erfc}$  is the complimentary error function. The fraction defined by Eq. 4.29 is a rapidly increasing function of temperature and is characteristic of molecules in



both gases and liquids [40]. This becomes relevant when charges inside a vapor region subjected to an electric field gain energy and a vapor bubble can become a localized source of heat.

Vapor bubbles, such as those that might originate from boiling of the cryogen, can become attached to flat surfaces. In practice, however, few surfaces are truly flat except for glasses. Nevertheless, the bubble on a flat surface serves an illustrative purpose. Figure 4.13 shows a spherical approximation of a vapor bubble attached to a flat solid. Bubbles attached to surfaces demonstrate the triple contact line, which is the boundary where all three phases meet. The  $\sigma_i$  denote the surface energies of the liquid-vapor, liquid-solid and vapor-solid boundaries. A simple balance of forces for a bubble in mechanical equilibrium, Fig. 4.13, yields Young's equation

$$\sigma_{VS} = \sigma_{LS} + \sigma_{LV} \cos \theta_c . \quad (4.30)$$

The energy required to produce the bubble shown in Fig. 4.13 is modified, and lower than the free bubble, due to its volume and the interface between the vapor and solid. Assuming the bubble is hemispherical then the volume becomes

$$V = \frac{1}{3}\pi R^3(1 + \cos \theta)^2(2 - \cos \theta) \quad (4.31)$$

and the area of the liquid-vapor interface becomes  $2\pi R^2(1 + \cos \theta)$  and the area of the vapor-solid interface is  $\pi R^2 \sin^2 \theta$ .

The surfaces of crystalline solids are an ever-present source of scratches, grain boundaries and other irregularities at nm- $\mu$ m scales. Figure 4.14 shows how an advancing liquid front might trap gas or vapor inside a crevice. The advancing contact angle of the liquid is  $\theta$  and the half-angle of the crevice is  $\beta$ . The first part of the figure shows the case when  $\theta < 2\beta$  and the liquid is able to fill the crevice. In the second part  $\theta > 2\beta$  and the advancing liquid front covers the crevice before filling with liquid. The contact angle of the liquid is a measure of its wettability and depends on the interaction between the liquid and substrate at the atomic level.

Once vapor is trapped inside a crevice then a meniscus is formed between the liquid and vapor (e.g., see [56] and references therein). Figure 4.12 shows the types of heterogeneous vapor bubbles for (a) flat and (b)-(c) grooved substrates. Compared with the homogeneous spherical case, the volume and surface energy terms are modified in the heterogeneous case.

Taking into consideration nucleation of boiling is particularly important since evaporative cooling is used in LHe. Throughout the cooling process it is assumed that the saturation condition is satisfied, i.e. the system cools along the saturation curve. It is very likely then that boiling is present in the bulk liquid originating at heterogeneous nucleation sites such as impurities and surfaces. It is known that the thermal conductivity of He-II is several orders of magnitude higher than He-I, for that reason after the  $\lambda$ -transition evaporation is expected to take place only at the liquid surface due to the absence of thermal gradients.

Small contact angles correspond to high wettability whereas low wettability means large contact angles. For any liquid, the contact angle at any time must be confined between two extremes:  $\theta_a < \theta_c < \theta_r$ , where  $\theta_a$  is the advancing contact angle and  $\theta_r$  is the receding contact angle.

The roughness of the surface being covered by liquid affects wettability. It has long been known that smoother surfaces can produce better wettability.

It has been shown that pockets of vapor occurring due to incomplete wetting at surfaces are energetically favorable over vapor bubbles in the bulk liquid. In [55] the author provides a nice description of various bubble types. In the case of a spherical bubble (Fig. ??-a) inside bulk liquid the free energy is

$$\Delta F = 4\pi R^2 \sigma - \frac{4\pi}{3} R^3 \delta P \quad (4.32)$$

where  $\sigma$  is the liquid-vapor surface energy,  $R$  the radius of the spherical bubble and  $\delta P = P_0 - P$  the difference between the pressure inside the bubble and the saturation

pressure  $P_0$ .

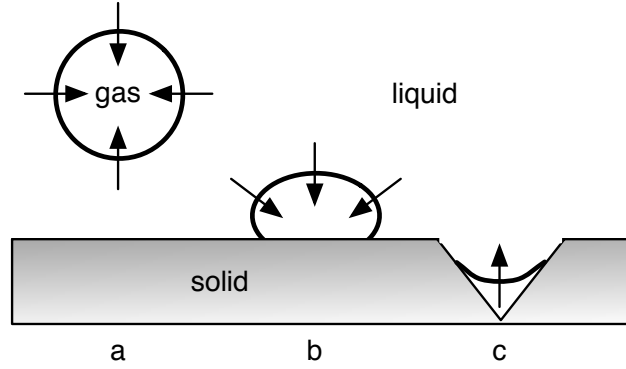


**Figure 4.11:** *Some bubble types. Arrows indicate the directions of surface forces. a.) bubble floating in bulk liquid, least stable. b.) bubble attached to surface, more stable. c.) bubble inside surface crevice, concave outward, can withstand great pressure.*

If a bubble is attached to a surface then its energy is modified [55]

$$\Delta F = \left( 4\pi R^2 \sigma - \frac{4\pi}{3} R^3 |\delta P| \right) \lambda \quad (4.33)$$

where  $\lambda$  is a geometric factor defined as

$$\lambda = \frac{(1 + \cos \theta)^2 (2 - \cos \theta)}{4} \quad (4.34)$$

and  $\theta$  is the angle of contact between the vapor bubble and solid surface (Fig. 4.12). Note that  $0 < \lambda < 1$  and thus such a bubble is more favorable over a spherical bubble in the bulk liquid.

The final type of vapor bubble considered is that contained inside a surface crevice as shown in Figure 4.12. In this case, the free energy is given by

$$\Delta F = \left( 4\pi R^2 \sigma - \frac{4\pi}{3} R^3 |\delta P| \right) f(\theta, \beta) \quad (4.35)$$

where the geometric function  $f$  is given by

$$f(\theta, \beta) = \frac{1}{2} - \frac{\sin(\theta - \beta)}{2} + \frac{\cos^2(\theta - \beta) \cos(\theta)}{4 \sin(\beta)}. \quad (4.36)$$

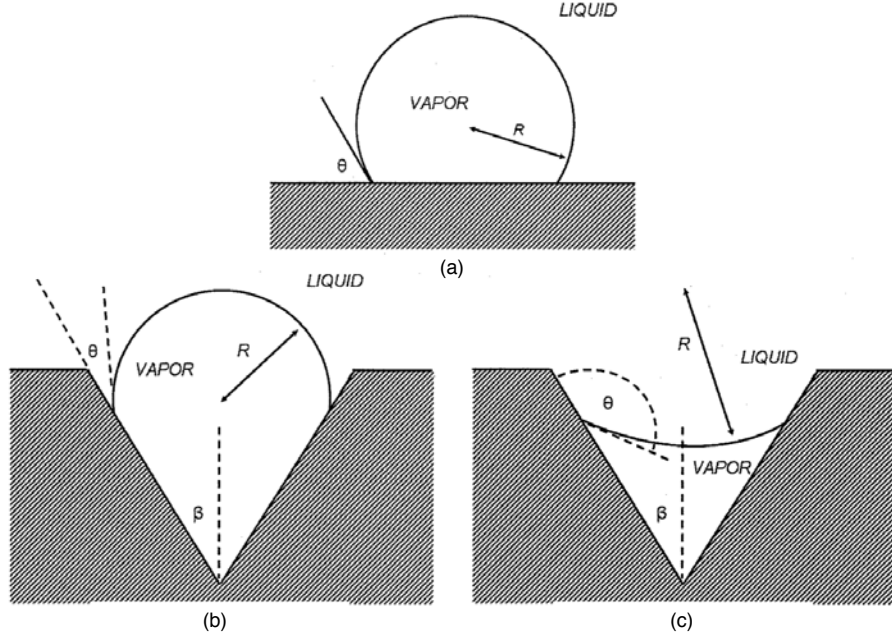


**Figure 4.12:** *Types of heterogeneous vapor bubbles, from [55].*

In this case, depending on the condition of the liquid, the surface of the vapor bubble can be either concave outward or concave inward (as seen in Figs. 4.11-c) and 4.12-c). The amount of concavity of the liquid-vapor interface is bounded by the advancing and receding contact angles and depends on the applied pressure. The turning point of the concavity occurs at  $\theta_c = \beta + \pi/2$ . For  $\theta < \theta_c$  the bubble will be concave inward and for  $\theta > \theta_c$  concave outward. As applied pressure decreases, the contact angle will decrease until it reaches  $\theta_r$  and will not decrease beyond that. If the pressure continues to decrease, it will be more favorable for a new liquid-vapor interface to form and a bubble will germinate from the nucleation site. Similarly,

when the pressure is increased the contact angle will increase until it reaches  $\theta_a$  and will not increase beyond that. Then the liquid-vapor interface may move toward the apex of the crevice. At the time of nucleation, such as during boiling, the trapped bubble meniscus shifts from concave on the liquid side to convex on the liquid side (Fig. 4.12-b and c).

The nucleation barrier (free energy maximum) is smallest for vapor pockets inside surfaces crevices, such as would be found on poorly polished electrodes. The probability for nucleation, which increases as the energy barrier decreases, is thus higher on rough surfaces.

The history of the liquid under study plays a critical role in nucleation phenomena. Studies done by Winterton and Gallagher [57–59] show the importance of the pressure history heterogeneous nucleation inside a liquid.

The pressure across the liquid-vapor interface of a bubble trapped in a crevice is given by:

$$\Delta P = P_1 - P_2 = \frac{2\sigma}{R} \quad (4.37)$$

where  $P_1$  is the pressure inside the bubble,  $P_2$  the pressure outside and  $R$  the radius of the bubble interface. The right hand side is clearly greater than zero. This is known as Kelvin's formula and it suggests that the differential pressure can become very large for very small bubbles. This has the implication that small bubbles can exhibit extreme mechanical stability against outside forces, such as pressurization. In the case of a bubble inside a conical crevice, as the interface is pushed deeper inside the crevice, due to for example an increasing pressure, the radius of the interface decreases by virtue of the shape of the crevice.

Carrier injection by field emission is one way to create low density vapor regions in a liquid insulator. However, in practice it is more likely that low density vapor regions already exist due to incomplete wetting before the application of the field.

It is easy to imagine that such regions would act as preferential regions for carrier injection and subsequent growth of these regions by impact ionization for example. Vaporization continues in this way until the electrode gap is bridged by a low density vapor channel and breakdown can occur at this time.

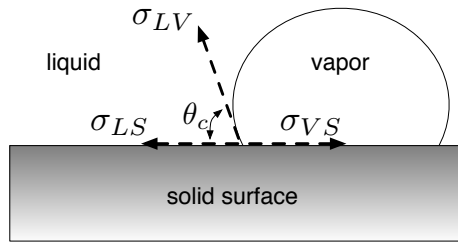


**Figure 4.13:** *A vapor bubble attached to a smooth flat surface.*

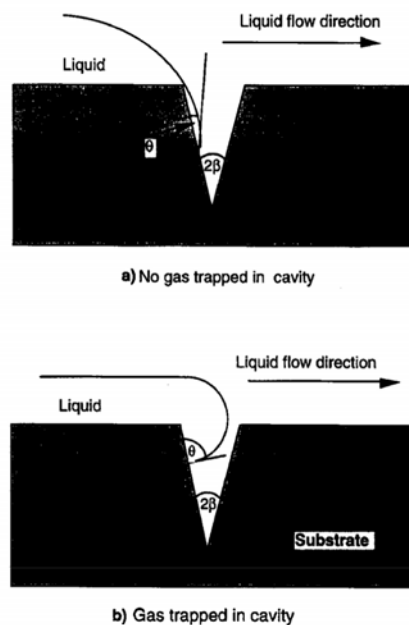


**Figure 4.14:** *Simplified geometry of an advancing liquid front on a solid surface with a crevice, from [56] The contact angle of the liquid is given by  $\theta$  and the crevice half-angle is  $\beta$ .*

## 4.5 Apparatus

The experimental cryostat consists of two nested LHe volumes: a high voltage experimental volume (HVEV) contained inside a larger volume that serves as a thermal bath. The HVEV can be sealed off from the outer volume, so that the pressure of the LHe within it may be controlled independently of the temperature, which is in turn determined by the LHe in the outer bath. A schematic of the HVEV is shown in Fig. 4.15. The outer cryostat is shown in Fig. 4.18.

High voltage is introduced to the HVEV via a commercial ceramic feedthrough, rated to 20 kV (Fig. 4.15), which is terminated by a spherical electrode screwed onto its end. The HV sphere is secured using vibration-proof washers (vacuum pumps and

cryogen boiling cause vibrations which can shift the electrode position), which also act as spacers to adjust the vertical position of the sphere relative to the feedthrough. Dimensions of the electrodes and other components of the HVEV are given in Tab. 4.2. The total LHe volume of the HVEV, with all components installed, is  $0.18 \ell$ .

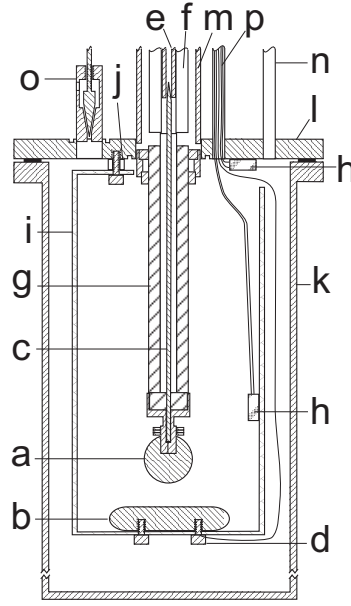


**Figure 4.15:** HVEV elevation, to scale. a) Spherical HV electrode. b) Cylindrical ground electrode. c) HV conductor. d) Ground connection screw, with leakage current monitor wire. e) HV conductor extension (capillary). f) Teflon insulator. g) Ceramic HV feedthrough (Kurt Lesker model EFT012091). h) RuO temperature sensors (Lakeshore model RX-102A). i) G-10 insert. j) Macor spacer. k) Stainless steel enclosure. l) Top flange with Mylar gasket. m) HV capillary ground shield (evacuated). n) Stainless steel He gas line for pressurization. o) Custom needle valve, nominally SF-tight. p) Stainless steel tube for temperature sensor and ground leads.



A plate–sphere electrode configuration is used to reduce geometrical uncertainties associated with parallel plates. The ground electrode is a flat cylinder with rounded edges. It is attached with two screws to the flat bottom of a G10 fiberglass epoxy insert coaxial with the feedthrough (Fig. 4.15). Both screws holding the ground electrode are connected to leads that exit the HVEV through a stainless steel tube. The two leads are grounded outside the cryostat; the ground electrode can be electrically isolated from the HVEV for leakage current measurements. Continuity between the leads can also be tested at any time to ensure proper grounding after the system is sealed and cooled. The vertical position of the G10 insert relative to the feedthrough can be adjusted, allowing additional flexibility in the electrode gap. Typical gap sizes in the experiment range from 0.5 mm to 1.5 mm.

Either electrode can be replaced or easily adjusted between runs; electrodes of different materials and/or surface preparations can be tested. Most of the experiments reported below use electrodes made from type 304 stainless steel. After machining, the electrodes are polished with progressively finer finishing papers, up to 1500 or 2500 grit (ANSI). The electrodes are then polished with a commercial compound [60] which reduces the surface roughness to well below  $1\text{ }\mu\text{m Ra}$ . Finally, the electrodes undergo ultrasonic cleaning in acetone and alcohol. A separate set of electrodes underwent additional commercial electropolishing and chemical cleaning steps [61]. While advertised electropolished surface roughness can reach as low as a few nm Ra, in practice, electropolishing tends to reduce the roughness attained by the final mechanical polish by a factor of 2. More importantly, electropolishing smoothes out the smallest features of the surface. Figures 4.16 and 4.17 show the electropolishing process and AFM scans of a typical handpolished electrode and an electropolished electrode.

The HVEV is housed inside a stainless steel cylindrical enclosure (Figs. 4.15 and 4.18). The vacuum-tight seal for the enclosure is made using a Mylar gasket

**Table 4.2:** HVEV dimensions (all units cm.)

HV electrode diameter	1.27
Ground electrode diameter	3.17
Ground electrode thickness	0.64
Ground electrode edge curvature radius	0.32
HV feedthrough diameter	1.90
HV feedthrough length	8.08
G10 support inner diameter	5.00
G10 support wall thickness	0.08
G10 support length	11.00
Steel enclosure inner diameter	6.80
Steel enclosure wall thickness	0.10
Steel enclosure length	17.80
HV conductor extension capillary outer diameter	0.30
HV capillary length	40.00
HV capillary teflon insulator outer diameter	1.90
HV capillary shield (grounded) inner diameter	2.54
Pressurization capillary inner diameter	0.32
Pressurization capillary length	75.00

coated with silicone vacuum grease. The HVEV is filled with LHe from the outer bath through a custom needle valve. The valve is nominally superfluid (SF) tight and remains closed during pressurization studies. The valve is controlled manually with a torque rod installed in a compression fitting in the outer LHe volume top flange (Fig. 4.18). Dimensions of the outer volume are given in Table. 4.3

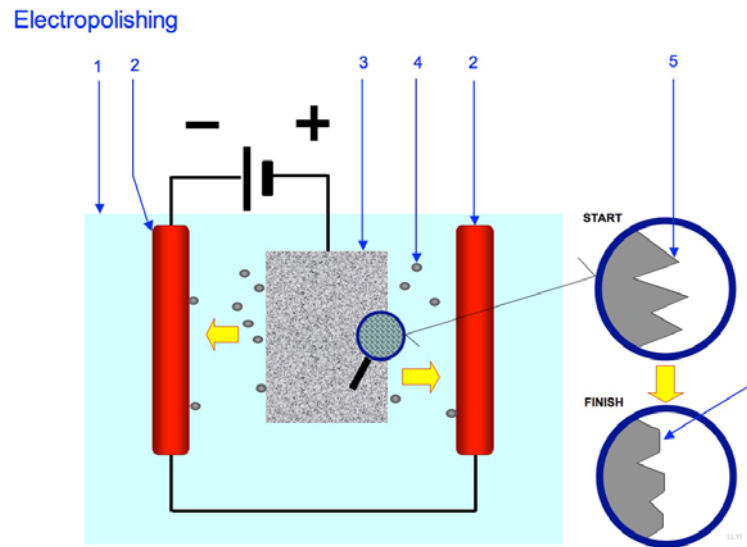


**Figure 4.16:** *The electropolishing process, from [62]. 1. electrolyte solution 2. cathode 3. metal workpiece (anode) 4. metal residue removed from workpiece 5. surface before electropolishing 6. surface after electropolishing*

The central conductor of the HV feedthrough connects to a stainless steel capillary (Fig. 4.15). The capillary runs through the neck of the outer cryostat inside a stainless steel tube, and is insulated with a teflon sleeve running the length of the tube (Fig. 4.18). The tube is evacuated to remove contaminants which may solidify at LHe temperature and short out the capillary.

A second, external ceramic HV feedthrough is attached to the top of the stainless tube with a vacuum-tight seal (Fig. 4.18). It is connected to a DC HV power supply with a coaxial cable, fastened to the top of the feedthrough by a spherical brass electrode. The outer shield of the cable is connected to a grounded aluminum cage that surrounds the external feedthrough. The DC power supply has a capacity of 30 kV

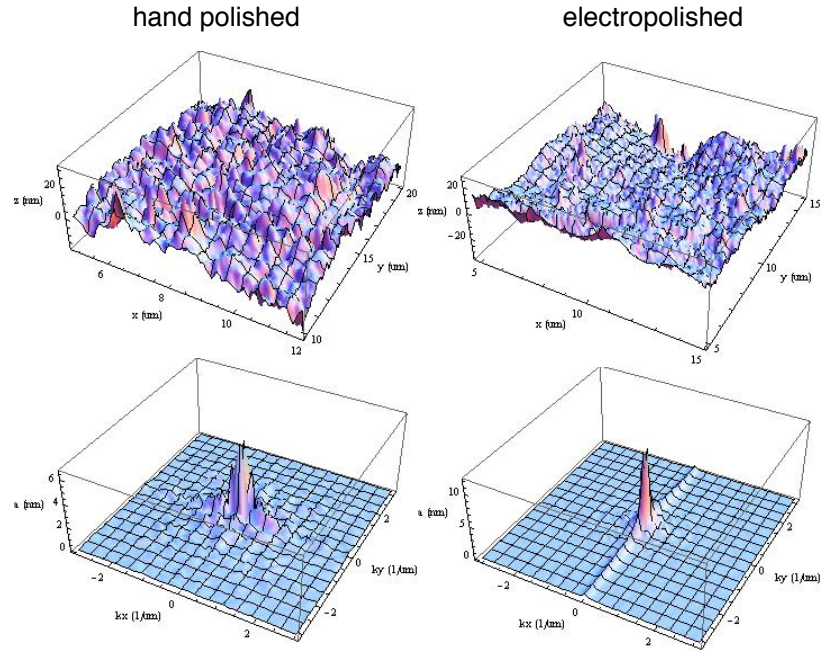


**Figure 4.17:** *AFM scans of hand polished and electropolished electrodes, by A. Peckat. Lower plots show the 2-D Fourier transforms of roughness.*

**Table 4.3:** Outer volume dimensions (all units cm.)

LHe main volume inner diameter	15.2
LHe main volume length	45.7
LHe volume neck inner diameter	7.0
LHe volume neck length	30.5
LHe volume pumping port inner diameter	5.0
Outer vacuum volume diameter	25.4
Outer vacuum volume height	63.5

and 3 mA, with ripple specified to better than 0.03% RMS of rated voltage (plus an additional 0.5 V) at full load. The power supply also has interchangeable polarity modules, allowing for straightforward tests of polarity dependence in the experiments.

Pressure in the HVEV is controlled by maintaining a small volume of He gas above the liquid level. With the SF-tight needle valve closed, gas is introduced to the HVEV through a stainless steel capillary (Figs. 4.15 and 4.18). The capillary is supplied from a gas manifold.

The manifold and other external connections are illustrated in Fig. 4.19. He gas is supplied to the manifold from a pressurized cylinder. A 2-stage regulator on the cylinder allows for accurate control of gas flow and pressure. The HVEV pressure is monitored using mechanical gauges on the gas manifold, with 0.1 torr resolution.

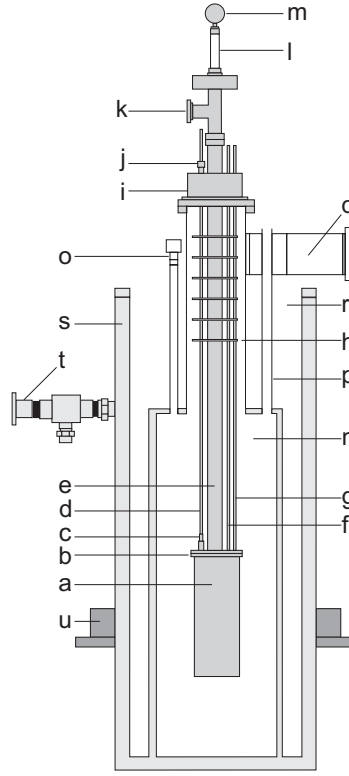


**Figure 4.18:** *Outer cryostat with custom HVEV probe inserted. a) HVEV enclosure. b) HVEV top flange. c) Custom needle valve, nominally SF-tight. d) Needle valve torque rod. e) HV capillary ground shield (evacuated). f) Stainless steel tube for temperature sensor and ground leads. g) Stainless steel He gas line for pressurization. h) Radiation baffles (6). i) LHe volume top flange. j) Compression seal for needle valve torque rod. k) HV capillary ground shield pumpout port. l) Ceramic HV feedthrough (Kurt Lesker model EFT012091). m) spherical electrode for attaching HV cable. n) LHe volume. o) LHe fill and level sensor port (1 of 2). p) LHe vent. q) LHe volume pumpout port. r) Liquid nitrogen volume. s) Insulating vacuum volume. t) Insulating vacuum volume pumpout port. u) Adjustable mounting flange.*

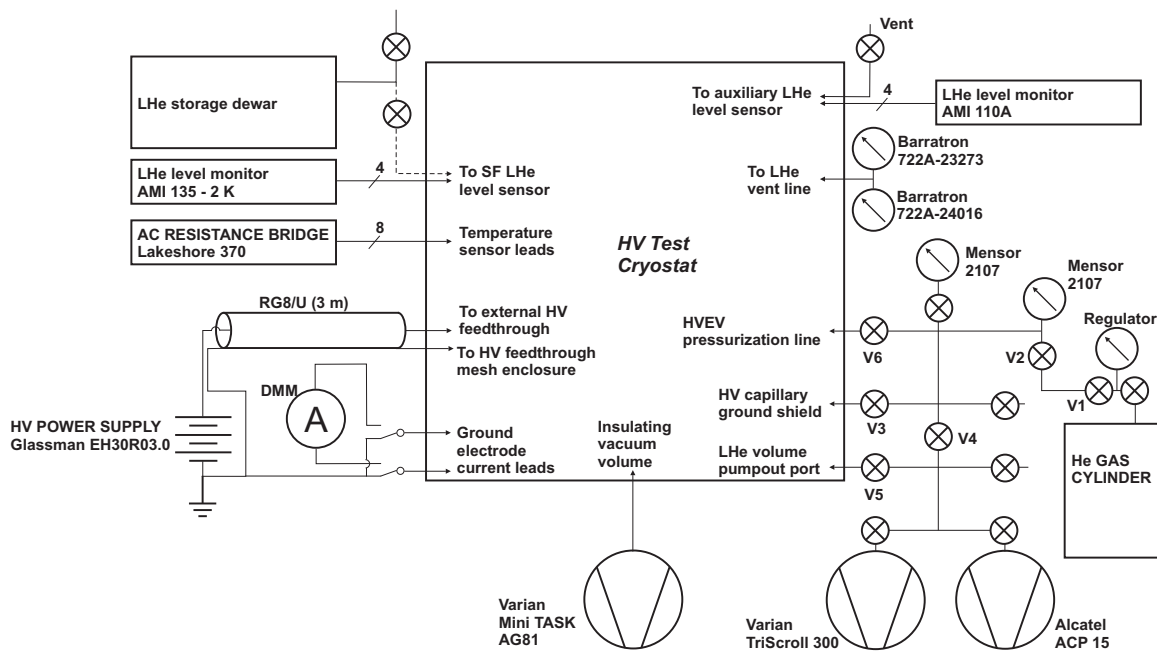


**Figure 4.19:** Complete HV experiment schematic. LHe level is monitored from fill port after LHe transfer. HV capillary ground shield tube is purged through valves V1, V2, and V3, then evacuated through V4. Outer LHe volume is pumped through V5. HVEV is pressurized through V1, V2, and V6.

The HVEV contains two  $\text{RuO}_2$  temperature sensors (Fig. 4.15), which are also used as LHe level sensors. One sensor is just above the electrode gap to indicate when the gap is immersed in LHe. The second temperature sensor is placed near the outlet of the pressurization line at the top of the HVEV (Fig. 4.15) to indicate when gas is entering. The temperature sensors are read out with a resistance bridge.

The LHe thermal bath in the top-loading outer cryostat (Fig. 4.18) has a volume of 8 liters. The temperature of the bath is controlled by evaporative cooling using one or two dry mechanical pumps.

There are two liquid level sensors in the thermal bath volume. One sensor is not calibrated for SF LHe, but gives a consistent indication of the  $\lambda$  transition when the level reading increases dramatically due to film flow. The second sensor gives an accurate level reading of both normal state and SF LHe.

Vapor pressure of the outer LHe bath is monitored using two capacitance manometers, with ranges of 0–10 and 10–1000 torr and resolutions  $1 \times 10^{-3}$  torr and 0.1 torr, respectively. Pressure monitoring allows for cross-checking with known saturated temperature data.

## 4.6 Breakdown in helium gas

Measurements of electric breakdown in helium gas were necessary in order to establish a baseline which could be more readily compared with previous measurements. Specifically it was valuable to obtain an accurate Paschen curve for helium gas using the cryostat. The same standard purity treatment was applied to the gas measurements as to liquid measurements:

1. the system was pumped and kept at vacuum for several minutes
2. then filled with high purity helium gas which passed through a copper coil liquid



nitrogen trap

3. repeat steps 1 and 2 at least two more times.

An advantage of measurements with gas is that the pressure is more easily controlled as opposed to the vapor pressure of a constantly boiling liquid. Typically measurements began at high pressure (slightly above atmosphere) and a vacuum pump was used to decrease the pressure in steps. Between three and five breakdown points were taken at each pressure and the average and standard deviation reported.

An early measurement of the helium Paschen curve in the cryostat is shown in Fig. 4.20. While the measured curve maintains the general Paschen trend it satisfied only two of the three features.

While the curve of Fig. 4.20 shows a quasi-linear trend with pressure above the minimum and an abrupt recover below the minimum, the minimum itself however is not well-defined and is quite broad spanning more than a decade. Repetitions of the measurement with improved purity and using constantly flowing helium gas produced the same broad minimum.

Some thought was required to solve the puzzle of the broad minimum of the measured Paschen curve. Recalling the breakdown criterion,

$$\gamma \exp(\alpha d) = 1 \quad (4.38)$$

where  $d$  is the gap size and  $\alpha$  and  $\gamma$  are the first and second ionization coefficients. When the second ionization coefficient becomes nonzero then the breakdown probability increases rapidly. For a given gap size, as the electric field is increased then  $\alpha$  increases until eventually  $\gamma$  becomes finite. The minimum of the Paschen curve,  $(pd)_{min}$  corresponds to the lowest breakdown voltage,

$$V_b[(pd)_{min}] = V_{min} . \quad (4.39)$$

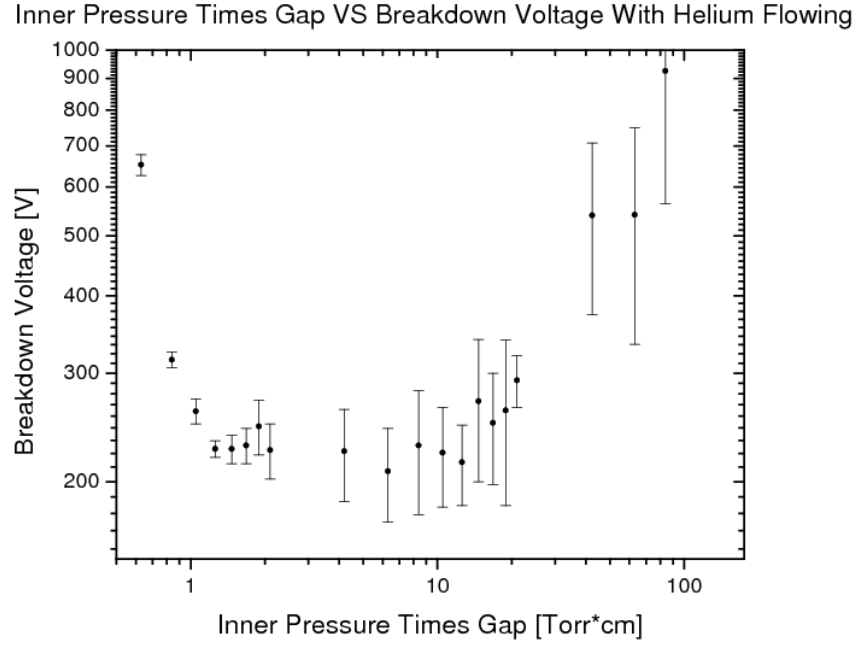


**Figure 4.20:** *Measured helium Paschen curve in the cryostat with very broad minimum.*

The  $(pd)_{min}$  region defines the ionization (*viz.* charge multiplication) region of highest efficiency. The factors which determine the efficiency are the energy gain of charges along the longitudinal mean free path and, more importantly, the product  $\alpha d$ . This has the straightforward implication that smaller gaps require larger fields to produce an amount of charge comparable to that in larger gaps with smaller fields to satisfy the breakdown criterion.

System configurations situated below the Paschen curve are stable against breakdown while configurations on or near the curve are metastable and those above the curve will be unstable. Measurements then consist of maintaining a fixed pressure and approaching the Paschen curve vertically from  $V = 0$  until breakdown. This

supposes, however, that the breakdown gap  $d$  is known and fixed and indeed this is a common assumption and one which persisted in this investigation for a while. This fixed breakdown gap has been assumed to be the smallest distance between the high voltage electrode and ground, where the field is strongest, and without direct observation inside the system in its various pressure-temperature configurations it was assumed that sparks landed on the ground electrode. Post measurement inspections of the ground electrode supported this assumption with distinct damage to the electrode surface.

A careful understanding of the breakdown mechanism shows that breakdown can only occur where the necessary criterion Eq. 4.38 is satisfied. The breakdown criterion is not a statement about local electric fields; rather, it is a requirement that sufficient primary ionization with ample kinetic energy to cause secondary ionization be present over a distance large enough to sustain an electron avalanche. If the ionizable material between the two electrodes is too sparse then charge multiplication will not take place to a sufficient degree and most charges will simply cause a leakage current. If, on the other hand, the ionizable material is too dense then electrons will not acquire enough energy between collisions to ionize and avalanching will not occur.

The primary ionization coefficient depends on the density of ionizable material through the pressure, Eq. 4.20. When charge multiplication occurs it is possible that the distance is too short for self-sustaining discharge. This is a qualitative statement about the Paschen law and explains why the breakdown strength should increase both below and above some critical pressure, in this case  $(pd)_{min}$ .

Figure 4.21 shows a schematic of the inner volume feedthrough and electrodes. Shown in the figure are three sample distances, including the electrode gap, between the high voltage and grounded surfaces. This defines three characteristic gaps for the system each of which can satisfy the breakdown criterion:

$$\gamma_1 \exp(\alpha d_1), \gamma_2 \exp(\alpha d_2), \gamma_3 \exp(\alpha d_3) . \quad (4.40)$$

As the voltage is increased at a given pressure, the first criterion to reach a value of 1 determines for which of the  $\{\gamma_i, d_i\}$  breakdown occurs. These are just three possible effective gaps where breakdown can occur but the actual number of effective gaps is a much higher nearly continuous distribution between the smallest and largest of the  $d_i$  and is determined by the electric field lines. This follows since electrons in their path from cathode to anode will avalanche approximately along field lines. The length of the field line then defines approximately the effective gap length and this length where breakdown occurs depends strongly on pressure.

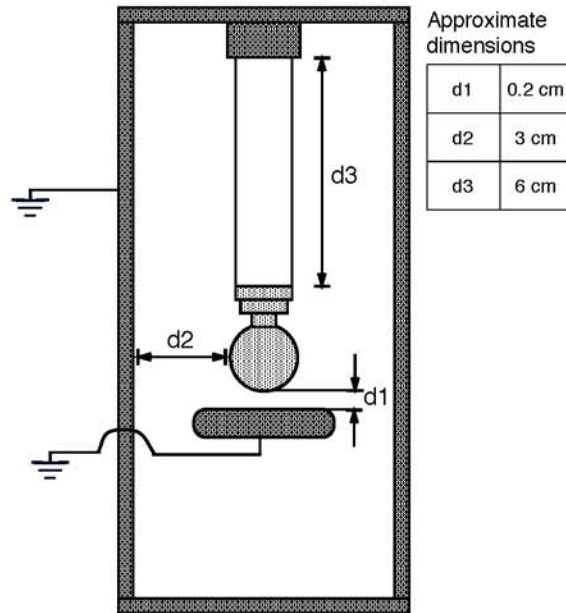


**Figure 4.21:** *An example of three effective gaps for breakdown inside the inner volume.*

To each of the  $d_i$  there corresponds a pressure  $p_i$  such that

$$V_B[p_i d_i] = V_B[(pd)_{min}] = V_{min} \quad (4.41)$$

where  $V_B(x)$  is the Paschen curve and  $(pd)_{min}$  is the position of its minimum. This means that for a configuration with several fixed distances between electrodes (or between high voltage and any grounded conductors) the place where breakdown occurs will actually depend on the pressure and not the distance to the nearest grounded conductor. More generally, there exists a bijective relationship between the set of possible gaps  $\mathbf{D}$  and the set of pressures  $\mathbf{P}$ :

$$\forall d_i \in \mathbf{D} \exists p_i \in \mathbf{P} | \gamma e^{\alpha(p_i)d_i} = 1 . \quad (4.42)$$

Note that by definition the breakdown criterion is always satisfied on the Paschen curve. The above relation is thus another way of expressing the Paschen law but in a way which highlights the close relationship between the geometry of the configuration and the operating pressure. Specifically, one must consider the entire set  $\mathbf{D}$  in a study of breakdown voltage and its dependence on pressure. This has an implication that pressures can exist for which breakdown occurs neither in the region of densest equipotential lines nor inside the smallest electrode spacing. It is possible to gain insight into  $\mathbf{D}$  by examining a map of electric field lines around electrodes and any other proximate conductors in the system. Figure 4.22 shows an Ansoft Maxwell electrostatic field simulation for the electrode geometry highlighting the diverse lengths,  $d_i$ , of field lines.

The range of lengths of field lines in Fig. 4.22 indicates the possible range of  $d_i$  which accounts for the broad minimum of Fig. 4.20. Even in the absence of the steel can around the inner volume the distribution of effective gaps spans almost an order of magnitude between the high voltage electrode and ground plate. With the can installed the range of gaps spans approximately an additional order of magnitude. Generally speaking the Paschen law is valid only for uniform or near-uniform

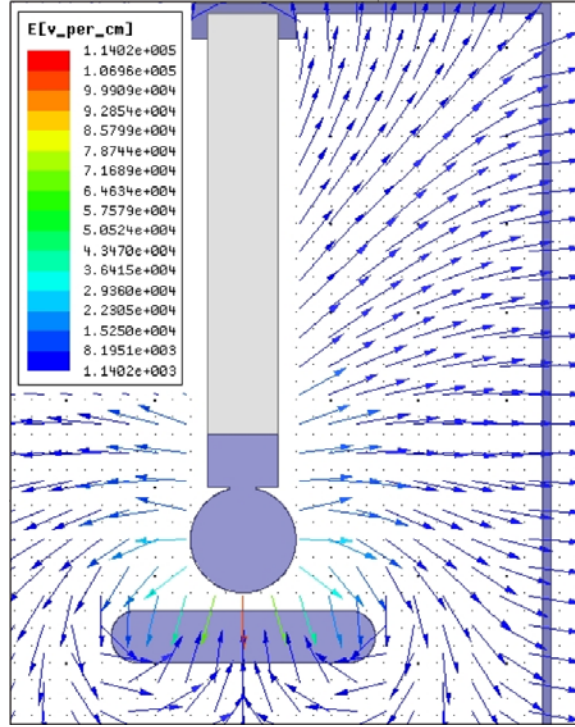


**Figure 4.22:** *Electric field lines inside the inner volume, with Ansoft Maxwell.*

fields. More precisely, however, in the case of non-uniform fields there can be a lack of information about  $d$ , not to mention many  $d_i$ , and this can translate into a misinterpretation of the Paschen relationship between  $pd$  and  $V$ . What is usually not considered in cases where deviations from the Paschen law are reported is the bijective relationship between  $\mathbf{D}$  and  $\mathbf{P}$  which satisfies the breakdown criterion, Eq. 4.42.

A range of several orders of magnitude in the  $d_i$  means that a measured breakdown curve with varying pressure would have a minimum that spans a range corresponding to the various minima  $\{(pd_i)_{min}\}$ . More generally, the breakdown voltage will be

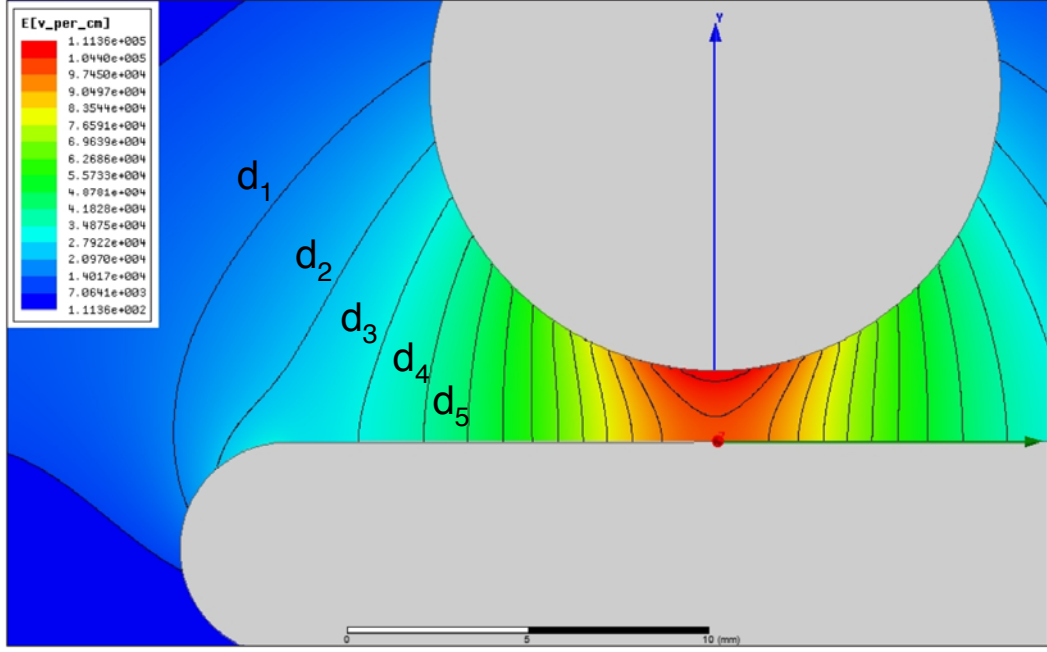


**Figure 4.23:** *Electric field strength in and around the electrode gap with  $HV = 20$  kV, with Ansoft Maxwell. Each field line that bridges the gap is a possible breakdown path at some pressure.*

given by

$$\min \left\{ \bigcup_{d_i \in \mathbf{D}} V_B(pd_i) \right\} \quad (4.43)$$

i.e., the Paschen curve must be evaluated for all  $d_i$  and the lowest  $V_B$  determines the breakdown voltage and its position.

One can construct a series of breakdown measurements, with carefully isolated and well-defined gap lengths, as a function of the pressure. Specifically, only one gap length must be present in the configuration at any time to guarantee that breakdown occurs only in the desired gap for any pressure. The resulting breakdown curves can then be superimposed. The lower envelope of the curves then denotes the effective

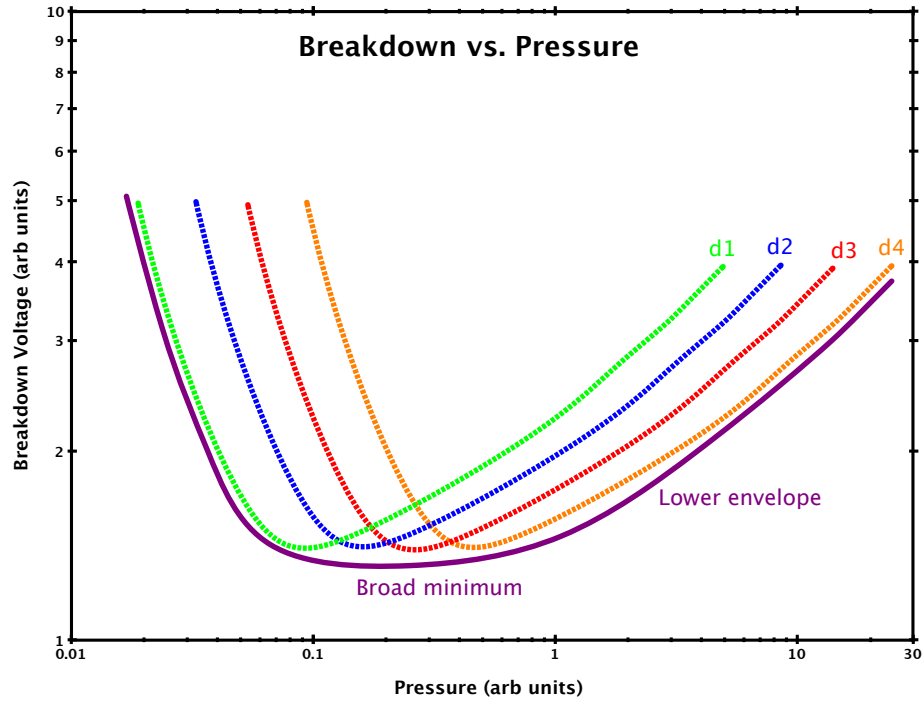


**Figure 4.24:** *Breakdown vs pressure curves for a system with four defined gap distances. Each curve could be obtained when exactly one gap length exists during the measurement. The resulting Paschen curve is the bottom envelope of the breakdown curves.*

Paschen curve that would otherwise be measured had no precautions been taken to isolate the gap lengths. This is what is meant by Eq. 4.43 and shown graphically in Fig. 4.24. Note that if the breakdown curves are superimposed as functions of  $pd$  then they should all collapse into the Paschen curve, modulo some small geometric effects such as tiny irregularities which will effect field emission and charge diffusion.

In light of the above discussion the next series of gas measurements was taken to isolate the minimum gap and prevent the breakdown region from varying with pressure. Figures 4.25 and 4.26 show a teflon assembly which was placed around the



two electrodes to limit breakdown to a very narrow region between the electrodes. Other conductors exposed to high voltage were wrapped in teflon tape.

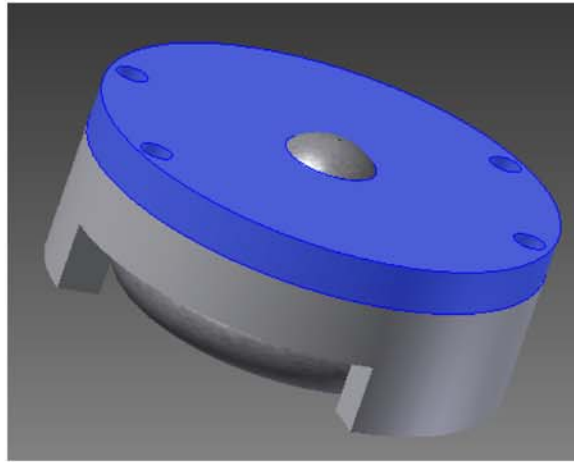


**Figure 4.25:** *Model of the teflon insulator around the electrodes.*

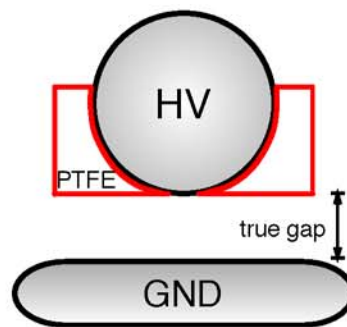


**Figure 4.26:** *Schematic of the teflon insulator around the electrodes.*

Figure 4.27 shows the measured Paschen curve when the high voltage electrode is isolated with teflon and the breakdown region confined. The well-defined minimum is now obvious and the behavior is in better agreement with the accepted helium

Paschen curve of Fig. 4.8. Figure 4.28 shows the Paschen curve as obtained when the electrodes are isolated using teflon from any other conductors at 77 K.

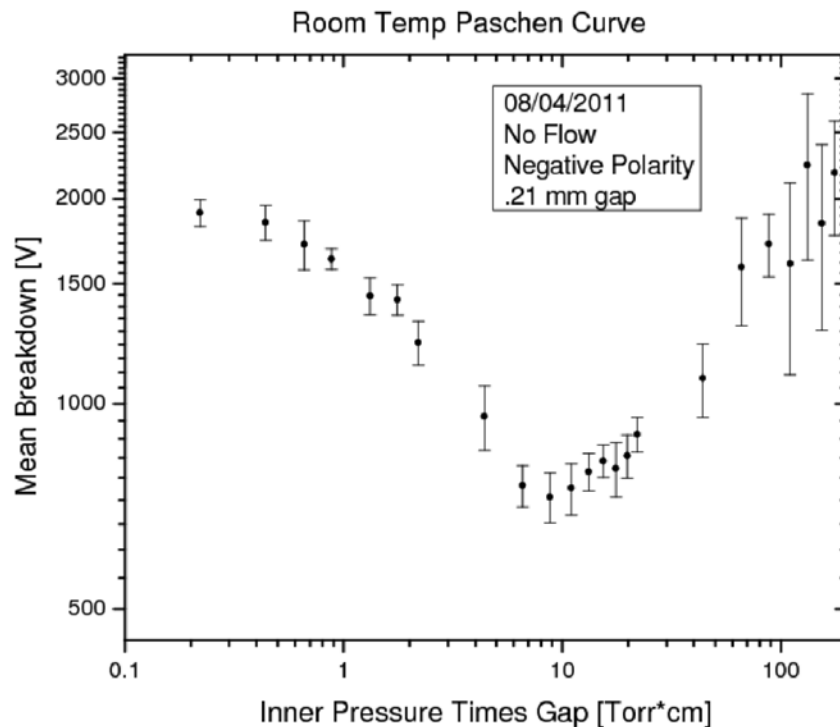


**Figure 4.27:** *Helium gas Paschen curve obtained with teflon isolation around the electrodes at 77 K. Liquid nitrogen was placed in the outer volume in an attempt to also reduce possible impurities.*

Paschen curves with broad minima were first reported only recently in [63] and attributed to various breakdown gaps in complex geometries in microelectromechanical systems. The authors studied breakdown in these systems at low pressures where the effects of multiple effective gaps are pronounced.

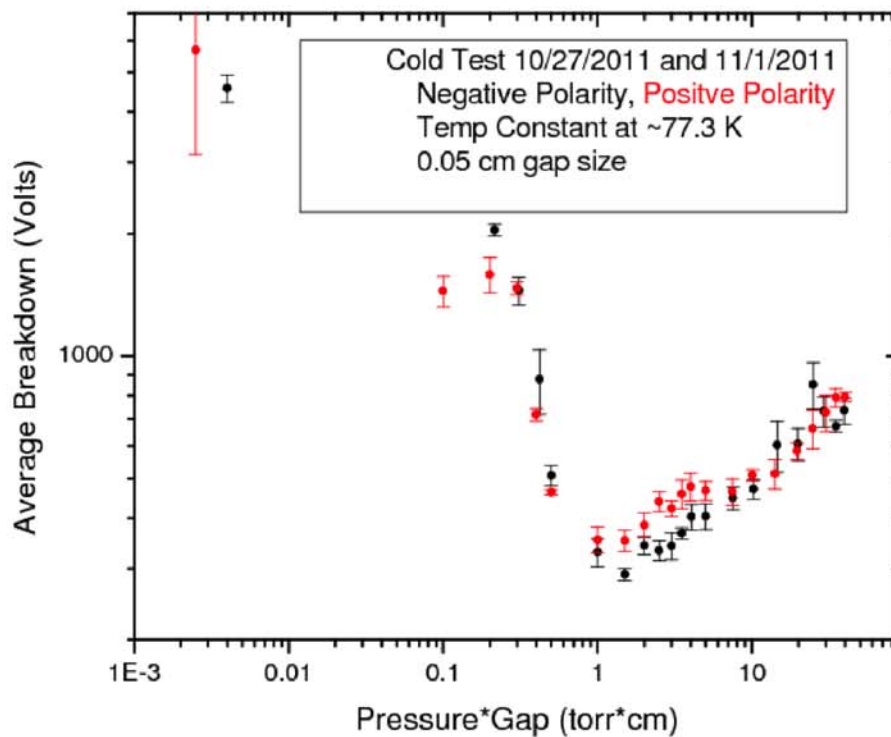


**Figure 4.28:** *Helium gas Paschen curve obtained with teflon isolation around the electrodes at 77 K. Liquid nitrogen was placed in the outer volume in an attempt to also reduce possible impurities.*

Going from 300 K to 4 K the electrode gap was expected to change but it was not clear whether it would grow or shrink. To test this, a capacitive divider was fitted to the cryostat where the capacitance of the electrode gap could be monitored relative to a fixed capacitance. Figure 4.29 shows the schematic. A room temperature calibration curve was established where the voltage output across the electrode gap was correlated to the measured gap size. Then at low temperature the voltage output can be monitored again to establish the position on the calibrated curve, Fig. 4.30. It was found that the electrode gap size did not change significantly upon cooling to

4 K. The change in capacitance was consistent with the change in dielectric constant after filling with LHe.

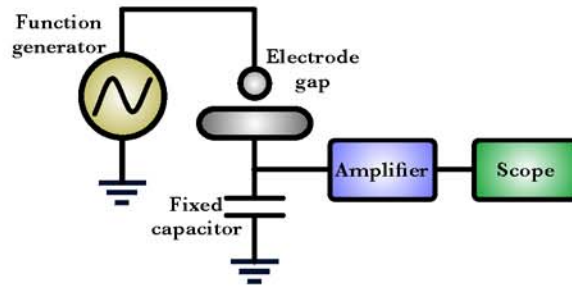


**Figure 4.29:** Schematic of capacitive divider used to monitor the change of gap at low temperature.

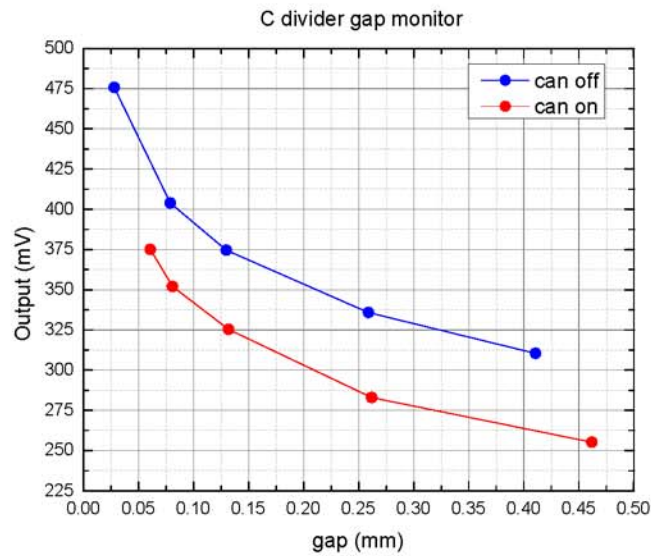


**Figure 4.30:** Calibration curve used to deduce the relative change in electrode gap size at low temperature.

The behavior of liquid helium under electrical stress is not fully understood, in particular the conditions leading to electric breakdown in both normal and superfluid states well above the saturated vapor pressure. Some work has previously been done studying breakdown in He-I but little work has been done to study breakdown in He-II off the saturation curve. Here we report a system implemented to study breakdown in He-I and He-II and effectively decouple temperature and pressure effects with a good degree of reproducibility. Utilizing various paths on the  $^4\text{He}$  pressure-temperature phase diagram we have observed hysteretic behavior in electric breakdown. The measured dielectric strength of liquid Helium was greatly increased relative to saturation curve cooling and appears consistent when interpreted as the suppression of nucleation sites on electrode asperities.

Studies of electrical breakdown in liquid dielectrics have been ongoing for a number of years. Relatively recently there has been renewed interest in understanding electrical breakdown in cryogenics, for example cryogenics used as coolants and insulants in superconducting devices.

## 4.7 Electric Breakdown in Liquid Helium

Electric breakdown in gases is well-described by Paschen's Law which relates breakdown voltage to the product of gas pressure and distance between the electrodes. The physics follow from the Townsend theory of breakdown. Breakdown in liquids, however, remains an active area of research, but appears consistent with the Townsend theory.

A pre-breakdown phase precedes the propagation of a spark between electrodes [64]. The pre-breakdown phase is reflected by the vaporization of liquid where avalanching leading to breakdown occurs inside gaseous regions within the liquid. This process is what generally makes some liquids good dielectrics, however the pres-

ence of vapor bubbles inside the liquid can jump-start Townsend avalanches. Kao and McMath [65] and references therein observe hydrostatic pressure dependences of breakdown which seem to favor a bubble-initiated mechanism. Thus, electronic and gaseous processes appear to be related during breakdown [64].

In [66] and [67] the authors put forth a model of breakdown in liquids based in large part on microbubbles. According to the authors, understanding of the physics involved in the initiation of breakdown is incomplete and assuming a purely liquid-based phenomenon makes explaining the breakdown process difficult. Specifically, the creation of free electrons and with enough energy for impact ionization to take place is very unlikely in an electrode-liquid interface. It is much more likely that local field enhancements due to electrode surface asperities or the presence of microbubbles are responsible for the onset of impact ionization.

In [66] the authors observed a dependence of the breakdown voltage in oil on the hydrostatic pressure, in agreement with a bubble-based approach. This suggests that a higher hydrostatic pressure would either inhibit bubble formation or reduce the size of bubbles, probably both. In addition the authors report decreases in breakdown voltage with decreasing pressure. The authors note that polishing the anode is particularly important. Finally, the authors postulate that breakdown is initiated with field emission into microbubbles which are likely to be scattered throughout the bulk liquid and electrode surfaces. Field emission would take place at the vapor-liquid interface of the bubble. Once inside the bubble, electrons would be accelerated by the electric field and gain enough energy for the onset of impact ionization. In this way, microbubbles at the electrode surface and inside the bulk liquid act as local sources of charge. A simple calculation shows that for a typical field of 100 kV/cm, it is possible for an electron to gain up to 1 keV across a 100  $\mu\text{m}$  bubble, well in excess of the energy required for impact ionization. A tiny bubble on an electrode surface could then greatly expedite the onset of breakdown.

Lohse [68] says surface crevices and impurities can be host to submicron bubbles and contribute significantly to the nucleation process. Thus it is critical to eliminate any residual sources of gas such as dissolved gases, microbubbles on surfaces and, in the case of cryogenics, heat sources which can lead to vaporization.

Breakdown in LHe is interesting to study and challenging to understand. A number of studies in LHe have been carried out which are consistent with the mechanisms thought to dominate breakdown in liquids.

Hong et al. [69] note that the shape of vapor bubbles under electrical stress becomes elongated in the direction of the electric field. Breakdown is observed inside vapor when the vapor bubble bridges the electrode gap. Bubbles remained on the electrode surface longer in the presence of the electric field than without. The authors also observed an increase in breakdown strength with increasing pressure in liquid Nitrogen.

This is supported by Hara et al. [70] who also studied the influence of thermally created bubbles on breakdown but in LHe. The authors noted that bubbles can be generated in three ways: the release of gas from a microscopic cavity on the electrode, local vaporization due to electrical current, and the motion of solid impurities. They observed elongation of bubbles inside the gap along the field direction and that breakdown occurred inside a vapor bridge between electrodes. The onset voltage for breakdown inside the vapor bridge is then much lower than the breakdown voltage without a vapor bridge, consistent with breakdown inside gas.

Schmidt et al. [71] note the improbability of Townsend breakdown inside LHe; it is unlikely for Townsend breakdown to occur in bulk liquid. It seems likely instead that the presence of gas domains inside the liquid is required to initiate a Townsend breakdown.

Hara et al. [72] have done studies in slightly pressurized He-I and II, near the saturation curve. They observed an improved breakdown strength in the pressurized

state but do not report any hysteresis.

Blank and Edwards [73] studied breakdown as a function of temperature, down to superfluid, near the saturation curve. They observed a decline in the breakdown strength with decreasing temperature using spherical electrodes. A polarity test using point-plane geometry also suggested electron field emission taking place at the cathode.

An important hurdle to overcome when dealing with cryogen dielectrics, in addition to gas bubbles, are contaminants such as dust, other impurities and heat sources. Dust and impurities can greatly increase the stability of vapor bubbles, e.g. by affecting their geometry and surface energy making them mechanically highly stable. It is also possible that solidified contaminants may act as ion channels between electrodes.

Generally speaking, there does not exist an abundance of breakdown studies in He-II and only one known study of breakdown off the SVP curve with He-II by Hara's group.

The primary goal in the design of our system to measure dielectric behavior of LHe was the decoupling of temperature and pressure effects. This was motivated by studies of breakdown in LHe at LANL [?]. In their experiment, temperature was controlled by evaporative cooling of the bulk liquid. Consequently, it was not possible to easily extrapolate the causes of breakdown.

Our test system uses a straightforward procedure to study breakdown dependence on temperature and pressure separately in He-I and He-II. Furthermore, by using a thermal bath the system is not confined to evaporative cooling along the saturation curve and can thus probe breakdown behavior in regions in phase space not previously explored..



## 4.8 Procedure

### 4.8.1 System Preparation and Cooling

In order to minimize contaminants, the electrodes, washers, and G10 support structure are subject to a final ultrasonic cleaning in acetone and alcohol prior to assembly. All other HVEV components are solvent-cleaned by hand and dusted with compressed He gas.

To ensure the basic integrity of the electrical connections and insulators before cryogenic operation, an electric breakdown test in air is performed. With the HVEV still outside the cryostat and the enclosure removed, the HV conducting line is evacuated and the conductor attached to the HV power supply. The voltage is ramped by hand at approximately  $100 \text{ V s}^{-1}$  until a spark is observed between the electrodes near the nominal breakdown field of air ( $\sim 30 \text{ kV cm}^{-1}$ ) at STP.

The HVEV is then closed and inserted into the outer cryostat. Both the HVEV and the HV conducting line are pumped to roughing pressure and purged 2-3 times with He gas to further reduce contaminants. To test all HVEV joints for basic leak tightness, especially the SF-tight needle valve, the HVEV is filled with He gas with the needle valve closed while the outer cryostat LHe volume is pumped to roughing pressure.

The insulating vacuum volume on the outer cryostat is pumped to a pressure of about  $1 \times 10^{-3}$  torr. Filling of the liquid nitrogen volume in the cryostat induces sufficient cryopumping after which the vacuum pump may be switched off to reduce vibrations.

To reduce the possibility of air contamination while filling the system with LHe, a slight over-pressure of He gas is established in the HVEV via the gas manifold, and the SF-tight valve on the HVEV is opened. Commercial-grade LHe is then transferred

to the outer cryostat, with no liquid nitrogen pre-cool. Once stable transfer has been established, the He gas flow from the manifold is stopped and the HVEV fills with LHe from the outer bath through the SF-tight valve. The HVEV is inferred to be full when the upper temperature sensor near the gas inlet stabilizes near 4.2 K.

Complete cool-down of the system from room temperature to 4.2 K takes on the order of 1 hour. The outer bath volume is usually given a full 8 l charge of LHe. Depending on the measurement carried out, a sufficient amount of LHe can remain in the system for up to 4 hours when pumping or pressurizing, or about 12 hours when left undisturbed.

#### 4.8.2 Pressure and Temperature Control in the $^4\text{He}$ Phase Space

The experiment is designed to be able to test the dielectric strength of  $^4\text{He}$  at any point in the liquid portions of the phase space bounded by  $1.8 \text{ K} \leq T \leq 4.6 \text{ K}$  and  $10 \text{ torr} \leq P \leq 1000 \text{ torr}$ . In practice, HV breakdown tests are performed at different points along various paths in the phase space. Paths are chosen in part for convenience and as dictated by results as they are obtained.

One such path, used in early sets of measurements in the experiment, is illustrated in Fig. 4.31. It was chosen to explore the dielectric strength along the  $^4\text{He}$  vapor pressure curve, followed SF near atmospheric pressure. The steps are:

- a. The HVEV and outer volumes are filled with normal state LHe at atmospheric pressure.
- b. The outer volume is pumped to cool the system along the vapor pressure curve. The SF-tight valve on the HVEV is kept open so that this volume also cools along the vapor pressure curve. The pump is allowed to work until the lowest

desired temperature is reached. The cooling rate can be controlled somewhat by throttling the pump, but fine control is difficult along this path. With an  $8 \text{ l s}^{-1}$  pump fully opened to the cooling line, it takes about 30 minutes to cool the system from 4.2 K to 2.17 K. The  $\lambda$ -transition occurs near 37 torr and 2.17 K according to the pressure gauge on the outer volume and the temperature sensors inside the HVEV. During the transition, the level sensor not calibrated for SF usually indicates a level increase of 100% or more.

- c. The SF-tight valve is closed, and commercial-grade He gas is introduced into the top of the HVEV to bring this volume to the desired pressure (in this case 1 atm). The vacuum pump on the outer bath is left running, but the gas must be introduced slowly since the initial pressure increase is quite rapid due to vaporization of some of the LHe in the HVEV. There is a significant temperature increase, but the desired pressure can be attained after a few minutes, with liquid still well above the electrode gap. The vapor in the upper part of the HVEV re-liquifies several minutes after the final pressure is attained. The pressure in the outer volume also tends to increase in response to the He gas influx in the HVEV, but usually by no more than 100 torr.
- d. The pump on the outer volume resumes cooling the HVEV, now maintained at constant pressure. Adjusting the He gas flow by hand with the regulator is sufficient to keep the HVEV pressure constant to within 1 torr. A significant reduction in flow is usually required only once during this process, at the instant when all the vapor at the top of the HVEV re-liquifies.
- e. Once the lowest desired temperature is reached (in this case 1.8 K), the system is decompressed by reducing the He gas flow with the regulator. Any desired pressure between the maximum set previously and the He vapor pres-

sure can usually be attained very quickly and maintained to within 1 torr for at least several minutes. Near the lowest practical temperatures attainable by the outer bath pump, the temperature changes very little during this step and the decompression is almost purely isothermal. Higher-temperature, isothermal decompressions are possible by simultaneously throttling the outer volume pump.

Since pressurization of the HVEV is a dynamic process, with gas liquifying and flowing past the pressure gauge, it was necessary to verify the actual HVEV pressure. To that end, a second pressure gauge was added to a static line (sharing instrumentation wires) coming from the HVEV which was not susceptible to effects of gas flow. A full breakdown measurement was conducted with this second pressure gauge and the system was put through the pressurization cycle outlined in Figure 4.31. Figure 4.32 shows the resulting pressure measurements with the inlet pressure measured at the incoming gas line and the outlet pressure measured in the static line. It was found that the pressures matches very closely and the time lag of the outlet pressure was on the order of seconds, far below the time scales of the measurements.

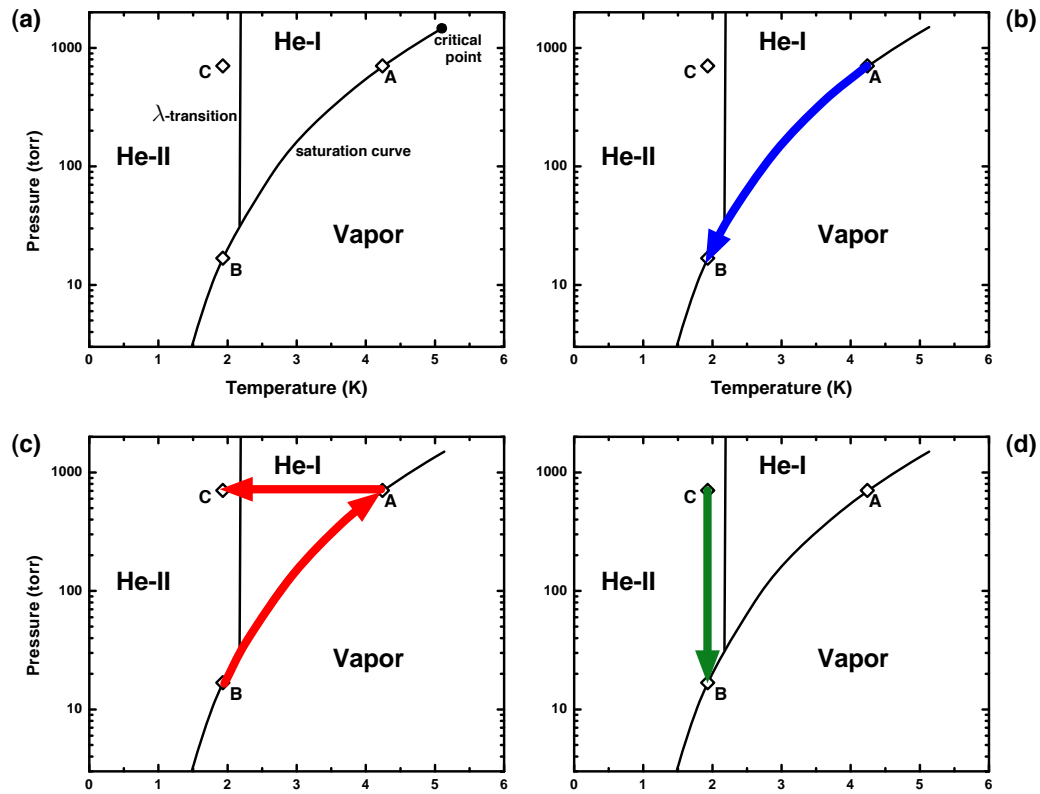


**Figure 4.31:** (a)  $^4\text{He}$  pressure-temperature ( $P$ - $T$ ) phase diagram with points A, B and C forming the corners of the probed phase space. (b) Cooldown stage from LHe transfer to superfluid.  $P_A = 760\text{ torr}$ ,  $T_A = 4.2\text{ K}$  and  $P_B \leq 25\text{ torr}$ ,  $T_B \leq 2.0\text{ K}$ . (c) Pressurization stage and subsequent isobaric cooldown.  $P_C = 760\text{ torr}$ ,  $T_C \leq 2.10\text{ K}$ . (d) Isothermal de-pressurization stage inside superfluid.

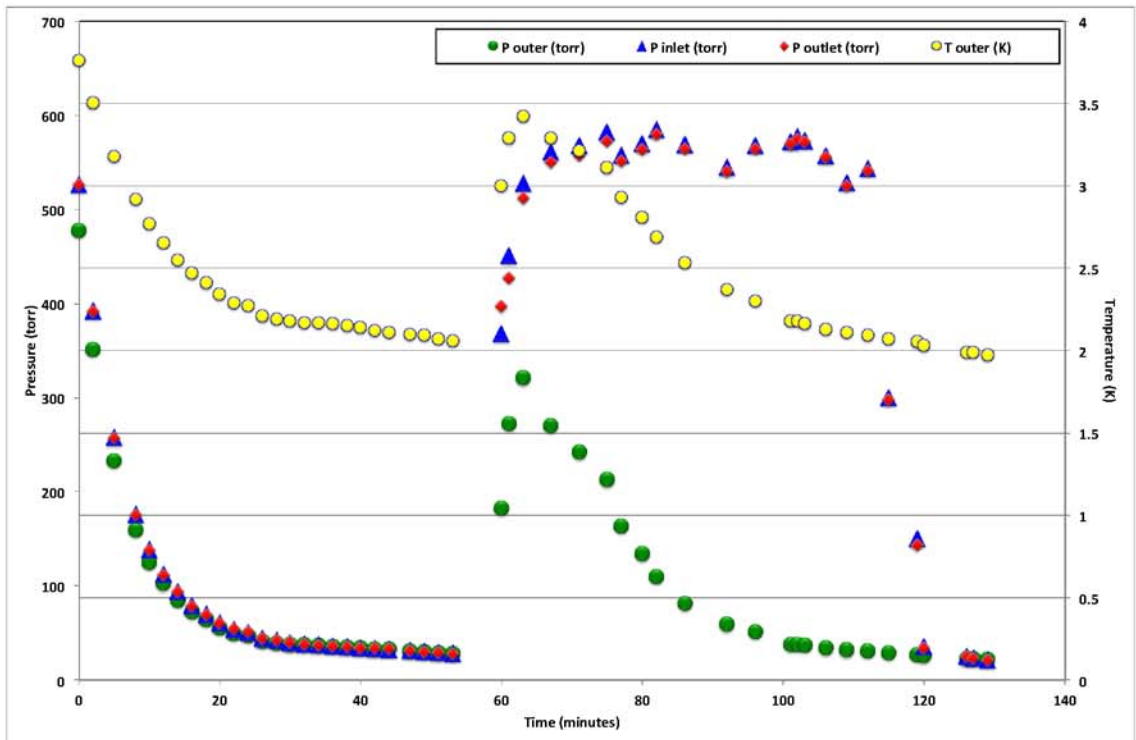


**Figure 4.32:** Comparison of the inlet (blue) and outlet (red) HVEV pressures. Also plotted are the outer pressure (green) and the outer temperature (yellow).

### 4.8.3 High Voltage Measurements

Dielectric strength measurements are taken at many points along the cooling and decompression branches of the paths explored in the  $^4\text{He}$  phase space. Irrespective of the pressure and temperature, the procedure is as follows:

1. HVEV temperature monitors are switched off to prevent anomalous readings and damage in the event of spark discharges.
2. The HV power supply is switched on with the voltage set to zero and the current limit set to a few tens of microamps.
3. The voltage was initially ramped by hand from 0 V at a rate of about  $100 \text{ V s}^{-1}$ . Later improvements allowed the voltage to be ramped using a MATLAB script by interfacing with the power supply.
4. Voltage and current readings are visually monitored for fluctuations. In the event of a current fluctuation of at most a few microamps, and/or a voltage fluctuation of at most a few kV, a partial discharge is assumed and the ramp is paused to permit the system to stabilize.
5. Dielectric breakdown is indicated by a rapid current surge of several microamps or more and a rapid drop in the voltage of several kV or more. On occasion these signals are accompanied by an audible spark. In the event of a breakdown the power supply is ramped down and switched off. (Later tests utilize a power supply with a trip-mode option, making this step automatic.)
6. As soon as possible, the HVEV temperature monitor is powered on and all relevant data are recorded by hand: breakdown voltage, HVEV pressure and temperatures, outer volume bath pressure and liquid level.

7. The system is allowed to recover for 1-2 minutes, and the process is repeated once or twice. The dielectric strength reported is the average of the breakdown voltages attained. Additional measurements are made in the event of unusually discrepant readings at a particular temperature and pressure point.

Data are recorded as soon as possible after a breakdown event for consistency. Pressure and temperature can change significantly during the ramp, which can take as long as several minutes, or during the 1-2 minute recovery time between data points for the same nominal temperature and pressure. However, these changes exceed a few percent only for when the system is cooling along the vapor pressure curve above  $\sim 3$  K ( $\sim 150$  torr), which takes place rather quickly. Most of the measurements of interest take place at HVEV temperatures below 2.2 K, where the pressure varies by less than 0.5 torr during a typical HV measurement.

The 1-2 minute recovery time is determined empirically and presumably corresponds to the time interval after which any (low dielectric strength) vapor created by the previous discharge has sufficiently cleared from the space between the electrodes. During this time, no adjustments are made to the HVEV pressure or outer bath temperature save occasional minor ones to keep them stable.

## 4.9 Results & Discussion

### 4.9.1 Electric Breakdown Hysteresis

Referring to Fig. 4.31, breakdown data were taken along the paths A-B, then the inner volume was pressurized with (warm) helium gas which caused it to warm back to point A. Then breakdown measurements are taken along the path A-C until the temperature and liquid level meter indicate superfluid at point C. Then the inner volume is de-pressurized in steps by reducing the flow of helium gas to the inner volume



and breakdown measurements are taken along C-B. Point B is at SVP and usually measurements are taken for a while longer along SVP. For ease of interpretation breakdown data are overlaid directly on the phase diagram.

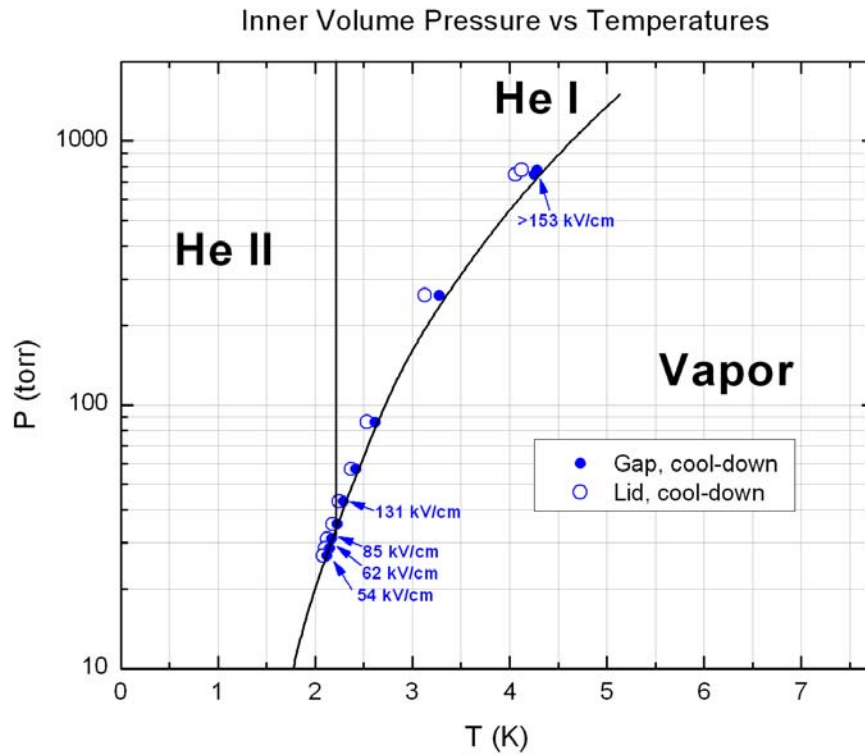


**Figure 4.33:** *Electric breakdown along SVP. The gap and lid temperatures correspond to two temperature sensors inside the HVEV.*

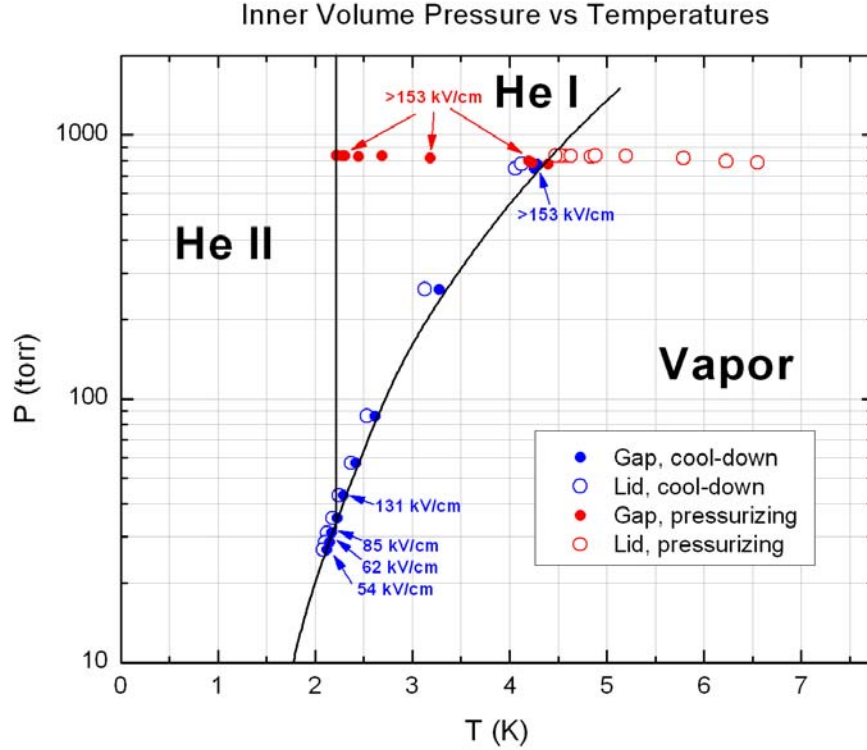
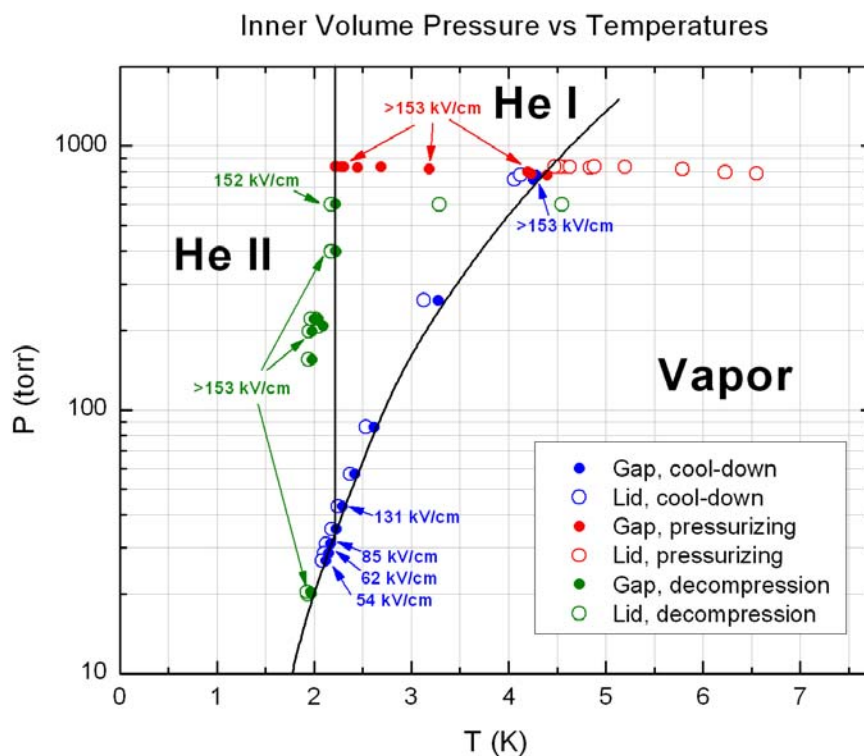


**Figure 4.34:** *Electric breakdown in the pressurized state, after measurements at SVP.*

Figure 4.33 shows breakdown results at SVP with hand polished, stainless steel electrodes, and the breakdown fields are calculated using the maximum voltage during ramp up before breakdown divided by the gap size. Points show the data taken during cooldown along the saturation curve. The first measurement (top-right most point, taken at 1 atm and 4.2K) indicates that no breakdown was observed. Instead, the power supply was able to maintain the maximum voltage rating of our feedthroughs, 20kV, which for that setup meant a field greater than 153kV/cm. Thus in normal

LHe at 1 atm the dielectric performance is relatively good. The steady decrease in breakdown field strength is typical for measurements made with handpolished electrodes above a certain threshold grit size.

Figure 4.34 shows data taken in the pressurized state. Note that the top (lid) temperature sensor reads vapor due to the incoming warmer gas but the lower temperature sensor ensures that the electrodes are always immersed in liquid. A significant decrease in breakdown strength at this point would mean the electrodes were exposed to vapor. The pressure is maintained while cooling is provided by the outer bath until superfluid is reached.



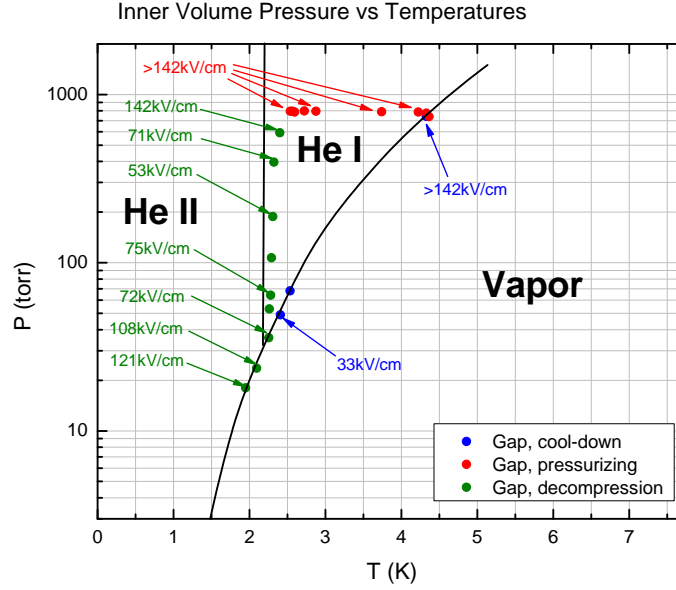
**Figure 4.35:** *Electric breakdown along SVP*

Figure 4.35 shows the de-pressurization stage. De-pressurization is performed in steps by fine control of the gas regulator; reducing the flow creates a lower pressure equilibrium state. This enables further breakdown data to be taken at constant pressure along the depressurization stage. The hysteresis becomes apparent when the saturation curve is reached at the end of the de-pressurization: no breakdown occurs on the saturation curve after de-pressurization. This is in stark contrast to the breakdown measurements along the saturation curve using evaporative cooling which typically occurred below 1 kV.

The onset of this hysteresis is observed also when using lower magnitudes of pressurization when performing the cycle in Figure ???. We have observed that pressurizing as low as 100 torr was sufficient to recover the high breakdown field post-depressurization.

#### 4.9.2 Pressurization Cycle in He-I

We also performed the cycle ABACB in He-I only, remaining above the  $\lambda$  transition until the end of the depressurization stage. As before, there is full recovery of the dielectric strength upon pressurization, however recovery is only partial during and after depressurization. This suggests that the  $\lambda$  transition is useful in enhancing the barrier against breakdown. In particular, it seems that for the electrode condition used in this experiment, traversing into He-II in the pressurized state appears to do more to inhibit the onset of breakdown. Figure 4.36 shows the pressurization cycle data plotted on the phase diagram.



**Figure 4.36:** *Pressurization cycle inside He-I.*

### 4.9.3 Agitated Superfluid

To test the possibility of breakdown hysteresis involving intrinsic superfluid properties, such as the suppression of elementary excitations, measurements were also made in agitated superfluid. A hypothesis floated within the nEDM collaboration that superfluid vortices could act as channels for charges between the electrodes. It was speculated that these charge channels could contribute to breakdown and their presence somehow contributed to the observed hysteresis.

A piezo-electric crystal oscillator (lead zirconate titanate, PZT) in the shape of a cantilever was used to agitate superfluid near the electrode gap. When an electric field is applied across the crystal, the crystal elongates along the direction of the field, thus by applying an alternating voltage to the PZT, it can be made to vibrate. To

achieve maximum deflection and speed at the tip the voltage needs to oscillate at a resonance frequency of the cantilever. This corresponds to an antinode at the tip of the PZT cantilever. The maximum deflection is achieved at the first harmonic. Figure 4.37 shows two different PZTs which were used for liquid helium breakdown tests. The resonance frequencies of the PZTs were found empirically by immersion in water. The long PZT shown on the left side of Fig. 4.37 had a resonance deflection slightly below 1 cm which did not change during immersion tests in water. For both types of PZT the resonance frequencies and higher harmonics were audible and could be verified by measuring the output low voltage side of the PZT since the amount of deformation was proportional to voltage.

If the PZT cantilever can be made to vibrate at a speed near the He-II critical velocity then it could generate excitations.

To test the effect of the PZT the system was put through the hysteretic pressurization cycle before switching on the PZT. Figures 4.38 and 4.39 show the post-pressurization cycle effect of the PZT. Operation of the PZTs near the gap did not have a significant reproducible effect on the breakdown strength. To account for that it seems more appropriate to suggest that the induced pressure waves instead of creating vortex channels may produce cavitation inside the liquid and contribute to the presence of vapor bubbles. Additionally, the pressure waves may perturb small vapor bubbles already present, either by physically displacing them or aiding in their condensation. Investigations with agitated superfluid were not pursued further since there was no way to gauge the effectiveness of vortex generation.

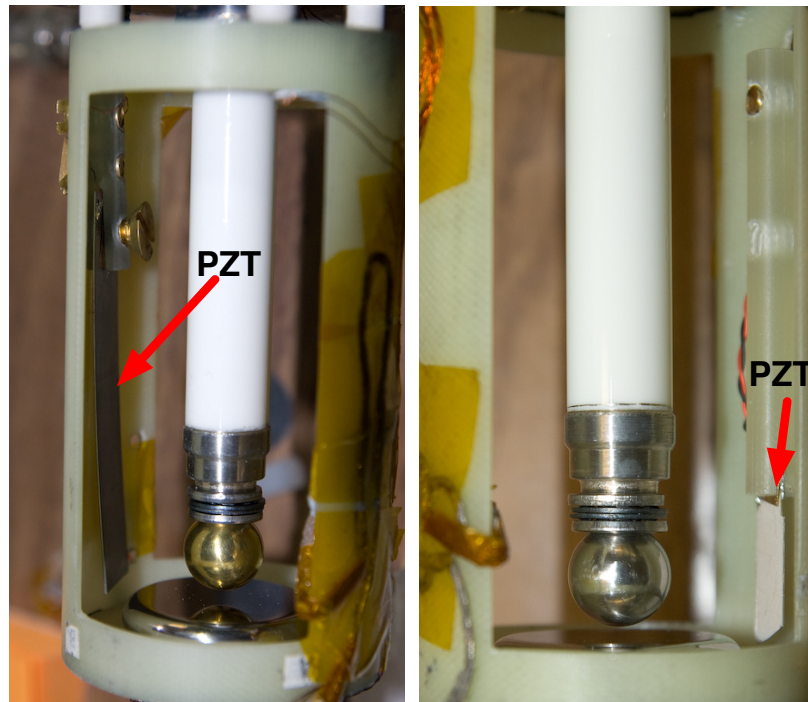


**Figure 4.37:** *Photos of electrodes and feedthrough showing two types of piezo-electric transducer (PZT) placed to agitate fluid near the gap.*

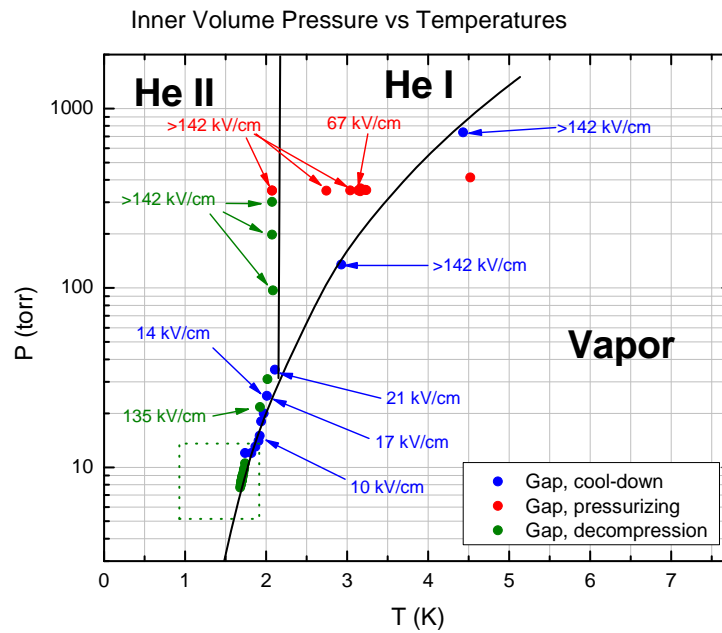


**Figure 4.38:** *Pressurization cycle with hysteresis applied before testing with PZT cantilever. The dotted green box shows the region where the PZT was operated.*



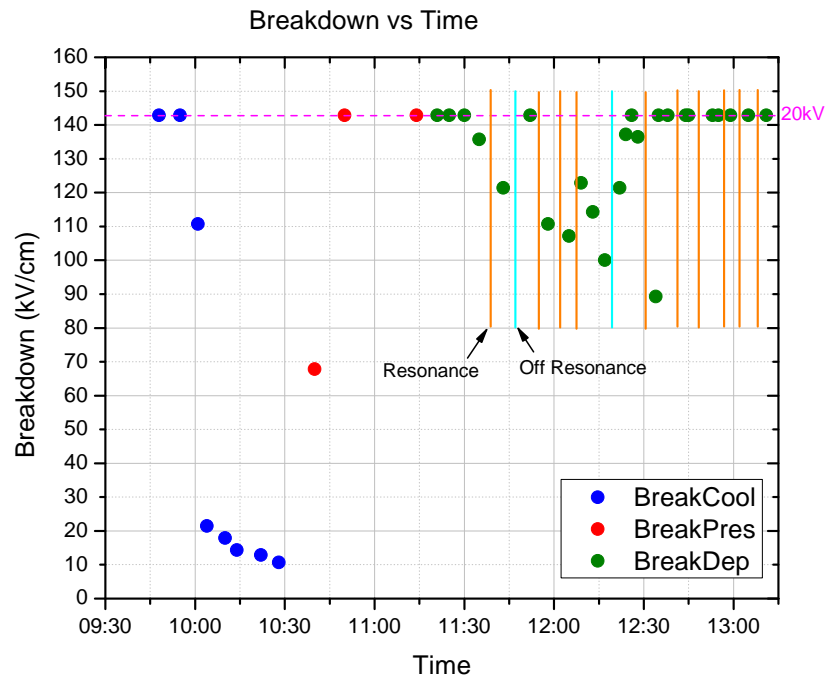


**Figure 4.39:** Evolution of breakdown strength with time, coinciding with Figure 4.38. The PZT was tested both on and off resonance as noted for about 30 seconds each time.

#### 4.9.4 Wetting Transition in Superfluid

M. Hara and colleagues [74] observed an increase in breakdown strength upon going through the  $\lambda$ -transition when vapor was generated by a conducting particle colliding with one electrode, Fig. 4.40. This could be attributed to the observed rapid collapse of the vapor bubble in He-II whereas in He-I the generated vapor bubble broke into many smaller bubbles which formed a vapor layer on the electrode. They also performed breakdown studies in slightly-depressurized and slightly-pressurized states by modifying the rate of vapor pumping although essentially still very near to SVP as seen in Fig. 4.41.

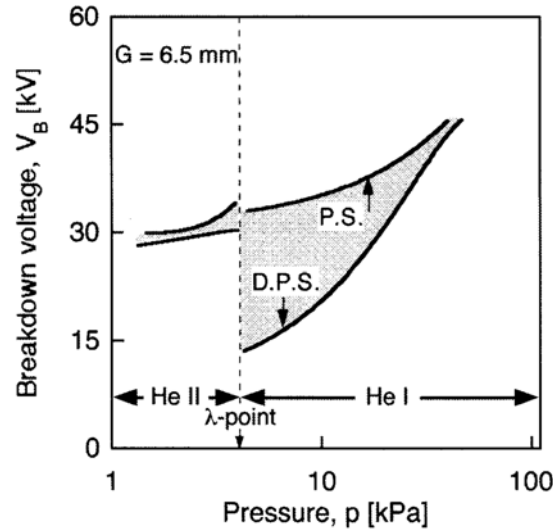


**Figure 4.40:** *Discontinuous breakdown voltage transition in the pressurized and slightly depressurized states, from [74]*

A possible effect due to the  $\lambda$ -transition was observed at IU as well. Figure 4.42 shows breakdown results when the SVP curve and the  $\lambda$ -transition are traversed multiple times. While breakdown decreases along SVP during the first cool down, it recovers dramatically during the warm up and subsequent cool down. There may be

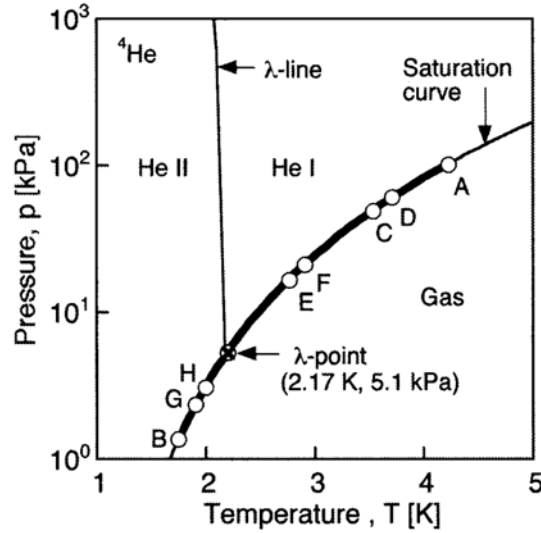


**Figure 4.41:** *Positions on the He phase diagram where breakdown measurements were made in [74]*

two explanations for this:

- during warm-up the liquid may be in a slightly pressurized state where trapped vapor bubbles become unstable and condense or their growth is inhibited
- the relatively violent boiling at the  $\lambda$ -transition could disturb the stability of trapped vapor bubbles and multiple transitions could have a ‘cleaning’ effect perhaps similar to PZT pressure waves.

Taborek and Senator [75] have observed a difference between wetting in He-I and He-II, in particular the film thickness in He-I is substantially less than in He-II. They concluded that He-I is not a highly-wetting fluid and that the  $\lambda$ -transition is also a wetting transition. There exists no viable theoretical explanation for this difference.

In addition to wetting transitions, wetting hysteresis is observed in a variety of systems [76] (and references therein). Wetting hysteresis in liquid helium can be

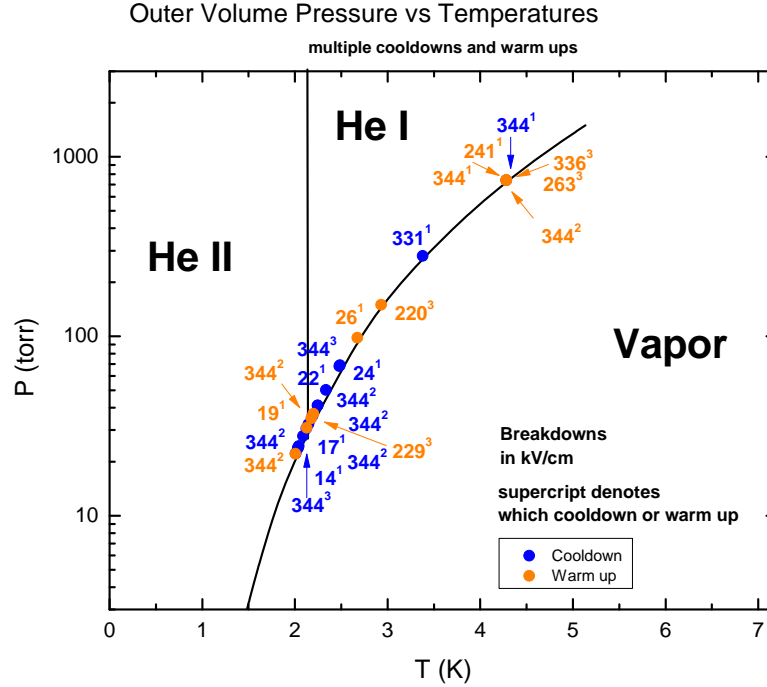


**Figure 4.42:** Breakdown in LHe when traversing SVP and crossing the  $\lambda$  transition multiple times.

categorized by the advancing contact angle, receding angle and equilibrium angle. Departure from perfect crystallographic planes, in the form of terraces and dislocations, leads to a random energy potential landscape and can cause pinning of the liquid film contact line. Wetting hysteresis is most widely studied on alkali substrates where the effect is most pronounced, in particular on cesium [77–79].

#### 4.9.5 Paschen trends in liquid helium

The Paschen curve gives the dependence of voltage on the product of pressure and gap size for electrical breakdown in gases. For helium gas the curve closely reflects

experimental data. In [80] the author gives a useful description of the Townsend regime and derivation of the Paschen curve. The breakdown voltage for a gas is given by

$$V_B = \frac{Bpd}{\ln(Apd) - \ln(\ln(1 + 1/\gamma))} \quad (4.44)$$

where A and B are experimental constants (related to the first Townsend coefficient),  $\gamma$  is the second Townsend coefficient and pd is the product of pressure and gap size. The first Townsend coefficient is expected to have the form

$$\alpha = \frac{C}{\lambda_e} \exp\left(-\frac{E_i}{E\lambda_e}\right) = Ap \exp\left(-\frac{Bpd}{V}\right) \quad (4.45)$$

where C is a constant,  $\lambda_e$  is the mean free electron path,  $E_i$  is the ionization energy of the gas and E and V are the electric field and voltage. Thus the first Townsend coefficient is related to the ability of field emitted electrons to ionize the gas. The second Townsend coefficient,  $\gamma$ , describes the efficiency of ionized gas particles to produce electrons upon colliding with the cathode, this process is also referred to as secondary emission. The constants A and B are expected to be constant over a certain range of pressure for a given gas,  $\gamma$  is a function of the gas and the electrode material.

The experimental values of A and B for He gas are given in [48] for the  $E/p$  range 20-150 V/cm torr. They are  $A = 3 \text{ (cm torr)}^{-1}$  and  $B = 34 \text{ V (cm torr)}^{-1}$ . While Paschen constants were generally well-known for He gas no such comparative study seemed to exist for liquid. The conspicuous absence of such a correlation with liquid became apparent by accident. After switching to a finer polishing scheme for electrodes and navigating the pressurization cycle it was found that the breakdown strength could recover spontaneously at low SVP. Figure 4.43 shows an early measurement of this type. The breakdown strength increases spontaneously at a low pressure during the cooling stage. Critically, this rise in breakdown strength occurs slightly above the  $\lambda$ -transition, around 50-60 Torr. An increase of breakdown strength below

the  $\lambda$ -transition has been observed before but no one appears to have reported an increase inside He-I.

The interesting shape of the low SVP breakdown recovery becomes apparent when breakdown voltage is plotted against  $pd$ . Indeed, the data are very reminiscent of the Paschen curve. The spontaneous recovery was more frequent when working with smoother finish electrodes and smaller gap sizes. In some cases, the recovery occurred close to 100 Torr and in all cases at  $pd$  values in the range 4-8 Torr-cm. Although the breakdown recovery in gas happens at slightly lower  $pd$  it seems plausible that the mechanisms are related. Indeed it would not be surprising to find that since formation of vapor is necessary for breakdown in liquid then mechanisms describing breakdown in gas could well apply to breakdown in a liquid.

Figure 4.44 shows an early attempt at establishing the Paschen constants for liquid helium breakdown. The relatively stochastic breakdown in liquid meant that more accurate fitting was obtained only for portions of the breakdown curve. The fitting parameters were the Townsend coefficients  $A$ ,  $B$  and the secondary ionization coefficient  $\gamma$  (which is included in the variable  $k$ ).

In addition to fitting portions of the  $pd$ -spectrum, attempts were made at fitting the first and second order Taylor expansions of the Paschen formula to portions of liquid breakdown data. There was typically good agreement in the region of linear  $pd$  dependence as seen in Figure 4.45. While the high  $pd$  behavior for various electrode surface finishes and gap sizes were similar, the low  $pd$  behavior was less consistent. That the pressure dependence in liquid at least for most of the  $pd$  spectrum resembled the Paschen law for gas appeared intriguing.

The increase in breakdown strength at low  $pd$  in liquid sometimes occurred close to  $P_\lambda d$ , i.e. the pressure at the  $\lambda$ -transition, and sometimes it occurred a factor of 2 or 3 above  $P_\lambda$ . It was useful then to perform measurements where  $(pd)_{min}$  was not near  $P_\lambda d$  so that any influence of the  $\lambda$ -transition could be discounted. The

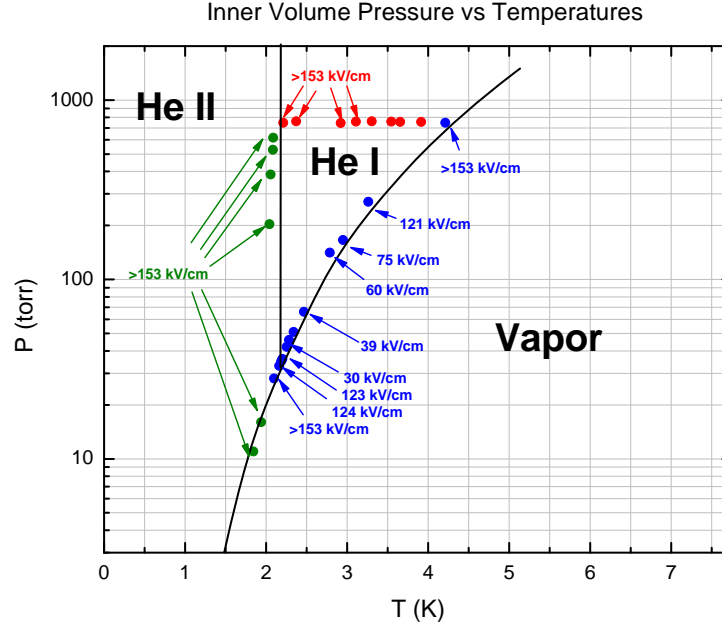


**Figure 4.43:** *Pressurization cycle with finer polishing of electrodes.*  
*Note the sudden large increase in breakdown strength at SVP.*

somewhat unpredictable nature of this low  $pd$  recovery meant that it was not easy to anticipate the position of  $(pd)_{min}$ . It is compelling to think that this unpredictable nature may be related to various  $d_i$ , as mentioned earlier, inside bubbles of various sizes. A larger abundance of bubbles, as could happen on rougher electrode surfaces, could mean a larger distribution of  $d_i$  and hence produce a more broad Paschen minimum or even no recovery at all. The comparatively rougher electrodes could well have a larger set of  $d_i$  and not observing a Paschen-type recovery could merely be a consequence. If the minimum were broad enough then a recovery would not be observable in liquid because there is a practical limit on the vapor pressure imposed by the rate of pumping (the minimum pressure that can be achieved with this system

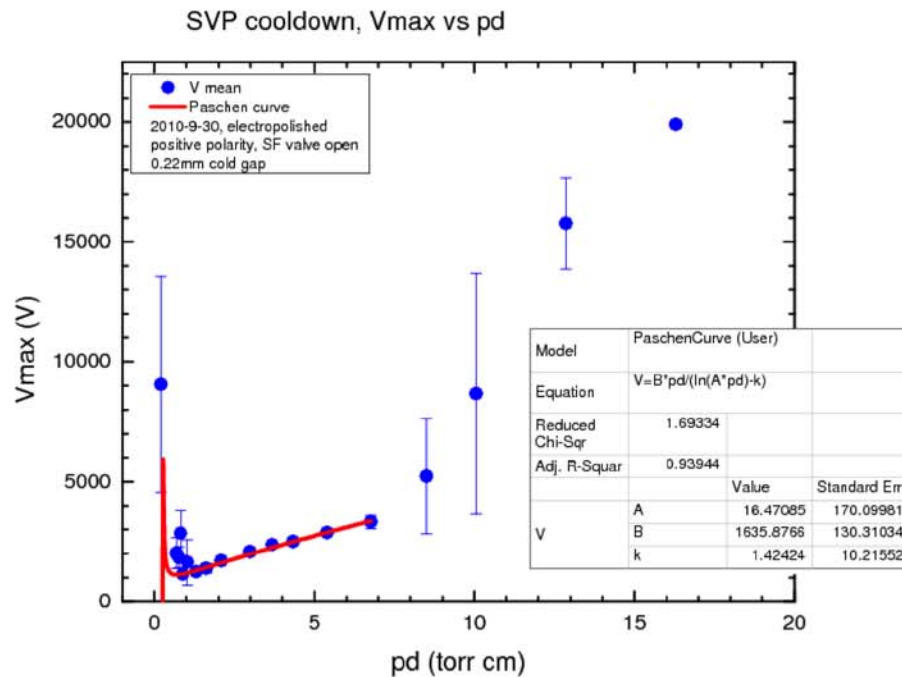


**Figure 4.44:** *Early fit of SVP liquid breakdown data to Paschen curve.*

is around 8 torr, pumping for longer than that would mean insufficient liquid to cover the electrodes). On the other hand, more finely polished electrodes could have a smaller distribution of bubbles (viz. smaller set of  $d_i$ ) and hence a more defined Paschen minimum and observable recovery. This concept for liquid breakdown is difficult to quantify and is supported, albeit vaguely, by quasi-successful fitting of modified Paschen curves to liquid breakdown data. The derivation of the Townsend model suggests that there should be some temperature dependence of the Townsend coefficients. While the Townsend model itself has a number of assumptions built in, it is unclear what kind of temperature dependence the coefficients should have.

Figure 4.46 shows breakdown results from 4 K helium gas with scaled version of



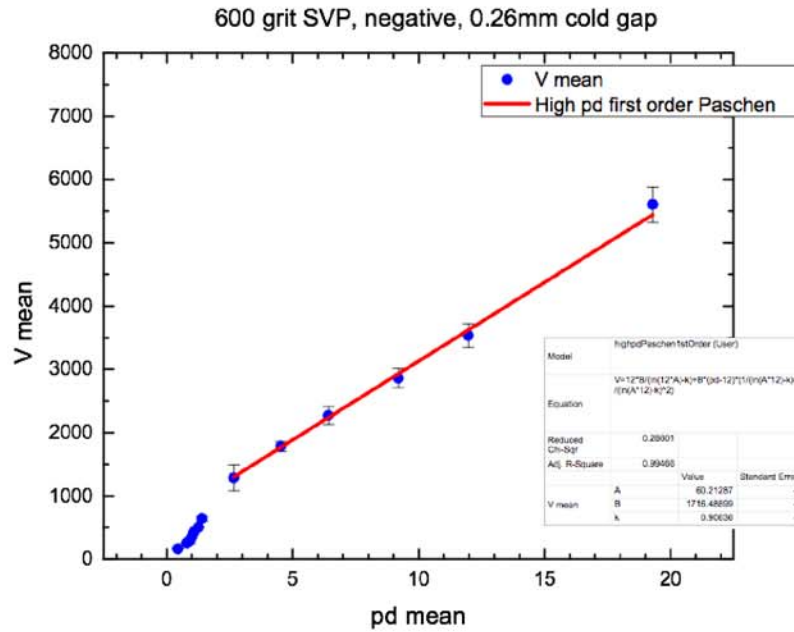


**Figure 4.45:** *First order Paschen expansion fitted to high pd liquid breakdown.*

breakdown compared with the Paschen curve. When the liquid breakdown voltages and  $pd$  values are reduced then there is a close correspondence to the usual helium Paschen curve. The apparent improved correspondence between the two curves suggests a link closer than previously thought between breakdown in LHe and helium gas. Modification of the Paschen coefficients can perhaps be due to the different temperature scale and vapor density or some other effect. The low  $pd$  recovery in LHe makes more sense if there exists a modified Paschen curve for LHe.

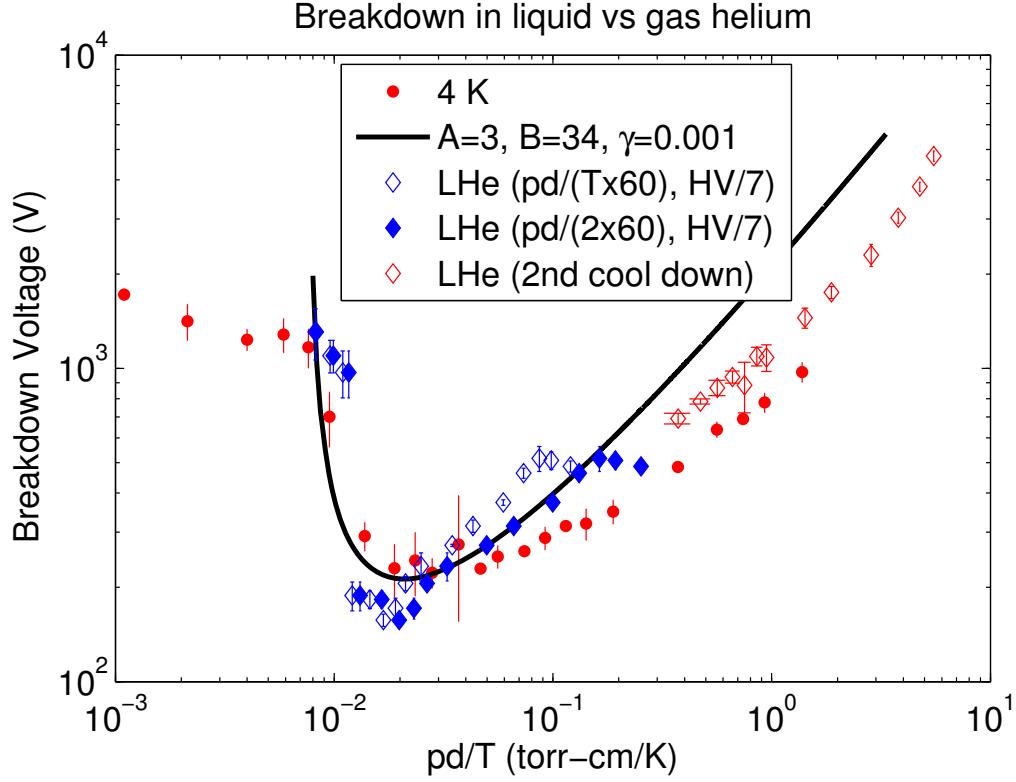


**Figure 4.46:** *Breakdown measurements in cold helium gas and scaled liquid helium compared with the Paschen curve.*

## 4.10 Discussion

In the previous section it was shown that there appears to exist a correlation between breakdown in LHe and He gas insofar as LHe breakdown, under certain conditions of surface roughness, appears to follow a Paschen-like trend. This is possibly due to the vaporization of liquid and breakdown taking place only after the electrode gap is bridged by vapor. Gerhold and Hubmann showed [81,82] that the helium Paschen curve is not affected by temperature by comparing the curves (scaled by density

number) at 293 K and 77 K, Fig. 4.47. Measurements of the gas Paschen curve at temperatures approaching liquid are scarce perhaps, as suggested by our studies near 4-5 K, because of the possible presence of liquid nucleation sites [83]. The high  $pd$ , right of the minimum, behavior is still consistent with the usual Paschen behavior but at low  $pd$ , left of the minimum, breakdown recovery tended to be less than for warmer Paschen curves.

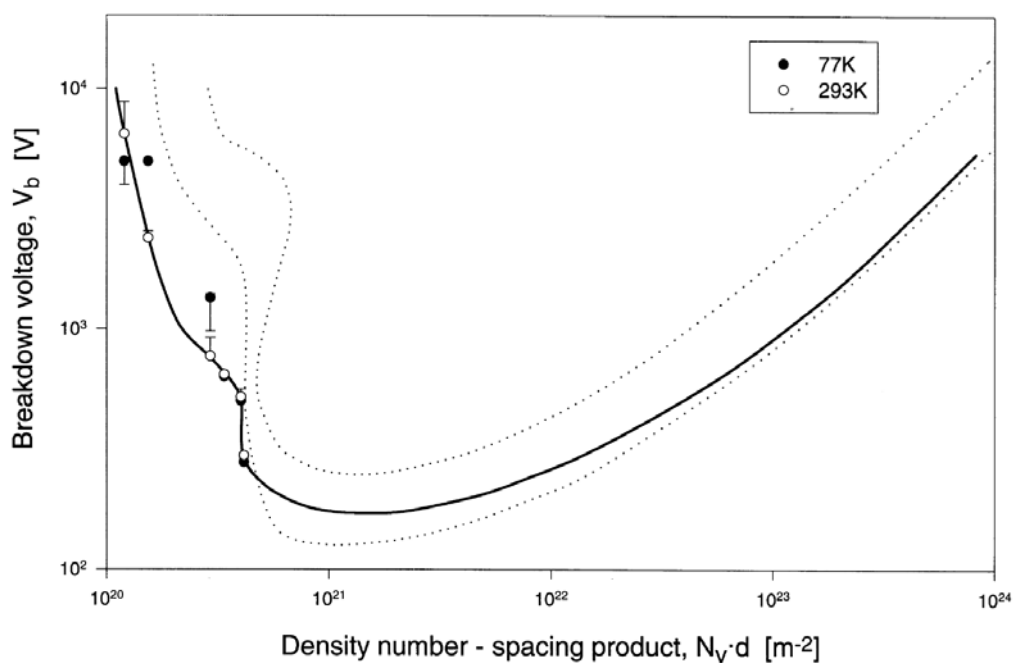


**Figure 4.47:** *Comparison of helium Paschen curves at room temperature and 77 K, from [82]*

A number of studies of breakdown in liquids in the presence of vapor exist. Perhaps the most thorough experiments in cryogenics were made by Masanori Hara and colleagues in Japan [70, 72, 74, 84–86].

Hong and colleagues [69] demonstrated the effect of vapor bubbles generated by a

heater on breakdown in liquid nitrogen. Figure 4.48 shows photos of vapor bubbles in an electric field in liquid nitrogen. Electrostatic forces caused the bubbles to elongate in the direction of the field until eventually the electrode gap is bridged by vapor. The vapor bridge tended to be mechanically stable and long lasting (several tens of minutes) if breakdown did not occur. The authors observed that in the presence of the electric field vapor bubbles remained in contact with the electrode surface (where the heater was mounted) for longer lengths of time. Since the electrodes were mounted vertically then vapor bubbles tended to drift up due to gravity.

Hong and colleagues also compared their results of liquid nitrogen breakdown with Paschen data for nitrogen gas. Their comparison was limited to pressures above atmospheric due to the phase diagram of nitrogen. Figure 4.49 shows their comparison of ac breakdown in liquid nitrogen with different heater powers and Paschen data.

The presence of vapor domains inside liquid with an applied electric has a large impact on the dielectric strength of the liquid. What is not so obvious is the origin of vapor domains. The concept of incomplete wetting of the electrode surface and heterogeneous nucleation have been conspicuously absent from literature as vapor domain sources in liquid dielectrics.

Heterogeneous nucleation sites can appear when there exists incomplete wetting by the liquid. If, for example, the container of the liquid contains micron-sized cavities or irregularities then these regions may trap vapor when the liquid is added. It will be seen that such regions of vapor can be very stable. It is only under very strict experimental conditions that homogeneous nucleation can be studied. It has been shown [87] that homogeneous nucleation of ice in water takes place at about  $-40^{\circ}$  C, but since there are almost always heterogeneous nucleation sites present water tends to freeze at  $0^{\circ}$  C at standard pressure. Heterogeneous nucleation plays a vital role in phase transitions (e.g., boiling, solidification) and phase transitions begin preferentially at heterogeneous nucleation sites. It is very unlikely for homogeneous

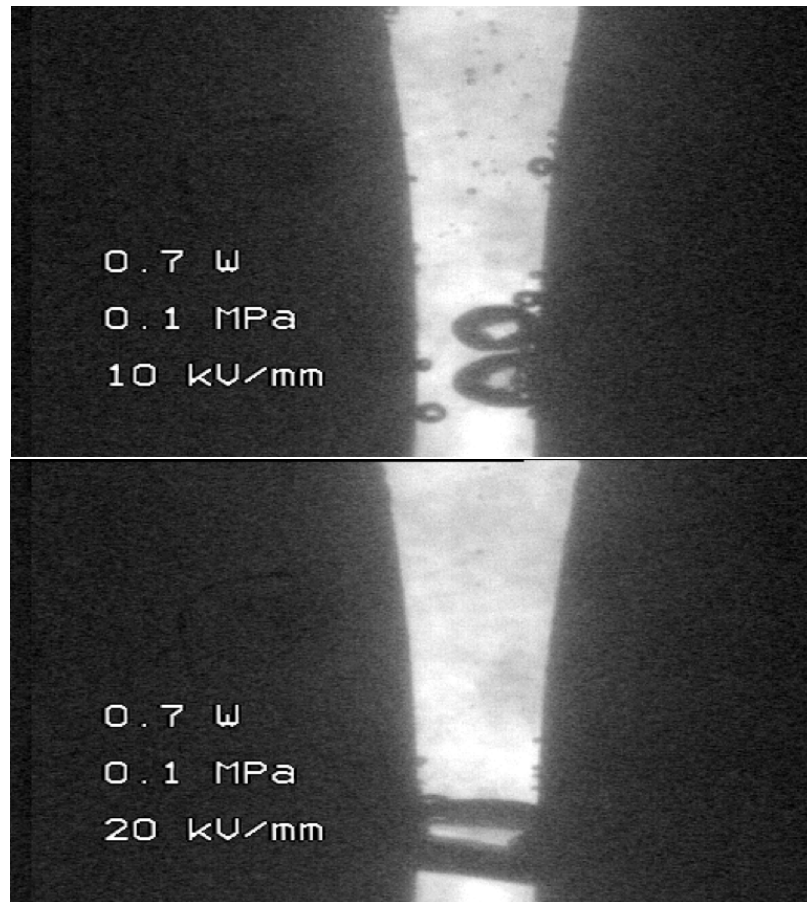


**Figure 4.48:** *Vapor bubbles between electrodes in liquid nitrogen, from [69]*

nucleation to be of much importance when dealing with electrode surfaces and LHe as a dielectric.

While it is known that the presence of vapor bubbles leads to premature breakdown in LHe and explains enhancements due to pressurization, the source of bubbles is usually taken to be thermal due to heat leaks or electrical due to local field enhancements at sharp points on the electrode surfaces [?] [?]. These interpretations, however, do not account for the apparent hysteresis we have observed. Few authors

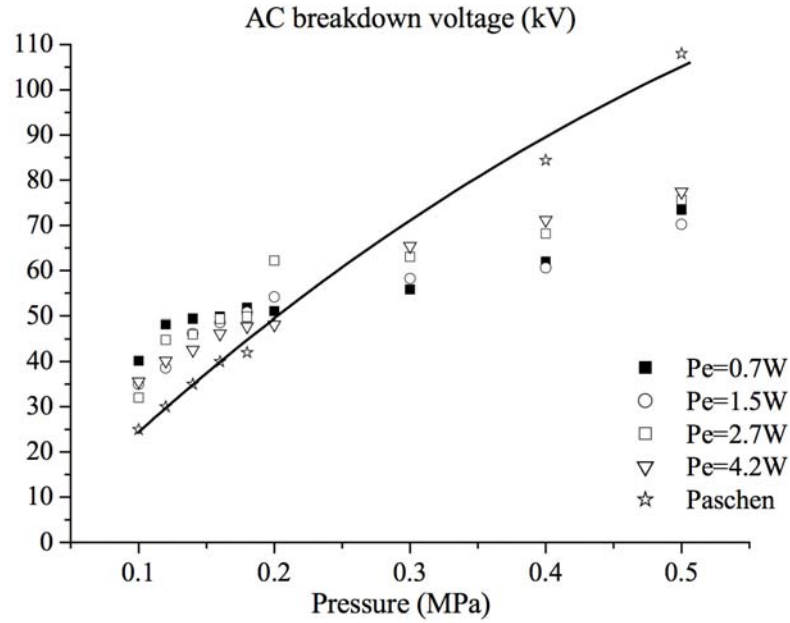


**Figure 4.49:** *AC breakdown in liquid nitrogen in the presence of vapor bubbles compared with nitrogen Paschen data , from [69]*

seem to consider incomplete wetting of the electrode surfaces as a source of vapor pockets which could greatly affect breakdown. It is more likely that in our studies the dominant effect was incomplete wetting resulting in nucleation sites on the electrodes.

Foreign particles can also act as sites for condensation of vapor. When the pressure and temperature of a vapor lie on the saturation curve then condensation will begin at so-called nuclei of condensation [88], e.g., specks of dust. In this case the direction from which the saturation curve is approached does not matter since the condition of, say, ionized particles or dust specks are not necessarily dependent on pressure or temperature. Furthermore, in the absence of any foreign particles a vapor exhibits a resistance to condensation under conditions in which it otherwise would develop a

liquid phase [88].

Cooling along the saturation curve by pumping causes the hydrostatic pressure of the bulk liquid to decrease. If any bubbles are present in the system, this reduction in pressure will cause their volume to increase. Thus when the pressure decreases monotonically the barrier against breakdown will become smaller and the breakdown field is expected to decrease. Why the breakdown field continues to decrease in the case of hand polished electrodes after the  $\lambda$  transition in our system is not fully clear though it may be related to a broader Paschen minimum that is the result of multiple breakdown gaps. In LHe, multiple breakdown gaps could arise from a large distribution of vapor bubbles on the ground electrode (as may happen on a rougher surface).

While not entirely clear how small gas bubbles can persist inside liquids, some explanations have been postulated by a number of sources. Batchelor [89] explains that gas pressure alone is not enough to balance the inward forces due to the liquid and prevent the bubble from dissolving. Stability of bubbles can be greatly improved inside micron-sized surface crevices, in this case located on the electrodes or on impurities such as dust. Inside such crevices the meniscus can be concave outward, balancing inward forces, in contrast to bubbles in the bulk liquid and on smooth surfaces, as shown in Figure 4.11.

Bubbles inside micro-crevices will have modified surface energy terms compared with bubbles on flat surfaces or ones moving through the bulk liquid. The three cases have different levels of stability, with the most stable being gas pockets trapped inside crevices (Figure 4.11 above). In this case, the surface force is not directed toward the inside of the bubble but rather the surface will become concave out and the surface force will be outward. Hence such a configuration will be much more stable against collapse compared with semi-hemispherical bubbles on flat surfaces and bubbles completely surrounded by liquid. It is entirely possible that such microcrevices can go

unnoticed on electrode surfaces but they can trap He vapor and lead to premature breakdown.

Degassing of water is a straightforward process. If water is pressurized to many atmospheres and depressurized to 1 atm, then boiling will be suppressed until well above 100° C [89]. Though degassing typically refers to the removal of dissolved gases, the dynamics involved in wetting are similar.



## Chapter 5

# Liquid Helium Ionization Detection

### 5.1 nEDM Cell as Ionization Chamber

It is worthwhile to explore the possibility of using the *in situ* electric field to measure the generated charges in the neutron absorption reaction in the nEDM experiment. The  ${}^3\text{He}(\text{n,p}){}^3\text{H}$  reaction in the nEDM experiment has a Q-value of 764 keV shared between the resulting triton and proton. The energy goes into ionization of the LHe medium (production of electron-ion pairs) and creating excited atomic states. When the electron-ion pairs recombine they produce excited Helium molecules known as excimers in the triplet and singlet states which decay radiatively. This decay produces a 16 eV photon in the extreme ultraviolet (EUV). The EUV photons must then be converted into ultraviolet before they can be detected with photomultipliers.

The presence of a strong electric field, however, means that a portion of the electron-ion pairs will not recombine and will instead drift toward the electrodes. It should be possible to measure the charges at the ground electrodes and in this sense treat the nEDM cell as a liquid ionization chamber.

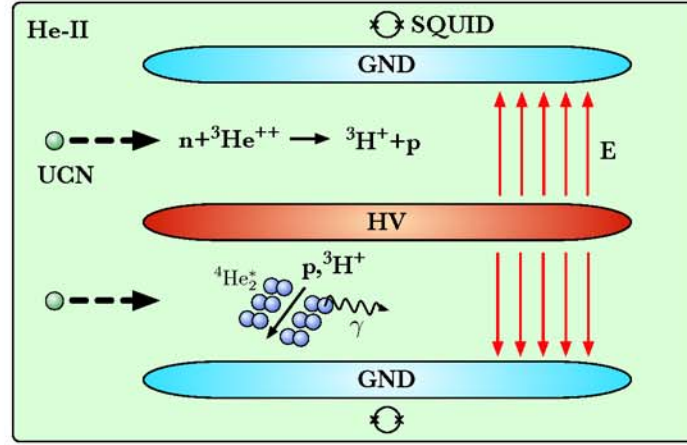


**Figure 5.1:** *Schematic of the nEDM detection cell, adapted from [90].*

### 5.1.1 Charged particle interactions with matter

The operating principle behind most detectors is the energy loss of the radiating particle. The energy of the particle is converted to more easily measurable phenomena such as light, heat and electric charge. In an ionization chamber the radiating particle loses its kinetic energy by scattering inelastically with a gas and this scattering, for sufficient energies of the incoming particle, will excite and ionize the gas atoms. Atomic collisions can be *soft*, where the atom is merely excited, and *hard*, where the collision ionizes the atom. For sufficiently large energy transfers liberated electrons, known as  $\delta$ -rays, can create additional ionizations. An applied electric field displaces the charges toward the electrodes and this produces a measurable voltage or current. Detailed descriptions of ionization chambers and particle detection can be found in standard texts such as [91–94], a few key points are summarized below.

### 5.1.2 Energy loss in matter

#### I Classical picture

For an atomic electron a distance  $b$  from the path of an incoming particle of charge  $ze$ , mass  $M$  and velocity  $v$  we can compute the energy transfer. The impulse transferred to the electron by the particle [94, 95] is given by

$$I = \int_{-\infty}^{\infty} F(t)dt = e \int_{-\infty}^{\infty} E_{\perp}(t)dt \quad (5.1)$$

where only the normal component contributes since the longitudinal averages to zero.

Using

$$\int E_{\perp}(t)dt = \int E_{\perp}(x) \frac{dt}{dx} dx = \frac{1}{v} \int E_{\perp}(x)dx \quad (5.2)$$

then

$$I_{\perp} = \frac{e}{v} \int_{-\infty}^{\infty} E_{\perp}(x)dx \quad (5.3)$$

and it follows from Gauss' law that

$$4\pi ze = \oint \mathbf{E} \cdot d\mathbf{S} = \int_{-\infty}^{\infty} 2\pi b E_{\perp} dx . \quad (5.4)$$

Therefore the impulse delivered to the electron is

$$I_{\perp} = \frac{2ze^2}{vb} \quad (5.5)$$

and, assuming the electron was originally at rest, the energy transferred becomes

$$E(b) = \frac{I_{\perp}^2}{2m} = \frac{2z^2e^4}{mv^2b^2} . \quad (5.6)$$

Atomic electrons are responsible for most of the energy loss.

#### II Quantum picture

The quantum picture of energy loss is attributed to H. Bethe with later corrections by F. Bloch. The more accurate treatment requires the sum of all excitation energies

weighted by their respective cross sections

$$\left. \frac{dE}{dx} \right|_{w < \eta} = n_a \sum_n \int E_n d\sigma \quad (5.7)$$

where  $n$  is some limiting energy transfer. This holds when the interaction is distant and the incoming particle interacts with the atom as a whole. When the interaction is close it can be considered to take place with the electrons and the energy loss can be written

$$\left. \frac{dE}{dx} \right|_{W > \eta} = n_e \int_{\eta}^{W_{\max}} W \frac{d\sigma}{dW}(E, W) dW \quad (5.8)$$

where  $\frac{d\sigma}{dW}(E, W)$  is the cross section for an incident particle with energy  $E$  to lose energy  $W$  on collision with an electron [95]. Spin will only play an important role when  $W \sim E$ . Close and distant contributions must be combined to obtain the total energy loss, for spin 0 incident particles this gives

$$\frac{dE}{dx} = \frac{4\pi n_e Z_1^2 e^4}{mv_1^2} \left( \ln \frac{2mv^2 \gamma^2}{I} - \beta^2 \right) \quad (5.9)$$

where  $I$  is the ionization energy,  $\beta = v/c$ .

## 5.2 Ions and electrons in liquid Helium

Several mechanisms require investigation to determine whether the nEDM cell can potentially operate as an ionization chamber for the  ${}^3\text{He}(\text{n,p}){}^3\text{H}$  reaction. As will be seen, the behavior of Helium ions and electrons in LHe, and He-II in particular, warrants special attention. The description of the behavior and transport of charges in LHe follows several standard references [96] and references therein. It is conventional to distinguish between the positive ions and negative electrons: ions will refer only to ionized Helium atoms. The broader term ‘charges’ will be used to mean both ions and electrons, or only one species when it does not matter which species in the context.

Historically, the study of the drift of charges in liquid Helium has been a useful probe of quantum-hydrodynamics in He-I and He-II, the breakdown of superfluidity and scattering from elementary excitations. Charges can be introduced into LHe by various means, such as field emission, thermionic emission or ionization. They are then accelerated with the use of electric fields and can be measured with appropriate circuitry at the electrodes. Ionized Helium atoms form  $(^4\text{He})_2^+$  in LHe. Positive ions produce strong electric fields in their immediate vicinity and by electrostriction are surrounded by an enhanced density of the fluid. The pressure around the positive ion can exceed the melting pressure of 2.5 MPa and thus the positive ion is surrounded by small amount of solid Helium. This is the reason positive ions are usually called ‘snowballs’. The snowballs are approximately 12 Å in diameter and have an effective mass between forty and sixty times the  $^4\text{He}$  atom between 0 K and 4.2 K.

The free electron in LHe is unstable due to the repulsive exchange force in the electron-He interaction. Electrons in LHe thermalize rapidly by becoming self-trapped in an empty cavity (by expelling nearby He atoms). The repulsive force an electron experiences in LHe is approximately 1 eV and it is energetically favorable for the electron to become self-trapped. The energy can be well-approximated as

$$E = \frac{h^2}{8mR^2} + 4\pi R^2\alpha + 4/3\pi R^3P \quad (5.10)$$

where  $m$  is the electron mass,  $R$  the bubble radius,  $\alpha$  the surface energy per unit area and  $P$  the applied pressure. At zero pressure and temperature [97],

$$R_{min} = \left( \frac{h^2}{32\pi m\alpha} \right)^{1/4} = 19 \text{ Å}. \quad (5.11)$$

Experimental values for the radius of the electron bubble vary between 18 Å at zero pressure and 11 Å at 2.5 MPa and between 15 Å at 1 K and 20 Å at 4 K, [96] and references therein.

For low temperatures where LHe is dominated by the He-II fraction, charges drifting sufficiently slow through LHe should not experience any resistance. For higher temperatures however, charges will collide with thermal excitations in the fluid and charge mobility depends primarily on the presence of thermal excitations.

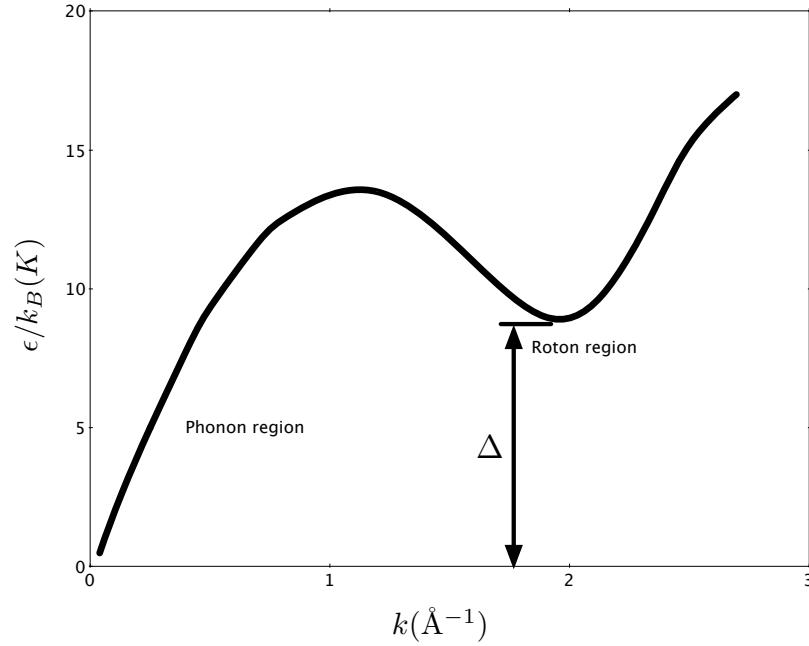


**Figure 5.2:** *Elementary excitation spectrum in He-II at SVP and  $T = 1.12$  K obtained with neutron scattering experiments.*

The energy excitation spectrum for He-II, first proposed by Landau [98] is shown in Fig. 5.2. For low temperatures longitudinal phonons are the dominant excitation but for  $T > 1$  K the roton density is dominant. These excitations are often termed quasi-particle excitations since charges can be scattered by them. Phonons can be characterized by a velocity  $c$  and the energy written as

$$\epsilon = cp \tag{5.12}$$

where  $p = \hbar k$  is the phonon momentum and  $k$  is the wave number. The second type of excitation, the roton, is unique to superfluid. Roton energy is given by

$$\epsilon = \Delta + \frac{(p - p_0)^2}{2\mu} . \quad (5.13)$$

The energy gap  $\Delta/k_B = 8.65$  K, roton mass parameter  $\mu = 0.16m_{\text{He}}$  and  $p_0/\hbar = 19.1 \text{ nm}^{-1}$  were obtained with neutron scattering experiments [99]. For low electric fields the drift velocity of charges is proportional to the electric field  $E$ , the mobility  $\mu(T) = v_d/E$  is mostly constant at different temperatures and is proportional to the inverse roton density [100]

$$\mu^{-1} \propto \exp\left(-\frac{\Delta}{k_B T}\right). \quad (5.14)$$

Experiments with drift velocities of charges in LHe revealed several surprising results, particularly in He-II. Careri and colleagues found a sharp discontinuity in the drift velocity associated with the creation of vortex rings [101]. Figure 5.3 shows measurements of drift velocities for electrons and positive ions plotted against the reduced electric field  $E(\rho/\rho_r)$ , where  $\rho_r$  is the roton contribution to the normal fluid density. At high electric fields, particles moving above the critical velocity,  $\sim 58$  m/s, have enough energy to emit rotons [100]. Roton creation was found to be the process responsible for the limit of drift velocity [102] at high fields where  $v_d \rightarrow v_L$  where  $v_L$  is the Landau velocity. This limit can only be reached at high pressure where the formation of vortex rings is suppressed. At SVP the creation of vortex rings is the limiting process for the drift velocity. Interestingly, at low fields alkali earth ions have much higher mobilities than  $^4\text{He}$  ions [103].

Figure 5.4 shows what the emission of a vortex ring may look like for an electron traveling faster than the critical velocity [104].

Schwarz and Stark [105] measured the electron bubble mobility in He-II for  $T \leq 0.5$  K and found that phonon scattering was the dominant effect. Electrons were injected

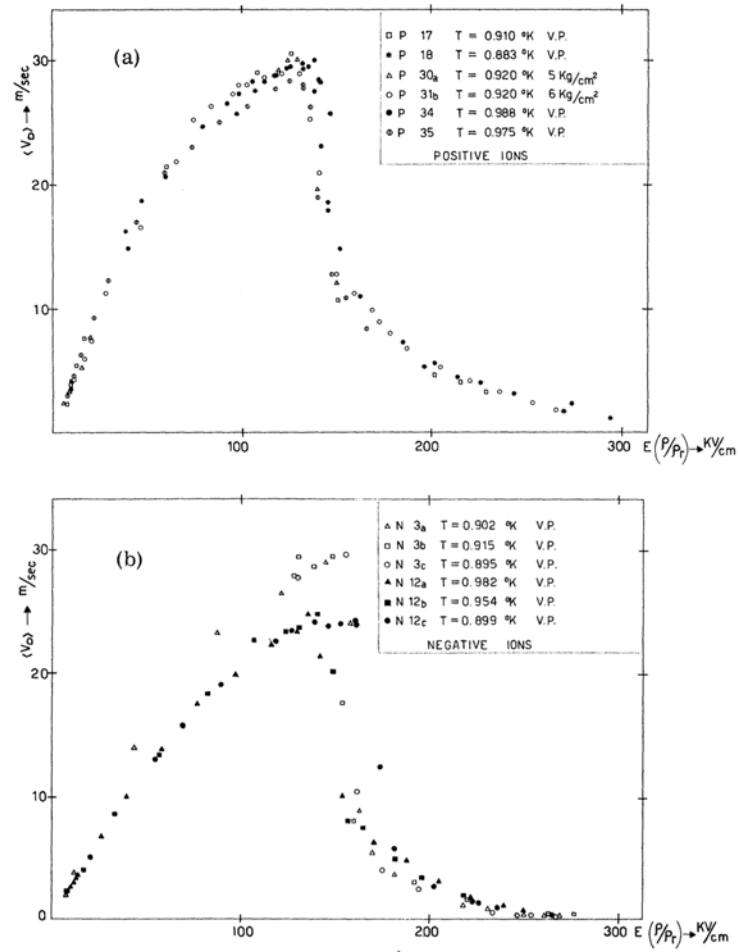


**Figure 5.3:** *Drift velocities of positive ions and electrons against the reduced electric field, from [101]*

into He-II using a <sup>241</sup>Am source and using a series of guard rings they measured the direct time of flight.





**Figure 5.4:** *Simulated density plot of vortex ring emission from an electron moving above the critical velocity, from [104]*

### 5.3 Design

Cooling of low temperature experiments can be divided into three stages. In order to reach higher stages of cooling the lower stages need to be utilized. In the first stage cooling is provided by a cryogen such as liquid  $^4\text{He}$  and limited to evaporative cooling (this type of cooling was described in the previous chapter). In the case of LHe this places a practical limit at around 1.6 K (depending on the pumping power available and heat load). The second stage of cooling can be reached using a  $^3\text{He}$  cryostat or a  $^3\text{He}$ - $^4\text{He}$  mixture cryostat. Because of its higher vapor pressure compared with  $^4\text{He}$ , a  $^3\text{He}$  cryostat can reach temperatures around 0.3 K, however pure  $^3\text{He}$  systems are prohibitively expensive and systems based on mixtures of the two isotopes are much more common and practical. The third stage of cooling can be achieved using adiabatic demagnetization of electronic spin states in paramagnetic

salts and is capable of reaching temperatures below  $\mu\text{K}$ . This work utilized only the first two stages of cooling.

### 5.3.1 The dilution refrigerator

Cryostats based on  $^3\text{He}$ - $^4\text{He}$  mixtures are termed dilution refrigerators for reasons which will become apparent in this section.

The dilution refrigerator (DR) has been central in low temperature physics research for half a century. First proposed by Heinz London in 1951 ([39] and references therein) and successfully constructed in 1964, the basic operation revolves around the entropy of mixing between fermionic  $^3\text{He}$  and bosonic  $^4\text{He}$ . DRs have since become mainstream and commercial models (though very expensive) are readily available and with customized applications. Nice discussions of the dilution refrigerator can be found in [39] and [106].

Owing to the spin-zero nature of  $^4\text{He}$  and Bose-Einstein statistics it exhibits superfluidity at 2.17 K, while  $^3\text{He}$  is spin- $\frac{1}{2}$  and as a result of Fermi-Dirac statistics does not become superfluid until below 2.5 mK. Thus a solution of  $^3\text{He}$  in He-II flows with little impedance from  $^4\text{He}$  and the He-II behaves rather like an empty lattice. For practical purposes a low concentration of  $^3\text{He}$  in He-II can be treated as a weakly-interacting Fermi gas.

When stage 1 cooling has been reached in the DR, the Helium gases are liquefied and they begin circulating and providing additional cooling. Since  $^3\text{He}$  has the higher vapor pressure of the two it is liquefied and recirculated first, this provides ample cooling power to liquify the remaining  $^4\text{He}$ . As the mixture cools under recirculation, a spontaneous phase separation of the isotopes occurs below a temperature depending on the  $^3\text{He}$  concentration, Fig. 5.5. For typical  $^3\text{He}$  concentrations in DRs this phase separation occurs at around 0.3-0.4 K.

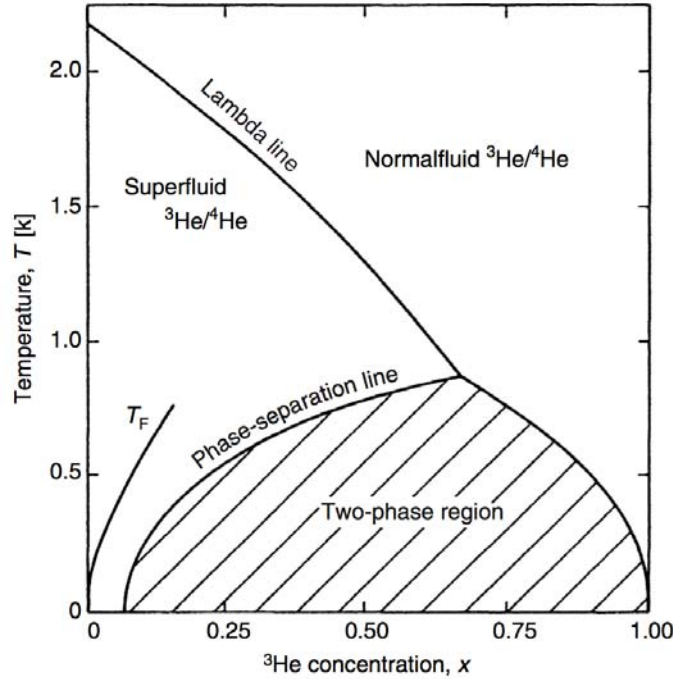


**Figure 5.5:** Phase diagram of the  $^3\text{He}$ - $^4\text{He}$  mixture. For typical  $^3\text{He}$  concentrations in dilution refrigerators phase separation takes place around 0.3-0.4 K. From [39]

In Fig. 5.5 is shown the phase diagram of a mixture of  $^3\text{He}$  and  $^4\text{He}$  for temperature and  $^3\text{He}$  concentration. Below a critical temperature of 0.87 K the mixture spontaneously separates into two phases: a  $^3\text{He}$ -rich phase which floats atop the heavier  $^4\text{He}$ -rich phase. The most significant feature is that the  $^4\text{He}$ -rich phase contains a finite concentration of  $^3\text{He}$  even approaching absolute zero (this does not violate the third law of thermodynamics because the two isotopes are quantum liquids). Instead the  $^3\text{He}$  concentration in the  $^4\text{He}$  approaches a constant value of 6.6%. The crucial aspect of the dilution refrigerator, therefore, is the forced ‘evaporation’ of  $^3\text{He}$  across the phase separation boundary from the  $^3\text{He}$ -rich phase into the dilute phase and the

apparently large amount of  $^3\text{He}$  in the dilute phase means a large flow rate is possible. The cooling comes from the enthalpy of mixing of the two isotopes [39]

$$\dot{Q} = \dot{n}_3 [H_d(T) - H_c(T)] \simeq 84\dot{n}_3 T^2 \quad (5.15)$$

where the subscripts  $d$ ,  $c$  refer to dilute and concentrated phases respectively,  $Q$  denotes the heat,  $n_3$  the number of  $^3\text{He}$  atoms and  $H$  the enthalpy. Precise expressions for thermodynamics quantities of  $^3\text{He}$  in the dilute or concentrated phases for any appreciable range of temperatures are not known. The above equation is an approximation given in [39].

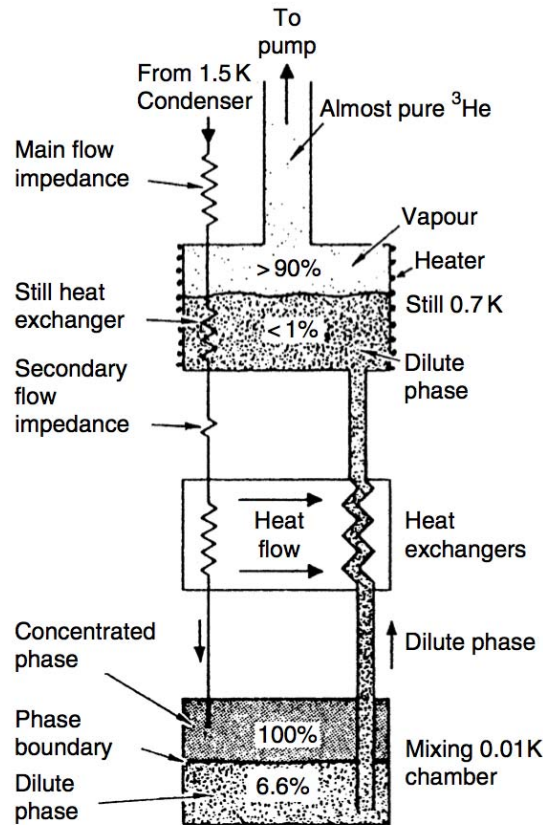


**Figure 5.6:** *The flow schematic of a dilution refrigerator. From [39]*

In Fig. 5.6 is the typical flow diagram for a dilution refrigerator. In the mixing chamber is shown the phase separation of the two isotopes. It is important that the outgoing line from the mixing chamber comes from the dilute mixture in order to create a deficit of  $^3\text{He}$  in the dilute phase and force it to cross the phase boundary to replenish the dilute phase. It is sometimes necessary to calibrate the amount of  $^3\text{He}$  in the mixture for proper positioning of the phase boundary.

For typical still temperatures around 0.7-0.8 K,  $^3\text{He}$  has a vapor pressure three

orders of magnitude higher than the vapor pressure of  $^4\text{He}$ . As a result almost pure  $^3\text{He}$  is evaporated and recirculated.

### 5.3.2 Operation of the CF650 Dilution Refrigerator

The DR used for this experiment was model CF650 manufactured by Leiden Cryogenics in the Netherlands. CF650 is used to denote cryogen-free with a cooling power of 650mW at 120mK. A description of its operation highlights well the principles behind the DR. The CF650 was commissioned at IU in late 2008.

The CF650 DR offers many features which are only gradually making their way into the commercial market. Most prominent is the cryogen-free operation. Traditionally DRs have relied on a ‘1K pot’, i.e., a reservoir of LHe which is pumped continuously and refilled from a storage dewar, to provide cooling for the recirculating, incoming gas. The CF650 instead uses a Cryomech Pulse-Tube (PT) compressor to provide the first stage of cooling and is capable of supplying 2W of cooling power at 3K. The mixing chamber plate, at about 12 inches in diameter, provides tremendous area for the setup of experimental apparatus. In addition, much of the second stage of cooling is automated inside the gas handling system (GHS).

The CF650 consists of an outer vacuum chamber (OVC, in blue in Fig 5.7) and an inner vacuum chamber (IVC). The inner vacuum chamber contains everything below the 3K plate: the still, intermediate plate between still and mixing chamber, then mixing chamber plate and any experiment attached to the mixing chamber plate. An intermediate heat shield is installed between the OVC and IVC on the 50K plate which is not vacuum tight.

The OVC contains two activated charcoal sorption pumps which allow the OVC pressure to reach high vacuum at low temperature. The IVC contains one sorption pump with a heater inside which allows for the emission and absorption of exchange



**Figure 5.7:** *The assembled CF650 dilution refrigerator with pulse-tube compressor and gas handling system.*

gas. The exchange is necessary to cool the interior components of the IVC since stage 1 cooling ends at the 3K plate. During stage 1 cooling some Helium exchange gas must be present in the IVC but not in the OVC.

Once base temperature for stage 1 is reached (around 2.5 K) then the exchange gas is removed from the IVC. This can be done by shutting off the heater to the IVC sorption pump or using turbomolecular pumps. When the IVC is at high vacuum then stage 2 cooling can begin.

### I Stage 2 cooling

Once the interior of the IVC is at about 2.5 K and the IVC is at high vacuum then condensation of  $^3\text{He}$  can begin ( $^3\text{He}$  is liquefied first because it is able to provide a high cooling power for the much larger amount of  $^4\text{He}$  that must be liquefied). The CF650 contains about 40 liters of  $^3\text{He}$ .  $^3\text{He}/^4\text{He}$  condensation is mostly automated by the GHS and it monitors pressures at the inlet and still to maintain optimum condensation flow. Condensation is aided by a gas compressor to increase the inlet pressure to 2-3 bar. The temperature of the mixing chamber decreases as soon as the first liquid is produced because the DR loop enters recirculation mode as a  $^3\text{He}$  cryostat. In about 30 minutes all of the  $^3\text{He}$  will be liquefied and will be circulating through the DR loop. The free liquid surface will likely be somewhere inside the mixing chamber and the temperature reaches about 0.5 K.

Once the  $^3\text{He}$  is liquefied then the process is repeated with  $^4\text{He}$ . The CF650 contains about 120 liters of  $^4\text{He}$  and it takes about 90 minutes to liquify. Once all the mixture is condensed then the GHS enters a ‘normal circulation’ mode and the gas compressor is no longer used. In this mode the gas is in a purely recirculating state. Some manual intervention is necessary, however, to optimize the position of the  $^3\text{He}/^4\text{He}$  phase boundary inside the mixing chamber. Due to a small surplus of  $^3\text{He}$  in the system some of it is removed until an optimal cooling rate is reached. This will be indicated by stability in the outlet and inlet pressures and a sudden monotonic decrease in temperature. The 100  $\Omega$  heater on the still is also adjusted to maintain an outlet pressure between 0.2-0.3 mbar as this provides an optimal recirculation rate and hence optimal cooling power for the CF650. During commissioning in 2008 the CF650 reached below 20 mK without much effort and without heat loads due to apparatus on the mixing chamber plate and instrumentation hookups. In single-shot mode, where recirculation is stopped and gas is routed into the storage tanks, the



CF650 reached near 10 mK.

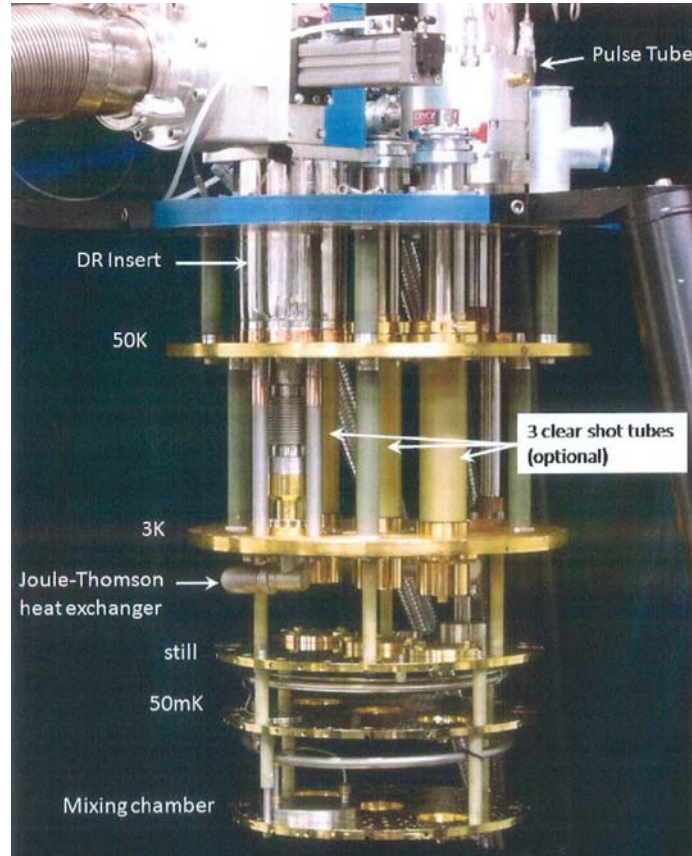


**Figure 5.8:** *Interior of the CF650 dilution refrigerator.*

### 5.3.3 Test chamber

Prototyping of the environment found in the nEDM cell precluded the use of guard rings and grids which would facilitate a measurement of charge drift. To that end, the geometry was limited to plane-parallel electrodes without any other conductors. If the purpose of the investigation were only to measure the drift and collection of charges then several crucial modifications would be necessary, but that would not

have made the result relevant to the nEDM effort.

The test chamber used in this experiment was inherited from a scintillation experiment conducted at IU in collaboration with Los Alamos National Laboratory [107]. Hence the design of the test chamber was with that experiment in mind and slight modifications had to be made to accommodate the experiment described here.

The test chamber is made from stainless steel with two conflat seals, one for the high voltage access and the second for the gas vent as seen on the left and right sides of Fig. 5.9.

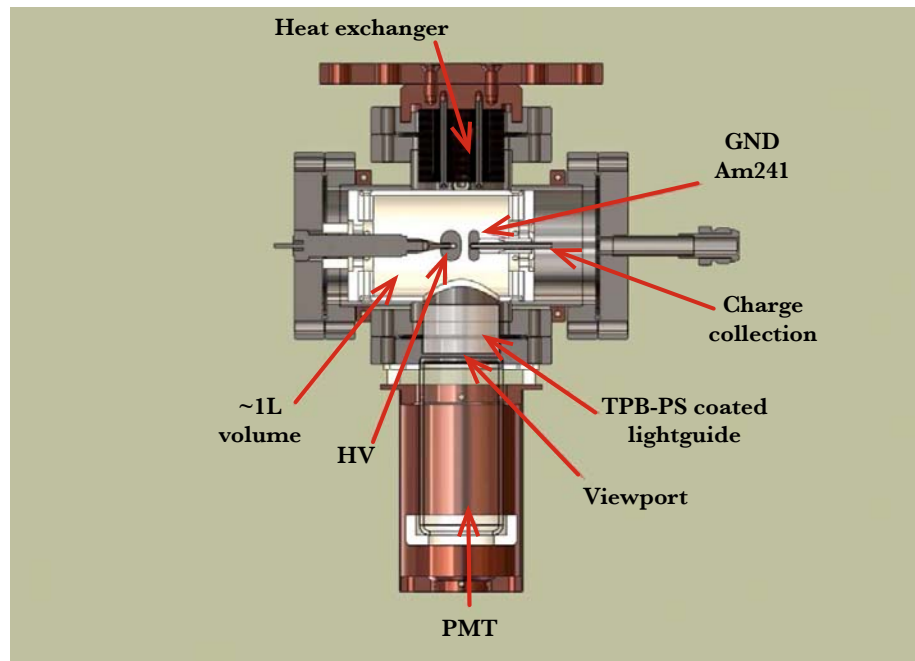


**Figure 5.9:** *Main interior features of the test chamber. The PMT, lightguide and viewport were removed for this experiment.*

A gold-coated copper heat exchanger is located at the top of test chamber which transfers heat to the mixing chamber plate.

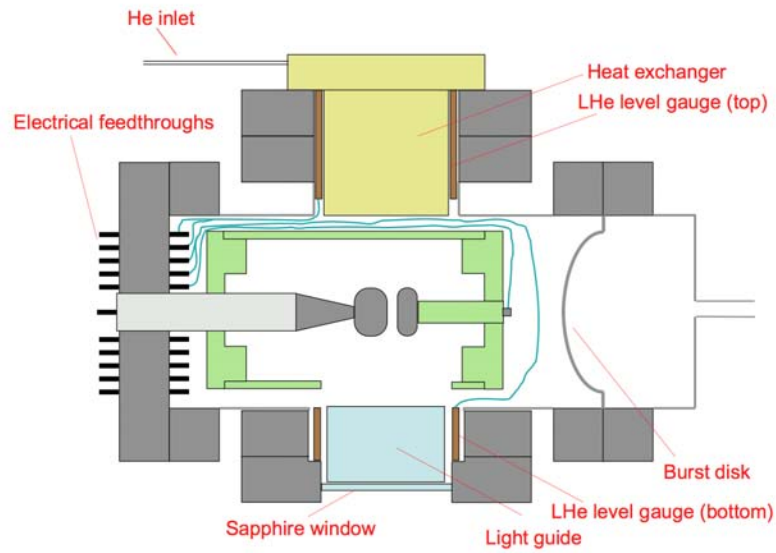


**Figure 5.10:** *Geometry of the interior of the test chamber. The sapphire window and lightguide were used for a different experiment.*

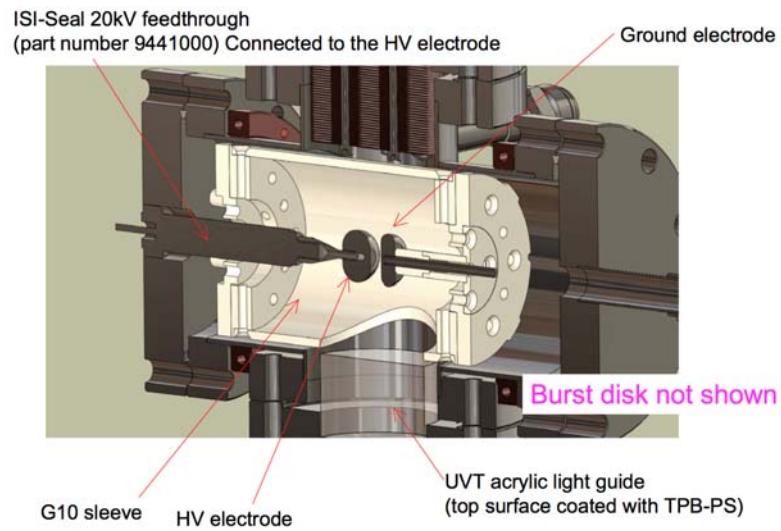


**Figure 5.11:** *Cutaway view of the test chamber showing the approximate available volume for liquid Helium.*

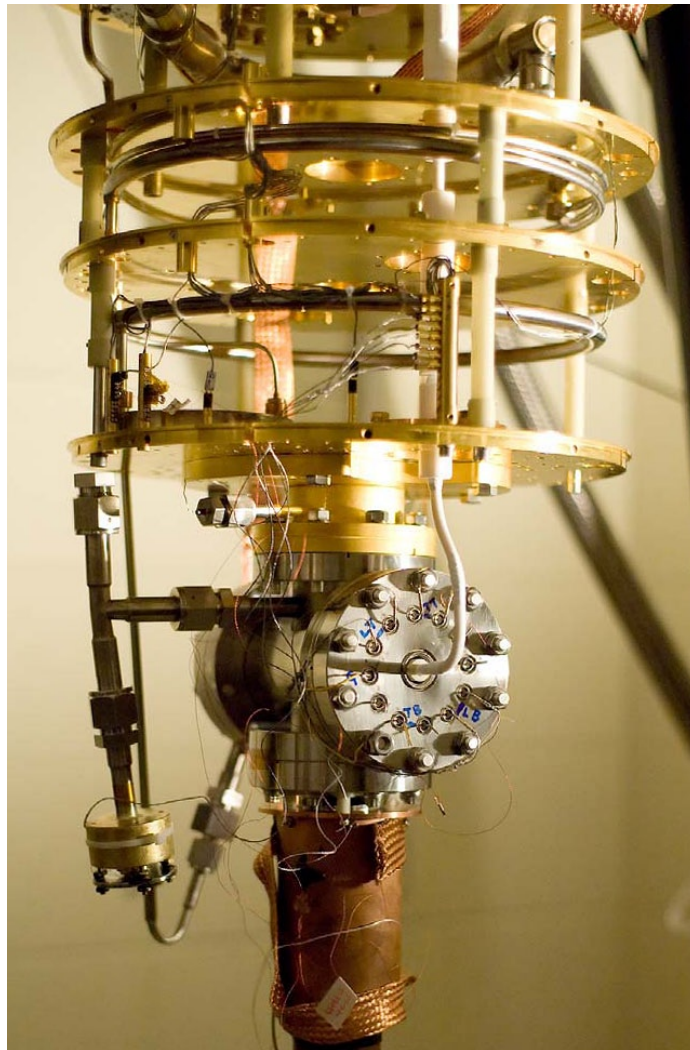


**Figure 5.12:** *Test chamber with PMT attached to the mixing chamber plate.*

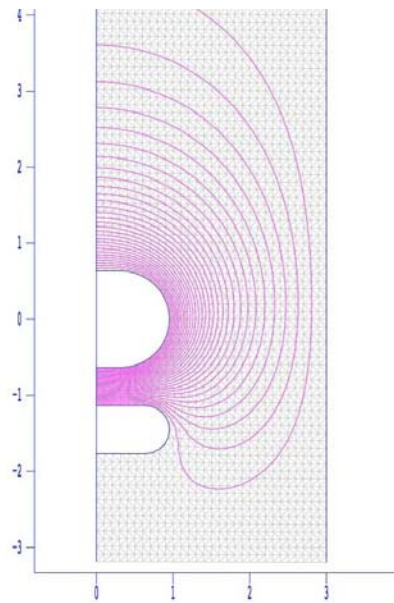


**Figure 5.13:** *Poisson Superfish electrode geometry field simulation done at LANL, units in cm.*

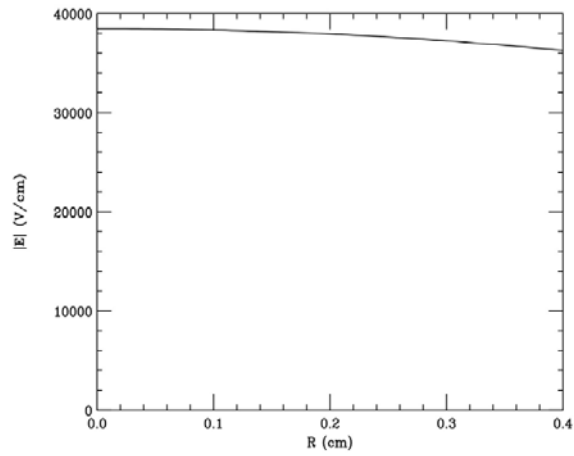


**Figure 5.14:** *Electric field uniformity profile calculation done at LANL shows low field falloff across the area of the electroplated  $^{241}\text{Am}$  source.*

### 5.3.4 Test chamber gas handling & liquefaction

The test chamber is filled with liquid Helium using a dedicated gas handling system with a clean Helium supply. Through several iterations an effective gas handling system was constructed (Fig. 5.15) capable of efficient liquefaction (even at sub-Kelvin temperatures) and recovery without wasting Helium gas. The system is also self-cleaning due to the presence of a liquid Nitrogen (LN) charcoal trap, each liquefaction-recovery cycle resulted in a cleaner gas supply, provided the LN trap was cleaned and baked between cycles. Arrows near the compressor indicate the direction of gas flow into the test chamber during operation.

#### Test Chamber Gas Handling System

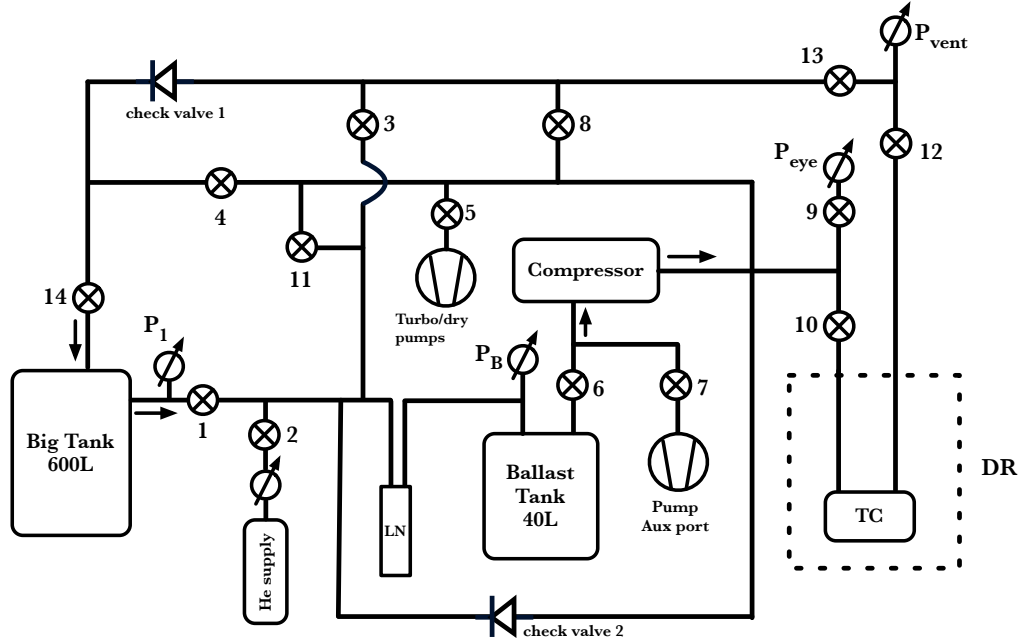


Figure 5.15: Test chamber closed gas handling system.

Gas is delivered to the test chamber using a 1.2 mm CuNi capillary which is thermally anchored at every stage inside the DR. A Joule-Thompson heat exchanger

on the 3 K plate allows gas inside the capillary to become liquefied at that stage, taking advantage of the ample cooling power of the pulse-tube refrigerator. A series of copper posts anchor the capillary to each of the subsequent plates before entering the test chamber from its top.

A vent line from the test chamber to a room temperature pressure gauge (Pvent in Fig. 5.15) provides an indication of the vapor pressure inside the test chamber. At low temperatures, where the vapor pressure of LHe is very low, the vent line provides a minimal heat load to the test chamber. Superfluid film creep is also not a serious concern as the system was able to sustain temperatures of 176 mK with the test chamber full of superfluid.

The vent line is a necessary addition to the test chamber and serves several functions in addition to indicating the vapor pressure of the liquid. It provides an emergency relief path for boil off in the event of loss of cooling. The wide diameter of the vent line (0.25") also provides an easier way of evacuating the test chamber as opposed to the thin capillary. It is also necessary for the test chamber to have an inlet and outlet so that clean Helium gas can be circulated for cleaning and a continuous gas circulation is also an effective way of preventing blockages from the accumulation of impurities in the capillary.

Procedures for using the test chamber gas handling system (GHS) have become standard during the time of the experiment. The first necessary step is the cleaning of the GHS, assuming connections were broken and air introduced into the GHS. This is done using two pumps depending on the pressure inside the GHS. A scroll pump is connected to valve 7 (see Fig. 5.15) and a dry pump with a turbomolecular pump is connected to valve 5. The scroll pump evacuates through valves 6 - 1 - 8 - 10 - 9 - 4, the compressor's bypass valve is open as well. The scroll pump is used to evacuate large quantities of gas but is insufficient to purge the GHS to prevent later blockages in the test chamber capillary. Thus when the GHS pressure allows (pressure less than



about 100 mTorr) then valve 7 is shut and the GHS is evacuated further using the turbomolecular pump. The number and length of lines means that this step can be lengthy but does not need to be repeated frequently.

More common is the need to purge the test chamber. This is most easily done using the turbomolecular / dry pump combination to evacuate through the test chamber vent line: through valves 5 - 8 - 10 - 12 - 13. The GHS conveniently allows for monitoring of the test chamber capillary with pressure gauges at the start of the capillary ( $P_{eye}$ ) and at the outlet of the test chamber ( $P_{vent}$ ). This is important to ensuring the capillary is not blocked by impurities.

While the use of a closed gas system for the test chamber GHS should sidestep the need for extensive purifications steps, it is expected that this will only be fully true after a number of condensation - evaporation cycles as each cycle produces a slightly cleaner gas supply. Until such a state is reached, gas condensation required a step for purification of gas batches. The 40 liter ballast tank was filled from the Big Tank reservoir, then the gas was circulated using the compressor through valves 6 - 11 and back to the ballast tank for recirculation. Cleaning was done through the liquid nitrogen cold trap. Larger scale purification which includes the Big Tank reservoir can be made if valves 1 - 4 - 14 are opened.

The available volume inside the test chamber was calculated to be 808 cm<sup>3</sup>, or about 25 moles of liquid helium. It was necessary to keep accurate count of the amount of helium condensed into the test chamber to prevent over filling, which could lead to runaway heat loads, or under filling which could expose the active volume to vapor and impact the amount of ionization generated. The gas handling system in Fig. 5.15 made the liquefaction and tallying of gas straightforward. The ballast tank with its pressure gauge allowed for controlled amounts of gas to be purified and sent into the test chamber. Pressure readings at the inlet and outlet of the test chamber ensured that liquid was produced when the outlet pressure measured the liquid vapor

pressure corresponding to the temperature of the test chamber. Owing to the very low vapor pressure of LHe below 1 K, liquefaction was best achieved when the dilution refrigerator was in stage 2 cooling. The majority of time was spent in purifying each batch of gas and in allowing the dilution refrigerator to recover to its normal operating state since the heat load from the influx of warm gas and warm liquid caused pressures in the dilution mixture circuit to rise to abnormal levels. Typical rates of condensation were 4-5 moles per hour, for batches of 0.4 - 0.5 moles at a time. Thus it was possible to liquify the desired 800 cm<sup>3</sup> in just a several days.

## 5.4 Signal generation

The prototype ionization chamber was able to operate in pulse mode and current mode. In pulse mode the deposited  $\alpha$  energy in the form of ionization is collected at the ground electrode and amplified into a measurable voltage signal, Fig. 5.16. The amplitude of the voltage pulse is proportional to the amount of ionization produced. The rise time of the voltage pulse is proportional to the drift time of the ionization and the decay of the pulse depends on the  $RC$  time constant of the charge collector. Pulse mode detection was configured using an Amptek A250 charge-sensitive preamplifier connected directly to the ground electrode inside the test chamber. The A250 is well-suited for this application owing to its low intrinsic noise, low power, fast rise time and configurable decay time constant and gain using feedback components.

The commercial Amptek board with A250 preamplifier is shown in Fig. 5.17. Clean power to the A250 is provided using eight 1.5 V batteries which provide  $\pm 5$  V for the A250 and also the bias voltage for the over-current protection shown in Fig. 5.18. Several iterations of over-current circuits were necessary before arriving at a satisfactory design. Jumper cables can be used to configure the variable feedback (shown in the lower left of Fig. 5.17) depending on the application.

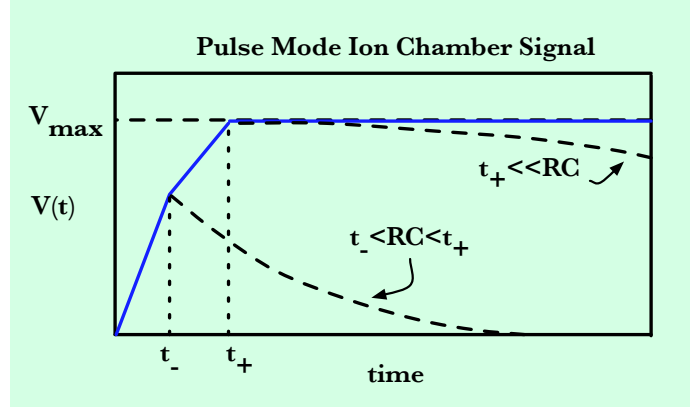


**Figure 5.16:** *The ideal charge collection pulse capable of discriminating between charge species with the use of appropriate decay time constants.*

Pulse mode ionization chambers, though limited in the number of applications, find use in specialized applications and in neutron detectors [91]. In the usual pulse mode configuration, an ionizing particle deposits energy between two electrodes in the form of charge pairs. These charges drift toward the electrodes and produce induced charges in the electrodes, reducing the voltage applied to the electrodes. The change in electrode voltage causes a corresponding voltage to appear in the external circuit and this voltage can be measured. Such a configuration is typically used with a voltage-sensitive amplifier. In voltage-sensitive amplification the signal voltage is given simply by  $V = Q/C$  where  $Q$  is the charge collected (induced) on the electrodes and  $C$  is the detector capacitance and any parallel capacitances [91]. Once all the charges have arrived at the electrodes then the total induced charge is equal to the charge that has arrived at the electrodes [92].

Charge-sensitive amplification can be used to remove dependence on the detector capacitance. The ideal pulse signal is shown in Fig. 5.16 [91]. A kink in the rise

The diagram shows the A250 module with the following components and connections:

- Power Supply:** +6 V (Pin 10) and -6 V (Pin 4). A compensation pin (Pin 6) is labeled COMP.
- Internal Components:**
  - Resistor R between Pin 12 and Pin 11.
  - Capacitor 0.047 between Pin 12 and Pin 13.
  - Resistor 50 between Pin 11 and Pin 10.
  - Resistor 1K between Pin 13 and Pin 14 (INPUT).
  - Capacitor 300M between Pin 1 and Pin 2.
  - Capacitor 1 pF between Pin 2 and Pin 3.
  - Capacitor 2 pF between Pin 3 and Pin 4.
  - Capacitor 4 pF between Pin 4 and Pin 5.
  - Resistor 50 between Pin 5 and Pin 6.
  - Capacitor 0.047 between Pin 6 and Pin 7.
  - Resistor 100 between Pin 7 and Pin 8 (OUTPUT).
- External Connections:**
  - EXTERNAL FET:** Drain (D) to Pin 14 (INPUT), Gate (G) to Pin 1, Source (S) to Pin 2.
  - DETECTOR:** Connected to Pin 1.

**Figure 5.18:** *The over-current protection circuit designed to protect the A250 from sparks in the detector. The FET corresponds to the external FET in the A250 diagram.*

Figure 5.18 shows the over-current protection portion of the A250 configuration. The over-current protection circuit sits between the detector output (from the ground electrode) and the FET at the A250 input and is designed to dissipate harmful transients and current surges due to sparks into ground. Figure 5.18 also shows the test input portion of the A250 design. A square-wave voltage can be sent through this input to produce charge in the 0.5 pF test capacitor to mimic charge produced in the detector. Using the simple relation  $Q = CV$  the amount of charge produced in the test capacitor can be calculated and from the corresponding A250 output pulse it is possible to determine the actual gain of the A250. It was determined that a feedback capacitance of 0.1 pF corresponded to an *actual* gain of 1.8 V/pC.



**Figure 5.19:** Photo of the shielded box containing the A250 board and over-current protection circuit. Power inputs are in yellow and additional connections are for bias for over-current protection, test signal, detector input and A250 output.

Most ionization chambers are operated in current mode which can have some

advantages over pulse mode operation depending on the application. For example, in current mode random noise fluctuations can be averaged out and are less likely to contribute to spurious events. Noise contributions in pulse mode compound over time and spurious events accumulate in addition to actual events. For pulse mode operation to be satisfactory much greater care is needed for shielding and grounding.

In current mode a SRS model 570 current-sensitive preamplifier is used to convert the DC ionization signal from the drifting charges into a voltage offset. The output is then amplified and filtered and the voltage offset is measured using a digital oscilloscope (see Fig. 5.20). In both modes of operation, high voltage (up to 5kV) is supplied using a SRS PS350 reversible polarity power supply. To reduce damage to the electroplated source on the ground electrode when a spark occurs, a high voltage 100 M $\Omega$  resistor is used in series with the high voltage cable.

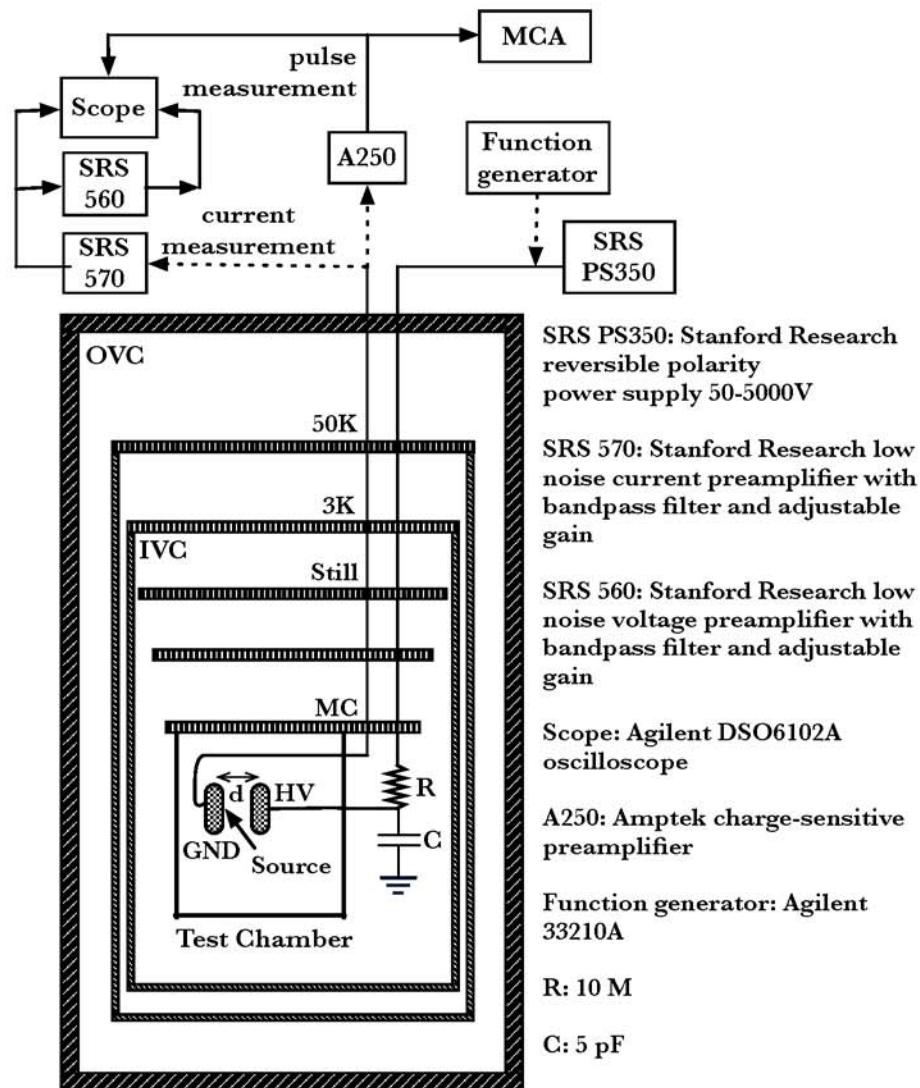


**Figure 5.20:** *Pulse and current mode configuration.*

### 5.5 Simulated ionization pulse distribution

A MATLAB script was created to simulate the effect of stopping distance on the measured pulse height distribution. By varying the range of alpha particles the script effectively mimics the conditions of varying density gas and simulates the impact of

gas density changes for the actual electrode geometry. Some physical effects which the script does not take into account are edge effects of the electric field, instead the collection volume is taken to be the volume enclosed by the electrode gap. Also not taken into account are recombination losses of the ionization charges which depend principally on the electric field magnitude and density of the ionization (thus depend indirectly on the range of alpha particles). In this way the script was meant to give an estimated depiction of the pulse height distribution.

Special attention is given to a proper  $\cos\theta$  distribution of alpha particle trajectories from the surface of one electrode. For each alpha event the inverse cosine is taken of a randomly generated number. This is used to calculate the  $\phi$  coordinate in spherical coordinates according to

$$\phi = \pi/2 - \arccos(x) \quad (5.16)$$

where  $x$  is a random number between 0 and 1.  $\theta$  is also generated randomly between 0 and  $2\pi$ . The range is generated from a normal distribution around a mean range which is entered manually into the script.



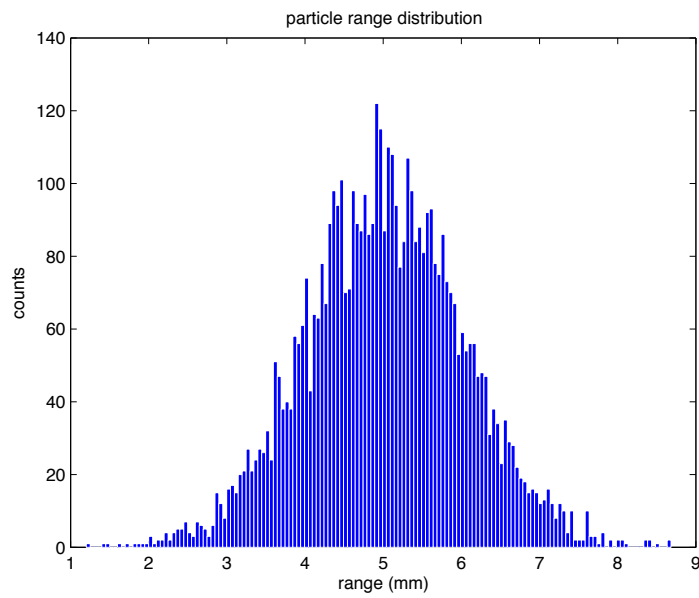


**Figure 5.21:** *Normal distribution of alpha particle ranges around a mean of 5 mm for 5,000 particles and 150 bins.*

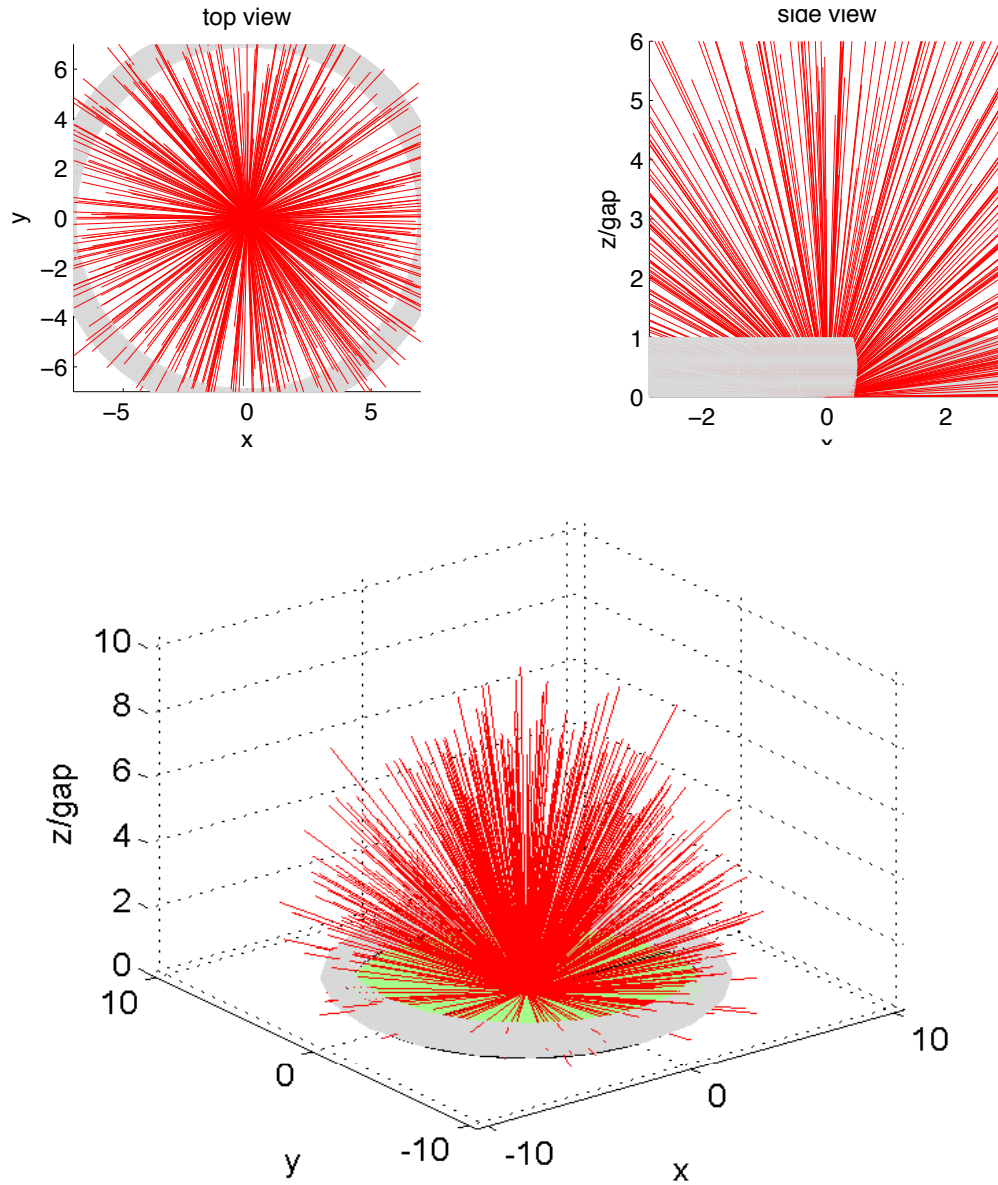


**Figure 5.22:** *Top, side and 3D views of generated alpha trajectories, dimensions in mm, top electrode not shown.*

From the alpha particle ranges the amount of ionization is computed based on the fraction of the range within the collection volume contained directly between the two electrodes. In this sense the simulation is purely based on geometrical effects. The maximum charge which can be produced (corresponding to an alpha range fully within the collection volume) is just the energy of the alpha particles, 5.5 MeV for  $^{241}\text{Am}$ , divided by the mean ionization energy of the gas. For Helium the mean ionization energy is 41 eV. Thus the maximum charge, neglecting  $\delta$ -rays and recombination, which can be produced is 134000 e. The generated charge from each alpha track is then converted into a voltage using the numerical gain of the A250 charge-sensitive preamplifier.

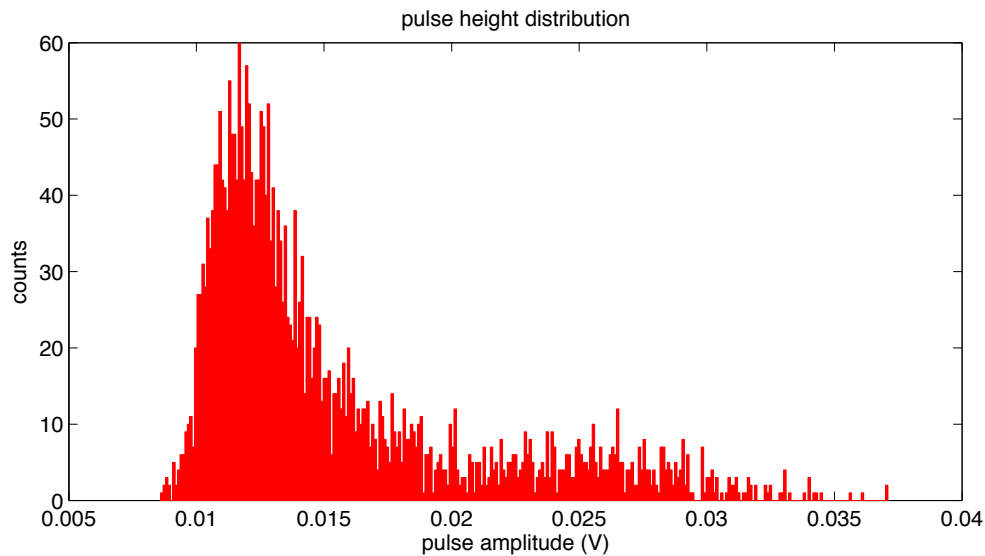


**Figure 5.23:** *Simulated voltage pulse height distribution using a mean alpha particle range of 10 mm in Helium gas and 3000 particles.*

A typical pulse height spectrum is shown in Fig. 5.23 for a 10 mm average range. Even for a simulated range which exceeds the actual range by a factor of 3 there

appears to be some structure from purely geometric considerations. This simple calculation indicates that if the electronic noise can be controlled to about 10 mV then some  $\alpha$  ionization pulse structure should be discernible.

## 5.6 Interface for pulse acquisition

A graphical user interface (GUI) was designed using MATLAB capable of communicating with a digital oscilloscope and acquiring pulse data. The goal of the GUI was to capture waveform data of each pulse inside liquid helium (above some trigger value) and determine the drift speed of charges. When the oscilloscope registered an event then the digitized waveform was transferred to the GUI and displayed. The GUI identified the rising edge of the pulse and calculated its slope (the drift speed of charges) using a subset of the rising edge which disregarded points close to the beginning and end of the rising edge. The code then compiled a running histogram of the velocity data and could be set to record for a determined length of time or until a certain number of pulses were acquired. The digitization, transfer and recording of waveform data occurred at a rate of about 3 Hz.

Figure 5.24 shows the GUI operating with a test pulse generated by a square wave across a test capacitor inside the A250 detector package. The GUI performed well in testing, but for reasons that will be discussed later, it was not useful for drift measurements inside liquid.

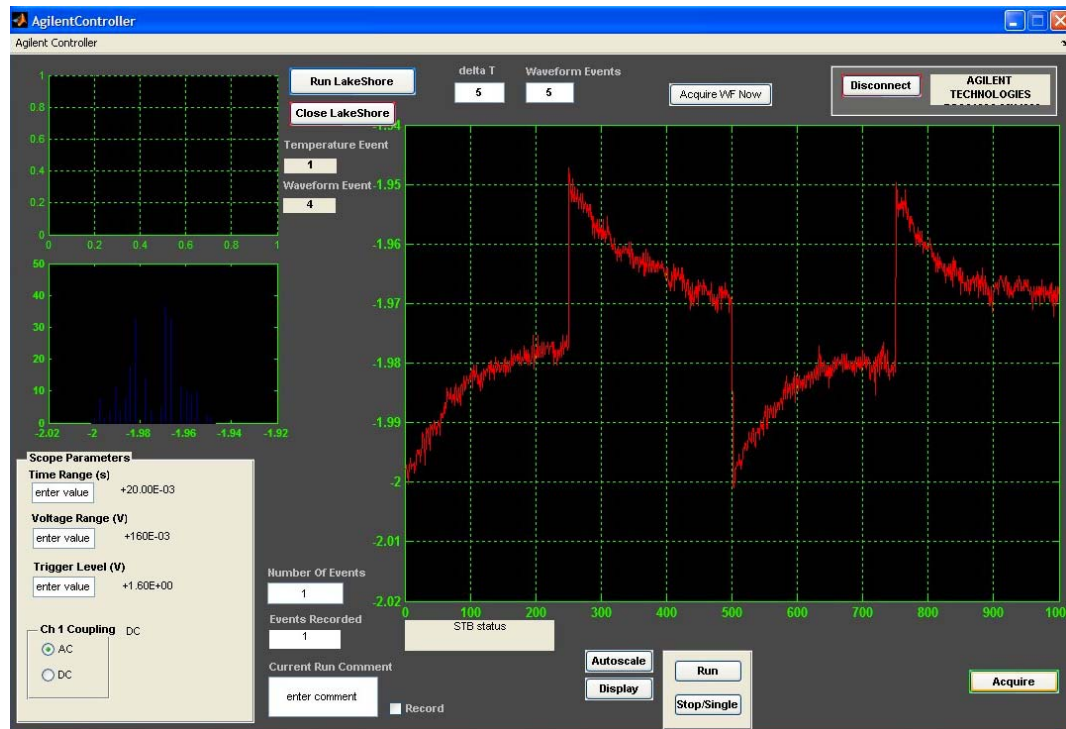


Figure 5.24: MATLAB GUI for acquiring ionization pulse waveform data.

## 5.7 Gas ionization measurements

Nominally 300 Bq of  $^{241}\text{Am}$  was electroplated on the ground electrode, however some of the source was damaged during shipping from Los Alamos to IU. In addition subsequent high voltage sparking could have further damaged the remaining electroplated source. The ionizing particle here is the  $^4\text{He}$  nucleus, also known as the  $\alpha$  particle,



where the  $\alpha$  energy is 5.5 MeV.

Pulse mode measurements in gas showed about 160 Bq source activity (4.3 nCi), the rate showed no dependence on voltage for low fields. It was necessary to keep

electric fields low in gas to reduce the risk of sparks and damage to the source.

According to classical kinetic theory the zero-field electron mobility is given by [96]

$$\mu_0 = \lim_{E \rightarrow 0} v_D/E = \frac{4e}{3N(2\pi m)^{1/2}(k_B T)^{5/2}} \int_0^\infty \frac{\epsilon}{\sigma(\epsilon)} \exp(-\epsilon/k_B T) d\epsilon \quad (5.18)$$

where  $N$  is the gas number density,  $\epsilon$  the electron energy and  $\sigma(\epsilon)$  the momentum-transfer electron-atom scattering cross-section. The weak energy dependence of  $\sigma$  means that

$$\mu_0 = \frac{4e}{3N\sigma_0(2\pi m k_B T)^{1/2}}. \quad (5.19)$$

For sufficiently low gas number densities, below about 0.5 atoms/nm<sup>3</sup> the classical zero-field approximation is in good agreement with experimental results. At higher gas densities (above 1 atom/nm<sup>3</sup>), or pressures approaching saturation ( $P/P_s > 0.6$ ), electrons become localized and there is a very large and sudden decrease in mobility. For large field strengths, the experimental electron mobility approaches the classical kinetic theory prediction [108]

$$\mu N = -\frac{e}{3} \left( \frac{2}{m} \right)^{1/2} \int_0^\infty \frac{\epsilon}{\sigma(\epsilon)} \left( \frac{dg(\epsilon)}{d\epsilon} \right) d\epsilon \quad (5.20)$$

where  $g(\epsilon)$  is the solution to the Boltzmann equation

$$g(\epsilon) = A \exp \left\{ - \int_0^\epsilon \left[ k_B T + \left( \frac{M}{6m} \right) \left( \frac{eE}{N} \right)^2 \frac{1}{z\sigma^2(z)} \right]^{-1} dz \right\} \quad (5.21)$$

where  $M$  is the He mass and  $A$  is a normalization constant.

In Fig. 5.25 are shown ion drift velocities as deduced from the A250 ionization pulse rise times in helium gas. Pulse rise times were in the 10  $\mu s$  range, well within the 20 ns rise time capability of the A250. The measurement was made in 270 mbar He gas at 4.8 K (gas density 0.41 atoms/nm<sup>3</sup>), using only stage 1 cooling of the dilution refrigerator. Positive polarity was used making the collector electrode the cathode and thus sensitive to He ions.

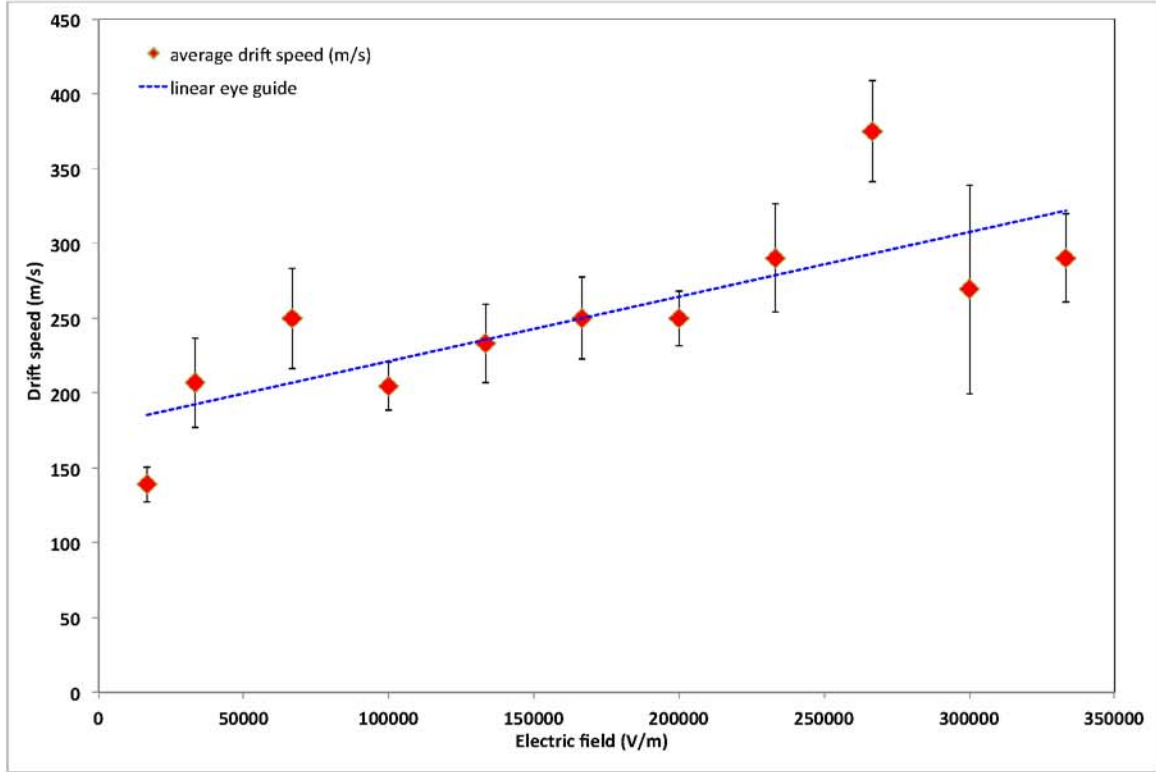


**Figure 5.25:** *Helium ion drift velocity based on  $\alpha$  ionization pulse rise times in cold gas,  $T = 4.8$  K and gas number density  $0.41$  atoms /  $\text{nm}^3$ .*

The measured  $\text{He}^+$  drift is in the same range as accepted quasi-localized electron mobilities at 4.2 K and pressure saturation fractions  $P/P_s \sim 0.6 - 0.7$  [96]. This is the region where thermal electrons rapidly approach their fully localized bubble form. It is not known at what cold gas density or temperature the  $^+\text{He}$  ion forms a snowball.

It should be noted that in LHe the snowball effective mass is about  $1/4$  the effective mass of the electron bubble and the electron bubble mobility is less than the snowball mobility. Thus it is not surprising to find that for quasi-localized electrons the mobilities of the two species would be in proximity.

Several authors have recently presented data on the mobility of  $\text{He}^+$  ions in cold gas, [109], in terms of the reduced mobility given by

$$K_0 = \frac{v_d}{N_0} \frac{N}{E} \quad (5.22)$$

where  $N$  is the number density,  $E$  the electric field,  $v_d$  drift velocity and  $N_0$  the Loschmidt number (the gas density under STP) is  $2.68676 \times 10^{25} \text{ m}^{-3}$ . The reduced electric field  $E/N$  is the main factor for determining the reduced mobility. The authors produced ions using an electron impact ion source and selected them using a filter before collimating and injecting the ions into a drift tube. Shown in Fig. 5.26 are the measured reduced ionic mobility in cold He gas from [109].

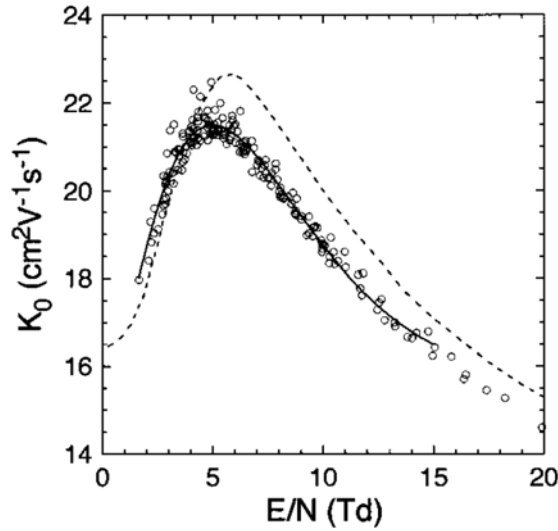


**Figure 5.26:** *Reduced ion mobility as a function of the reduced field from [?]. The units for  $E/N$ , Td, are defined as  $10^{-21} \text{ V m}^2$ , [109].*

The reduced ionic mobility in cold gas as deduced from the ionization pulses using  $^{241}\text{Am}$  is more than an order of magnitude higher than the accepted values. This result is not surprising primarily due to the fact that the ion drift distance is not well defined



since ions are produced all along the  $\alpha$  track. For this reason the measured pulse rise time will depend on the direction of the  $\alpha$  trajectory: ions produced by trajectories nearly parallel to the electrode surface have better-defined drift length equivalent to the electrode gap. Most  $\alpha$  tracks which produce pulses will not be along this favorable direction for an accurate mobility measurement. For most ions the drift length will be significantly less than the gap size thereby producing artificially high drift speeds. The design constraints of this experiment made measurements of mobility in gas not feasible.

While the investigation of mobility is not practical with the required design, an analysis of the ionization pulse height distribution and ionization current can yield meaningful results.

### 5.7.1 Helium gas ionization current

If the  $\alpha$  particles could be made to deposit all or most of their energy inside the active volume it could result in a current of approximately 3.4 pA for the 4.3 nCi source, a current which could be easily detectable if the recombination loss is small.

Figure 5.27 shows the various regions of operation for drift chamber detectors equipped with single wire configuration. The single wire configuration allows for gas gain in the vicinity of the wire and operation in proportional mode which can produce larger signals. We are primarily concerned with regions I and II however given the planar geometry, since proportional mode or higher with planar geometry will mean frequent sparking.

Current mode operation was achieved using the Stanford Research Systems 570 Low Noise Current Preamplifier. The SRS 570 includes bandpass filter capability, adjustable gain and converts the input current into a voltage for convenient observation on a digital oscilloscope. The voltage offset on the oscilloscope was measured for a

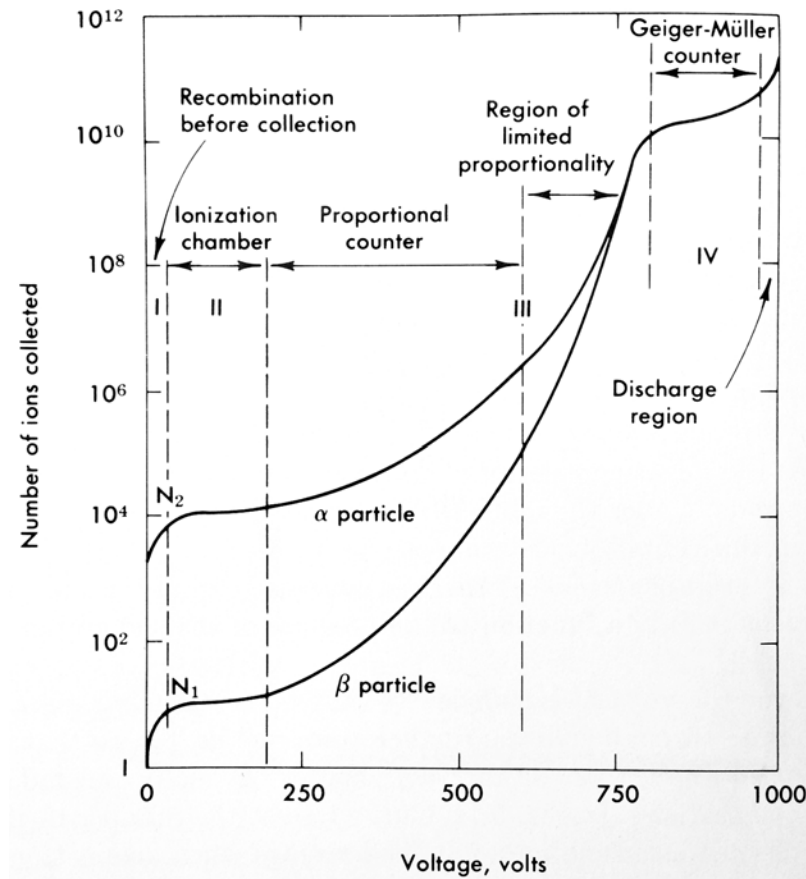


**Figure 5.27:** *Number of ions collected with increasing voltage for  $\alpha$  and  $\beta$  particles. Note the presence of saturation in region II. From [94].*

variety of chamber bias voltages and knowing the gain the ionization current can be deduced. Optionally, the output voltage can be sent through a SRS 560 Low Noise Voltage Preamplifier for additional filtering or gain but this was not typically used. One advantage of current mode operation over pulse mode in this experiment was the less detrimental effect of noise on the measurement. Due to the nature of current acquisition it is inherently an averaging process and high frequency noise components,

even 60 Hz, can be mitigated and influence the measured current in a less significant way than pulse mode operation.

An  $I - V$  curve relating the applied voltage to ionization current should approach a saturation level corresponding to a suppression of the recombination effect. At zero applied voltage across the active volume the collected current should also be zero and all produced ionization will be lost to diffusion out of the active volume and recombination. For increasing voltage the amount of collected ionization current will increase since recombination loss scales inversely with voltage. The saturation current provides information about the rate of formation of ionization in the active volume [91].

In light of the low stopping power of Helium gas, room temperature gas ionization measurements were shelved in favor of low temperature Helium gas tests. Additionally, because of concerns over the fragility of connections and feedthroughs it was deemed unwise to use excessive pressure at room temperature. The higher gas density at low temperature meant that measurements could be made at high density rather than high pressure, provided that precautions were made to stay *below* the Helium saturation curve.

The pressure of the test chamber was measured using  $P_B$  in Fig. 5.15 since the connections along the test chamber vent line remain open during operation. Cooling to 4 K was provided by the pulse-tube compressor which allowed for testing in cold dense He gas. In Fig. 5.29 are shown the measured background-subtracted saturation currents for varying pressures in the test chamber. There is a distinct linear portion in the pressure dependence indicating that the stopping length of the  $\alpha$  particles exceeds the active volume. The saturation current at the final pressure, just below the saturation pressure at 4 K, indicates that the saturation current approach a limiting value, consistent with the increased stopping power of higher density gas where  $\alpha$ 's are depositing all of their energy in the active volume. The limiting saturation current

is in good agreement with the predicted ionization current of 3.4 pA.

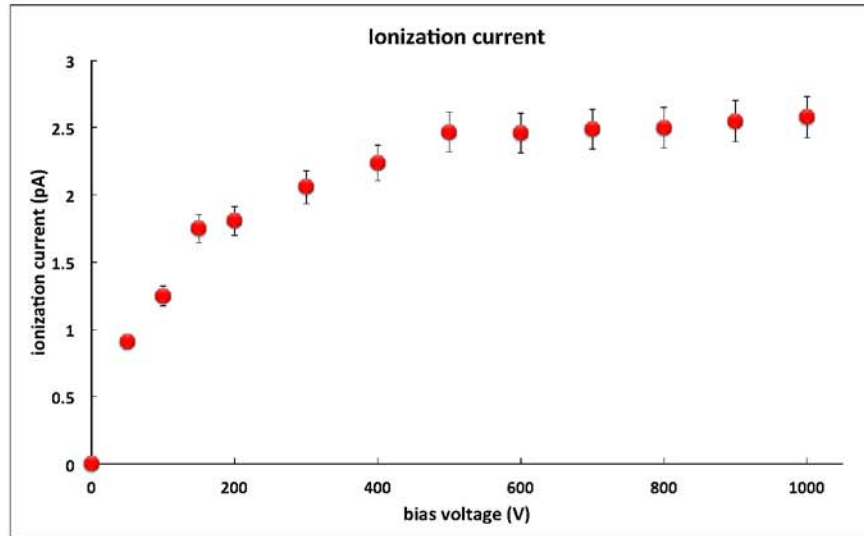


**Figure 5.28:** *Background-subtracted ionization current for  $T = 5.2$  K and  $P = 890$  mbar. The ionization current becomes saturated around 500 V.*

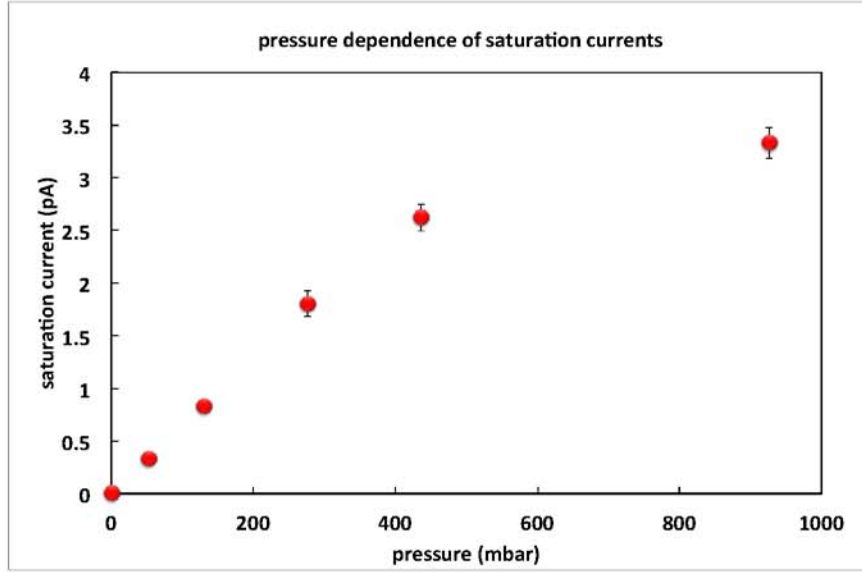


**Figure 5.29:** *Background-subtracted ionization saturation currents in cold dense Helium gas.*

### 5.7.2 Pulse mode in gas

Pulse mode operation was done using a commercial Amptek A250 charge-sensitive preamplifier, see Fig. 5.19. Charge was collected on the ground electrode and the signal carried by semi-rigid coaxial cryogenic cable with a solid metal shield made by LakeShore Cryotronics. Under the 3 K plate the cryogenic cable connected to a LEMO cable which was thermally anchored to the 3 K plate. The LEMO cable was routed around fourteen radiation baffles through the central access port of the dilution refrigerator to a room temperature feedthrough. Once outside the dilution refrigerator, test chamber output connected to the over current protection circuit Fig. 5.18 and then to the front-end FET on the A250 board, Fig. 5.17. The collected charges were then integrated with a theoretical gain inversely proportional to the

feedback capacitor,

$$\text{gain} = \frac{1}{C_f} \left[ \frac{\text{Volts}}{\text{picoCoulomb}} \right] \quad (5.23)$$

where  $C_f$  is measured in pF. A feedback capacitor of 0.1 pF was selected and drain resistance of 1-2 G $\Omega$  for time constants of 1 ms or less. Measurements with test pulses and the 0.5 pF test capacitor indicated that the actual gain was 1.8 volts/pC. The slow time constant helped ensure all the charge would be collected for each event but not so slow to cause pileup for the  $\sim 4.3$  nCi source. To reduce the risk of damage to feedthroughs and the risk of sparking, low temperature dense gas tests were the preferred test bed. The charge pulse amplitude was also significantly helped by the improved density of cold gas. The raw signal from the A250 preamplifier could be monitored on a digital oscilloscope or filtered and amplified using the SRS 560 Voltage Preamplifier or amplified using the Ortec model 672 spectroscopic amplifier. The signal was then recorded as a voltage pulse height spectrum using a FAST ComTec MultiChannel Analyzer (MCA) mounted in a PCI slot inside a computer. The MCA control software could save data in several formats, such as ASCII, which was then analyzed with MATLAB.

If the  $\alpha$  particle deposits all its energy in the active volume, then, neglecting recombination loss, it should yield 134000 ion pairs, or 0.021 pC of charge. A feedback capacitance of 0.5 pF should then produce raw voltage pulse amplitudes up to 42 mV assuming no gas gain and neglecting stray capacitances affecting the A250 gain. Additional pulse amplification was provided using a spectroscopic amplifier with gain between 200 and 500 before recording the signal with the MCA.

Pulse height distributions were measured for helium gas temperatures of 293, 6 and 4 K. For each temperature a background measurement was made with zero applied voltage and then subtracted from distributions with applied voltage.

Figure 5.30 shows the raw ADC pulse spectrum after amplification of the A250

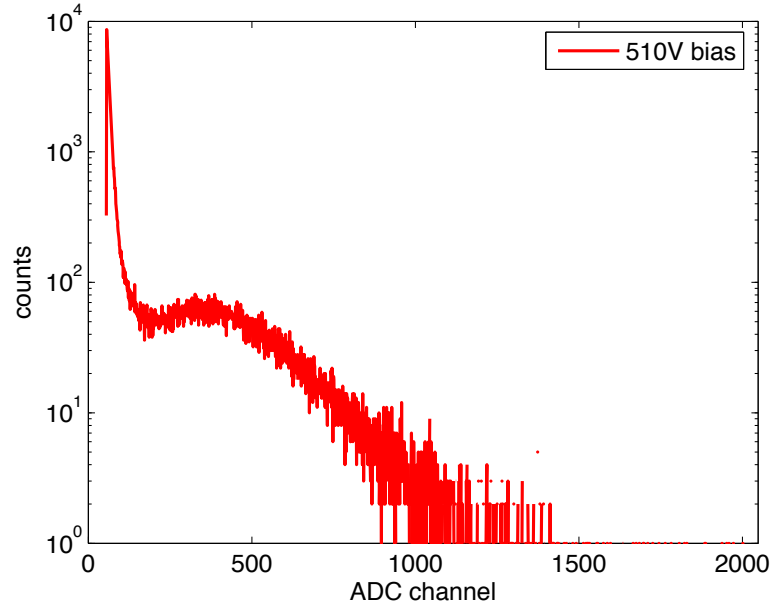


**Figure 5.30:** *Raw ADC pulse height distribution in 293 K helium gas at 771 mbar with amplifier gain of 200.*

output with charge integrating feedback capacitance of 0.5 pF. The ADC channel spectrum corresponds to pulse heights of 0-10 volts. Thus the raw A250 pulses are below about 30 mV.

In Fig. 5.31 are shown A250 pulse height spectra converted into charge produced per pulse. The spectra were recorded in helium gas at 293 K and pressure of 771 mbar. The pulse rate, above the noise cutoff corresponding to channel 170 on the MCA, was about 92 Hz for an applied voltage of 510 V. A large fraction of the pulses (corresponding to events normal to the electrode surface and therefore ones which produce relatively little ionization) are hidden inside the noise.

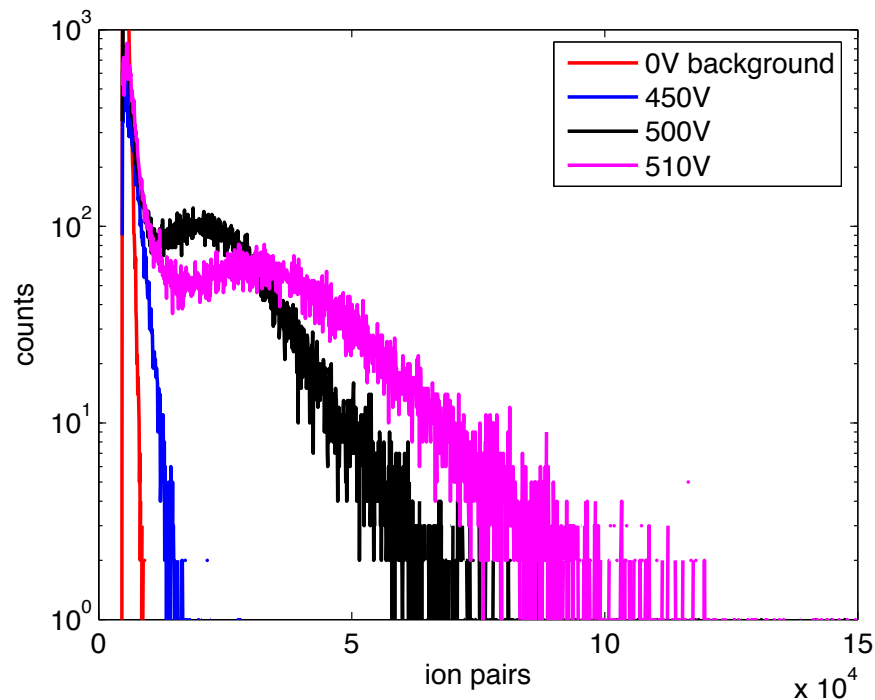


**Figure 5.31:** *Background-subtracted ionization collection spectrum in 293 K helium gas at 771 mbar and amplifier gain of 200.*

Figure 5.32 shows that at low temperature the amount of charge collected has dropped significantly. While recombination loss is likely present, measurement of the ionization current in Fig. 5.28 shows that the charge collection is at saturation. Thus the most likely reason for the smaller pulses is the quasi-localization of charges. As the gas density is increased and the temperature decreased, ions and electrons do not behave as simply as they do at 293 K. The slower drift time can mean that charge begins draining from the integrating capacitor before all the charge for an event can be collected. An ionization current amplifier would not be subject to this effect and therefore would measure a larger ionization.

Figure 5.33 shows the background-subtracted ionization pulse spectrum in 4.5 K



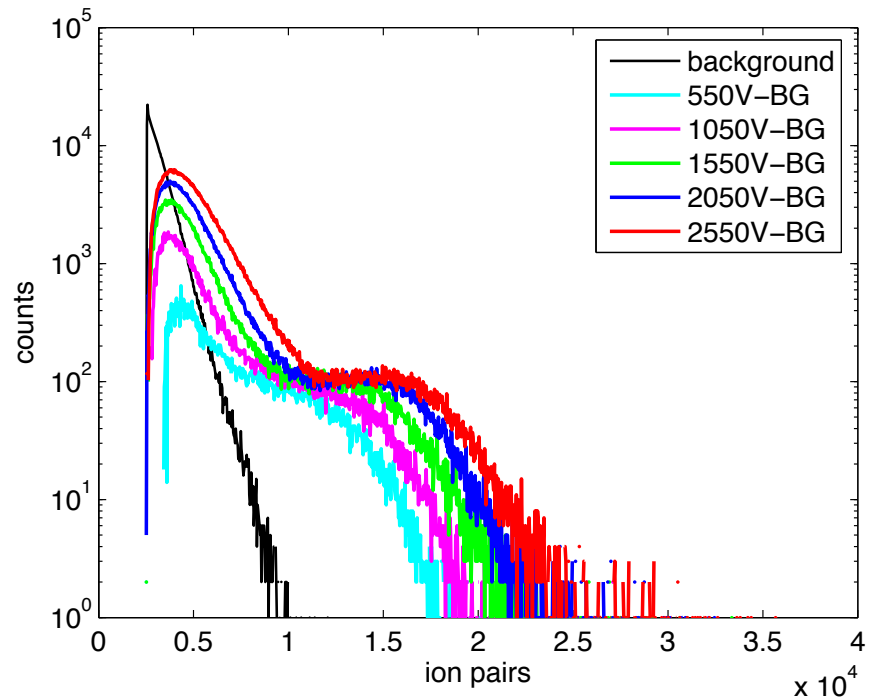


**Figure 5.32:** *Background-subtracted ionization spectra for various bias voltages measured in 6.5 K helium gas at 784 mbar and amplifier gain of 500.*

helium gas and 30 mbar pressure. Hardly any ionization pulses were visible above the noise indicating further decrease in the drift velocities of charges.

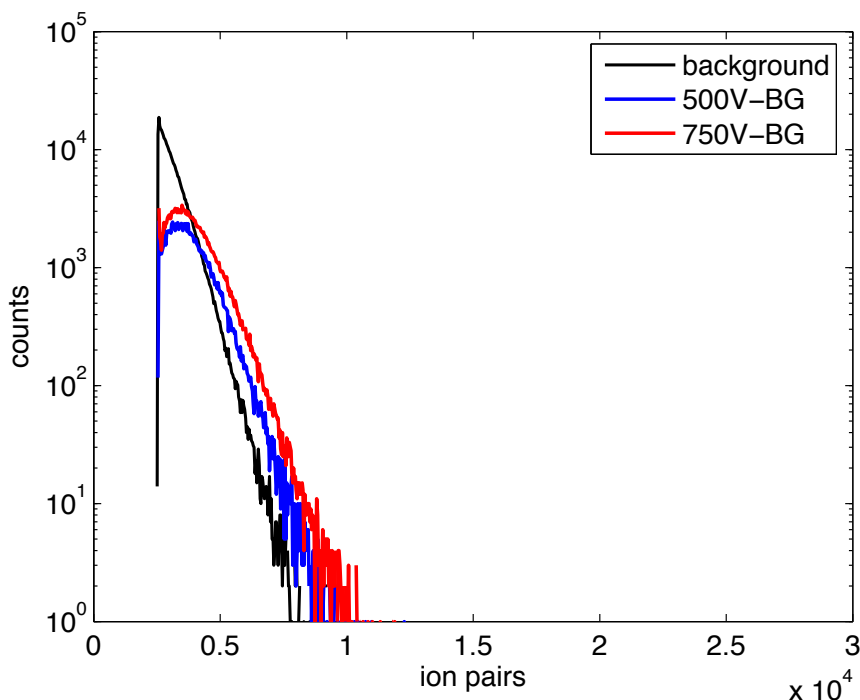


**Figure 5.33:** *Background-subtracted ionization spectra for bias voltages measured in 4.5 K helium gas at 30 mbar and amplifier gain of 500.*

## 5.8 Liquid Helium Ionization Current

Ionization pulses of any kind were no longer visible with the A250 configuration when the test chamber was filled with liquid helium. Data which yielded any information about ionization inside the liquid all came from measurements of the ionization current with current-sensitive amplification using the Stanford Research Systems 570 preamplifier. A gain of 1 V/pA was used and the corresponding RMS voltage offset was measured with a digital oscilloscope. Each measurement consisted of an average of several hundred traces and the standard deviation for each average was also

recorded.

It was expected that there would be some leakage current, proportional to the applied voltage, which would provide an ohmic contribution to the ionization current. The ohmic region can be identified by the linear region of the  $V - I$  curve, the slope of which can determine the resistivity of the liquid.

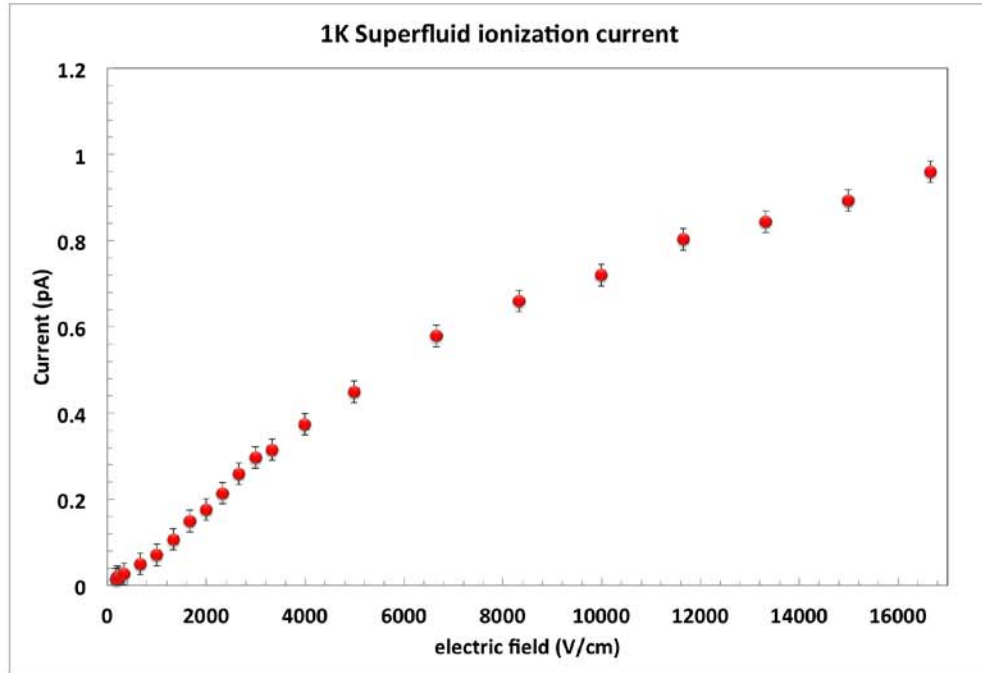


**Figure 5.34:** *Background-subtracted ionization current in superfluid at 1 K and 0 - 5000 V.*

## 5.9 Discussion

To reduce the risk of damage to the electroplated  $^{241}\text{Am}$  source on the ground electrode, it was necessary to keep the fields well below the breakdown field. Based on critical velocities of charges in He-II, however, it is unlikely that higher fields would

correspond to more pronounced pulse signals or measurable improvement in recombination losses. Perhaps the most detrimental losses were due to diffusion. Experiments of this type rely on field uniformity, such as with a Frisch grid, and ion gates for precise determination of transit times. Several problems prevented this experiment from making use of those tools:

- the presence of field grids or gates would be a poor approximation to the actual nEDM experiment
- the goal of the investigation was not the precise determination of drift speed, such measurements were already done, but instead to test the LHe detector concept as relates to the nEDM cell

Figure 5.35 shows a pulse height spectrum from  $^{241}\text{Am}$  in liquid xenon [110]. The authors achieve a gain of about 20 using  $3.5\ \mu\text{m}$  anode wires with anode fields around  $3 \times 10^6\ \text{V/cm}$ . The amplitude of the  $\alpha$  peak is reduced by a factor of 15 due to recombination. The width of the  $\alpha$  peak is also attributed to the variations in recombination when particles are emitted at different angles relative to the electric field. Contrasting this with the conditions which were possible in the experiment of this chapter, viz. fields  $< 6 \times 10^4\ \text{V/cm}$  and nEDM experiment fields  $\leq 7.5 \times 10^4\ \text{V/cm}$ , it becomes apparent there is little chance of operating pulse mode in LHe.

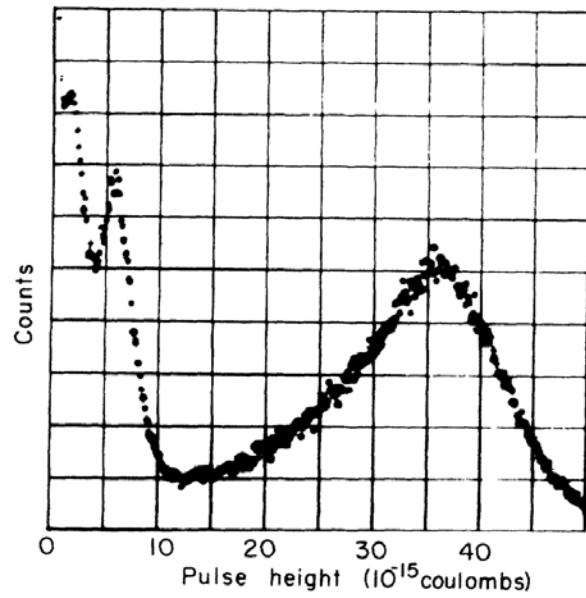


**Figure 5.35:** *Pulse height distribution with large  $\alpha$  peak and smaller  $\gamma$  peak in liquid xenon, from [110]*

## Chapter 6

# Neutron Detection Cryostat

The principal challenge of ionization detection using the electroplated  $^{241}\text{Am}$  source of the previous chapter was the fact that the source could not be modulated. To conduct background measurements without the source in the test chamber would require at least a couple weeks just to swap the electrode, ensure (superfluid) leak tight seals, cool down and condense liquid. Such a process would be impractical to say the least for diagnosing a detector design. The prudent course instead was to develop a small, portable cryostat which could be used with the Low Energy Neutron Source at Indiana University.

### 6.1 Low Energy Neutron Source

The Indiana University Low Energy Neutron Source (LENS) was completed in 2006 and was the first university-based pulsed neutron source in the U.S. LENS was born out of a desire for an alternative to large scale neutron facilities where competition for beam time is sometimes prohibitively high. A small facility like LENS, though boasting a smaller operational flux than national facilities, is better-suited for rapid

prototyping and is easily accessible to students.

LENS supports three beam line stations: small angle neutron scattering, spin echo scattering angle measurement and MIS, 6.1. The Middle Instrumentation Station, or MIS, is versatile in its ability to accommodate diverse measurements with fast turnaround and is specifically intended for the development and testing of novel instrumentation.

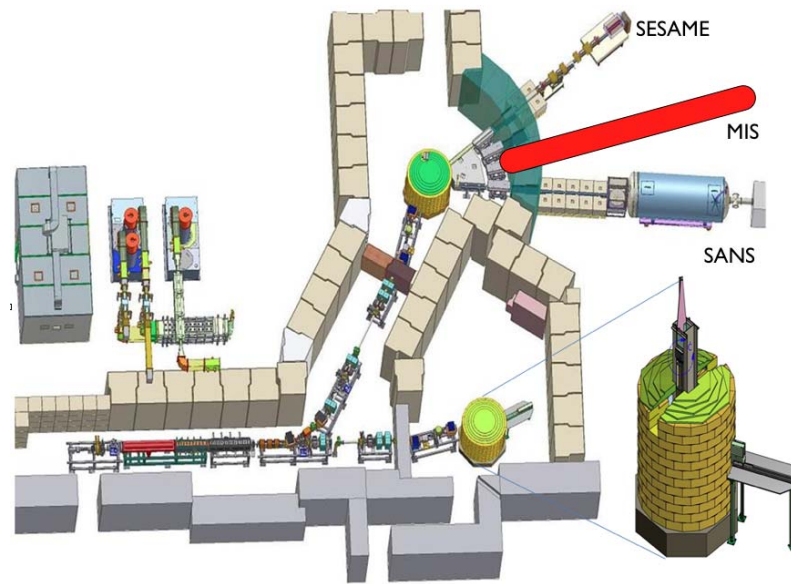


**Figure 6.1:** *The Low Energy Neutron Source with three beam line stations.*

LENS utilizes low energy (p,n) reactions in a beryllium target coupled to a light water reflector and cold methane moderator. 13 MeV protons are supplied by a LINAC peak current around 25 mA and pulse widths ranging from 10  $\mu$ s to 1 ms and repetition rate of 10-40 Hz depending on the experimental needs. The low energy of the proton beam allows for a lower temperature moderator which gives a colder neutron spectrum. Figure 6.2 shows the neutron flux spectrum at MIS.

A new detector workstation which overcomes a primary challenge described in Chapter 5, i.e. the ability to readily control the source and distinguish the signal from the background, was designed for use with LENS.

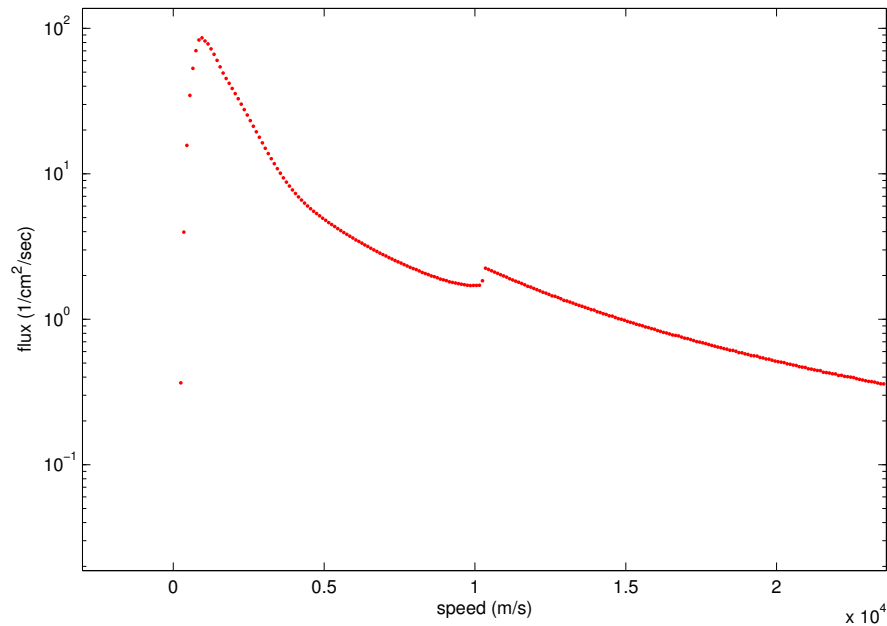


**Figure 6.2:** *Measured flux at MIS beam line. Integrated flux 1700  $cm^{-2}s^{-1}$*

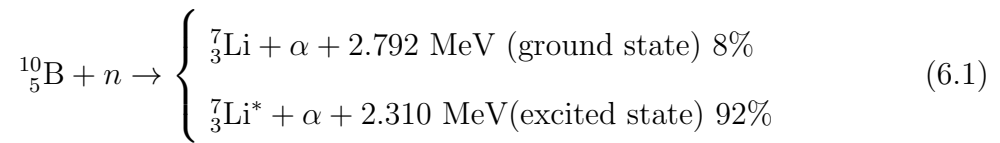
## 6.2 Design

The design of the neutron detector was based around a commercial RC102 continuous flow cryostat manufactured by Cryo Industries shown in Fig. 6.4. The detector is contained inside a commercial ceramic isolator made by CeramTec. A larger custom heat shield and vacuum jacket needed to be made to accommodate the isolator inside the cryostat.



A small opening was made in the cryostat cold head and a corresponding opening in the isolator top flange for gas and liquid delivery, as shown in Figs. 6.6 and 6.5. The top flange is sealed to the cold head with indium and the bottom flange with the detector mount is sealed to the isolator using a kapton gasket. The mounting flange for the detector body seals the isolator. The flange has stycast epoxy feedthroughs for high voltage, grounding and temperature wires as well as several redundant wires shown in Fig. 6.9. All the joints were helium cold leak tested at 77 K.

The assembled detector is shown in Fig. 6.7 mounted to the isolator flange. The assembly is under three inches high and has an adjustable electrode gap with corresponding neutron converter inserts. The ionization region is between two planar electrodes. Boron-nitride (BN) was chosen as the converter and bulk pieces of BN were machined in various heights for optimizing the detector in terms of maximum electric field strength and absorber area. Table 6.1 lists some properties of BN which made it attractive for this experiment. Natural boron contains a 20% abundance of  $^{10}\text{B}$  which has a relatively high thermal neutron absorption cross section of 3835 barns (see Fig. 6.3).  $^{10}\text{B}$ -n produces lithium and alphas according to



where the excited state of lithium releases a 482 keV photon. The range of  $\alpha$  in BN is only a few microns while the thermal neutron range is more than two orders of magnitude higher which presents the main disadvantage of using the bulk BN absorber.

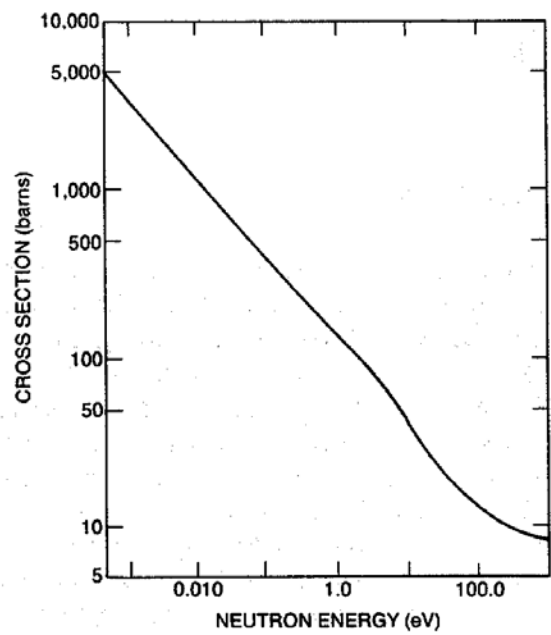


**Figure 6.3:** *Total low energy neutron cross section of boron, from [111]*

---

*high thermal conductivity*

*high electrical resistance*

*easily machined*

*density  $5.1 \times 10^{22}/cc$*

*$^{10}B$  isotopic abundance 20%*

*$^{10}B$  thermal neutron absorption cross section 3835 barns*

*thermal neutron range  $\sim 1$  mm*

---

**Table 6.1:** *Properties of boron nitride*



**Figure 6.4:** *Cryo Industries RC102 continuous flow workstation cryostat*

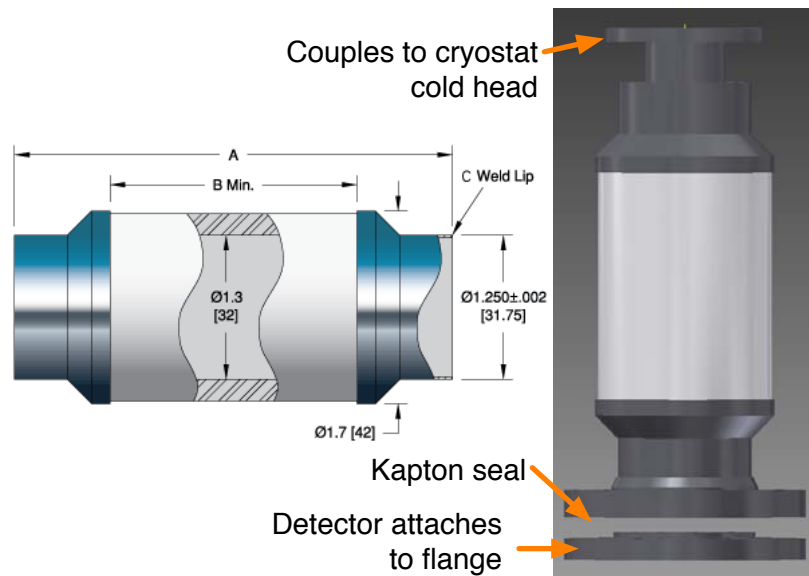


**Figure 6.5:** *Left: CeramTec isolator 17199-02-W with weldable stainless steel ends. Right: Isolator modified for installation into the cryostat with vacuum-tight seals.*

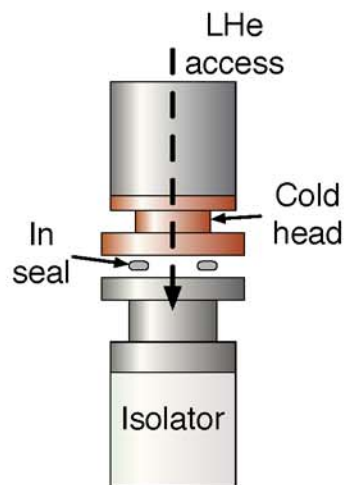


**Figure 6.6:** *Gas and liquid access into the isolator.*

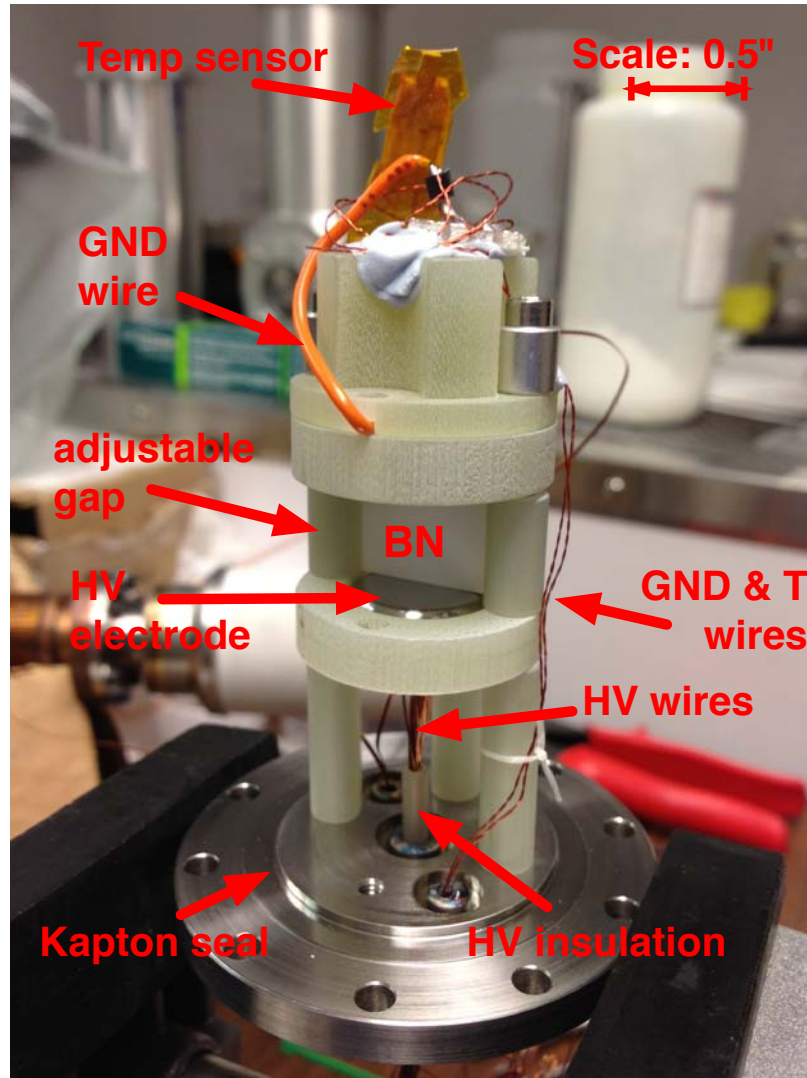


**Figure 6.7:** *Detector G10 assembly mounted to the inside of the bottom isolator flange.*



**Figure 6.8:** *Isolator attached to cryostat with half of the heat shield and vacuum jacket installed. Shown upside down for assembly.*

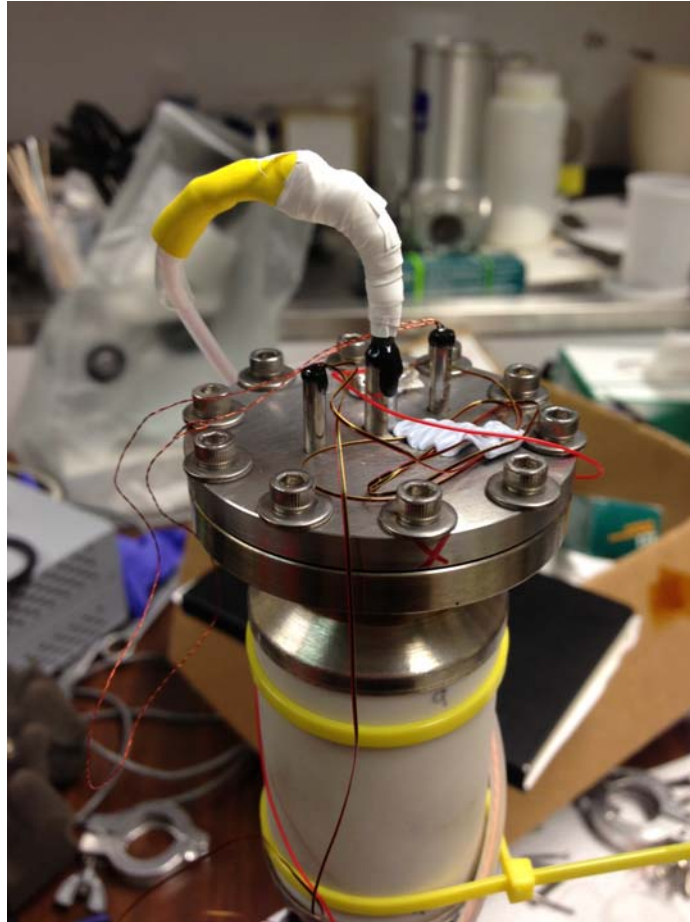


**Figure 6.9:** *Close up wires on isolator flange.*



**Figure 6.10:** *Detector with heat shield installed and wrapped with superinsulation.*



### 6.3 Neutron transmission of ionization cell

Before the isolator could be used in the beam line its neutron transmission needed to be assessed. A  $^3\text{He}$  neutron detector was placed inside the isolator and a second detector placed outside for beam normalization. The setup is shown in Fig. 6.11. After discrimination and amplification the signal was recorded using the MCA card described in the previous chapter and analyzed using Matlab. The MCA card is operated in single channel mode and the sweep interval is determined by the pulse width of LENS. Acquisition is triggered by the proton current  $T_0$  signal and pulses are accumulated for any desired amount of time. The raw transmission data are shown in Fig. 6.12 and Fig. 6.13 shows the ratio of transmitted to incident neutrons.

The ceramic isolator slightly moderates neutrons which is beneficial for the experiment. Slower neutrons spend more time in the vicinity of absorber, increasing the probability of absorption and the detector efficiency can improve as a result. In general, the interaction cross section is inversely proportional to the neutron velocity, this is known as the  $1/v$  trend.

Knowing the transmission capability of the isolator allows for the boron capture rate to be estimated. Figure 6.14 shows the estimated detector rate according to

$$\text{rate} = 0.5 \times 0.2 \times 5.1 \times 10^{22} \times \sigma_{\text{abs}} \times V_{\text{eff}} \times \Phi(v) \times 2200/v \quad (6.2)$$

The factor 0.5 is necessary because emitted  $\alpha$  and Li can only be measured in one hemisphere, 0.2 is the ratio of  $^{10}\text{B}$ ,  $5.1 \times 10^{22}$  the density of BN,  $\sigma$  the thermal absorption cross-section of  $^{10}\text{B}$  which follows the  $1/v$  trend,  $V_{\text{eff}}$  is the effective volume of absorber which takes into account the range of the daughter particles through BN, and finally  $\Phi$  is the neutron flux transmitted through the ceramic. A SRIM [112] calculation was used to estimate the range of  $\alpha$  through BN and found to be approximately 8  $\mu\text{m}$ .

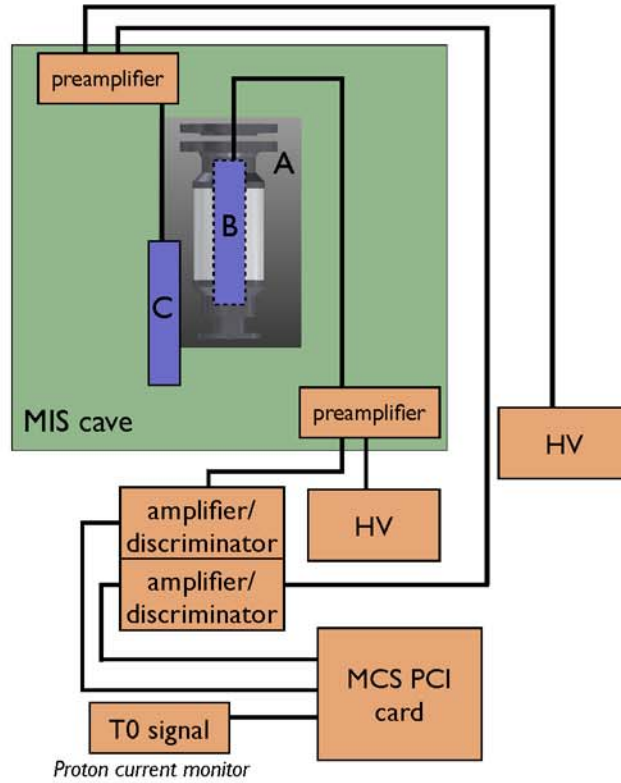


**Figure 6.11:** Setup for the isolator transmission measurement at the MIS beam line. A: ceramic isolator, B: main  $^3\text{He}$  detector, C: monitor  $^3\text{He}$  detector.

Figure 6.14 shows the estimated detector rate with the transmitted neutron flux. Though the estimate is somewhat idealized (not taking into account diffusion, recombination losses and the small solid angle where the entire ionization can be collected) the rate is notably low. This low estimated rate, however, is not inconsistent with measured efficiencies for boron thin film detectors.

The average ranges of  $\alpha$  particles in boron are  $3.6\ \mu\text{m}$  at  $1.47\ \text{MeV}$  and  $4.4\ \mu\text{m}$  at  $1.78\ \text{MeV}$  [113]. The corresponding  $^7\text{Li}$  average ranges are  $1.9\ \mu\text{m}$  at  $0.84\ \text{MeV}$  and  $2.2\ \mu\text{m}$  at  $1.02\ \text{MeV}$ . The authors [113] identified the peak efficiency of a thin film

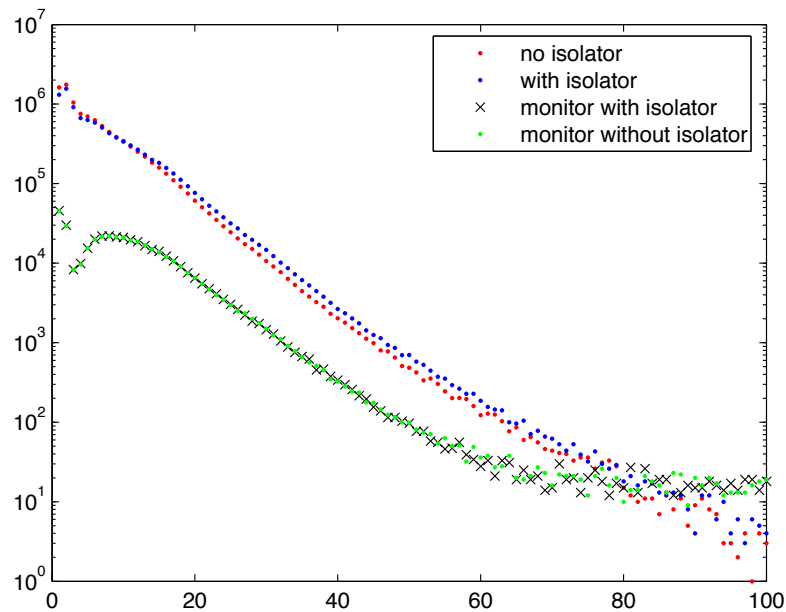


**Figure 6.12:** *Neutron transmission counts with the main  $^3\text{He}$  detector with and without the isolator. The monitor detector shows that there was no beam fluctuation between the cases while the main detector shows a difference in counts.*

enriched boron detector to occur at a thickness near  $3.0\ \mu\text{m}$ , and measured efficiencies of natural boron and enriched boron of just 1% and 5% respectively. The efficiency can be increased substantially by utilizing multiple layers of absorber, in the case of enriched boron around 20 layers. Up to half the efficiency of a  $^3\text{He}$  detector is possible with a layered  $^{10}\text{B}$  detector.

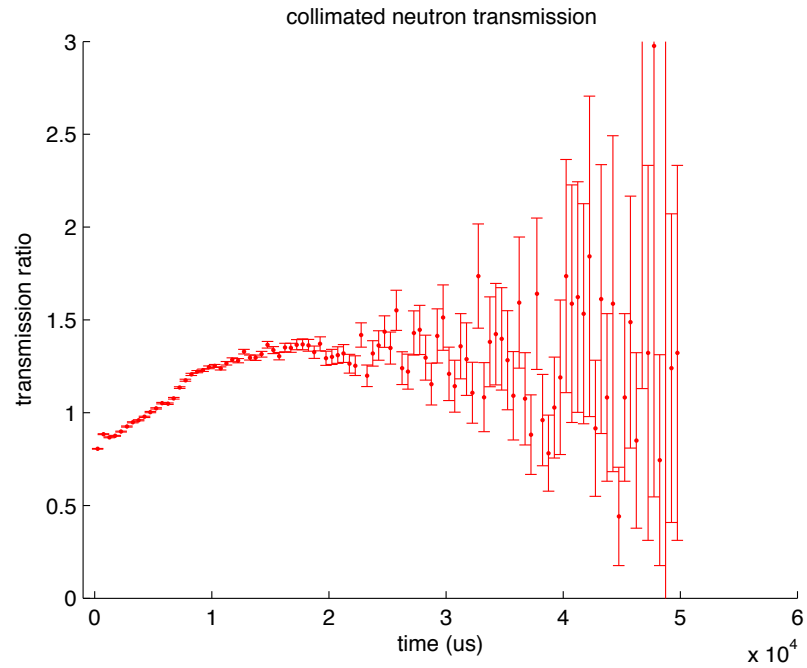


**Figure 6.13:** *Ratio of transmitted to incident neutrons. The ceramic acts as a neutron moderator. The neutrons were pulsed at 20Hz.*

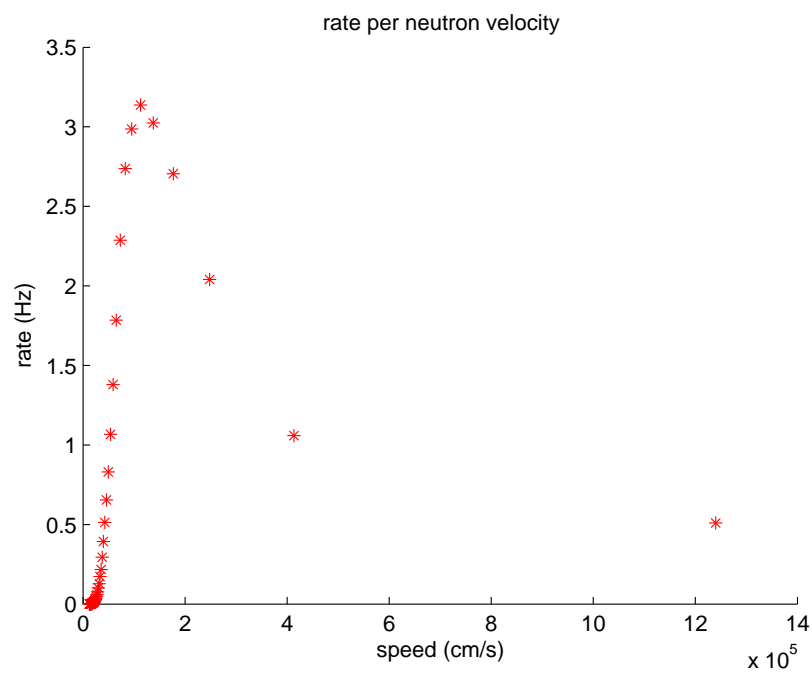


**Figure 6.14:** *Estimated BN detector rate with bulk absorber.*

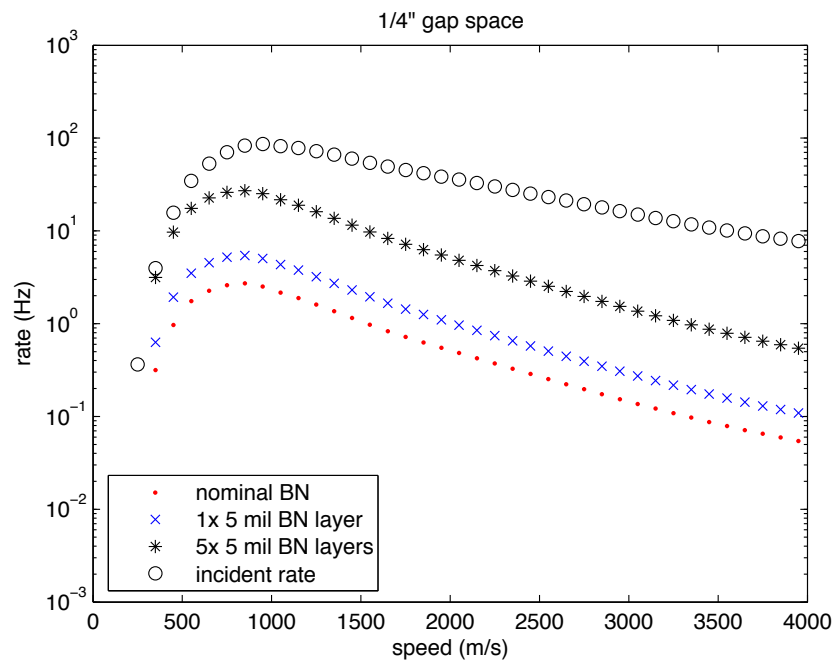


Figure 6.15: *Estimated BN detector rates with layered absorbers.*

## 6.4 Gas-based pulse mode neutron detection

The BN detector was tested using He gas but was unable to hold sufficient pressure to observe pulses. Better results were obtained with Ar gas at 1280 and 1480 Torr. BN absorbers were machined in several thickness (from 0.125" to 0.75") for a variety of possible absorber areas and electrode gaps, the optimal area was found to be between 0.25-0.5". Since the absorbers are held by being sandwiched between the electrodes the thinnest absorbers did not survive and cracked.

Figure 6.16 shows a pulse height distribution with the bulk BN absorber with the neutron beam shutter open and closed. The detection rate was 0.83 Hz and the background rate was 0.06 Hz.

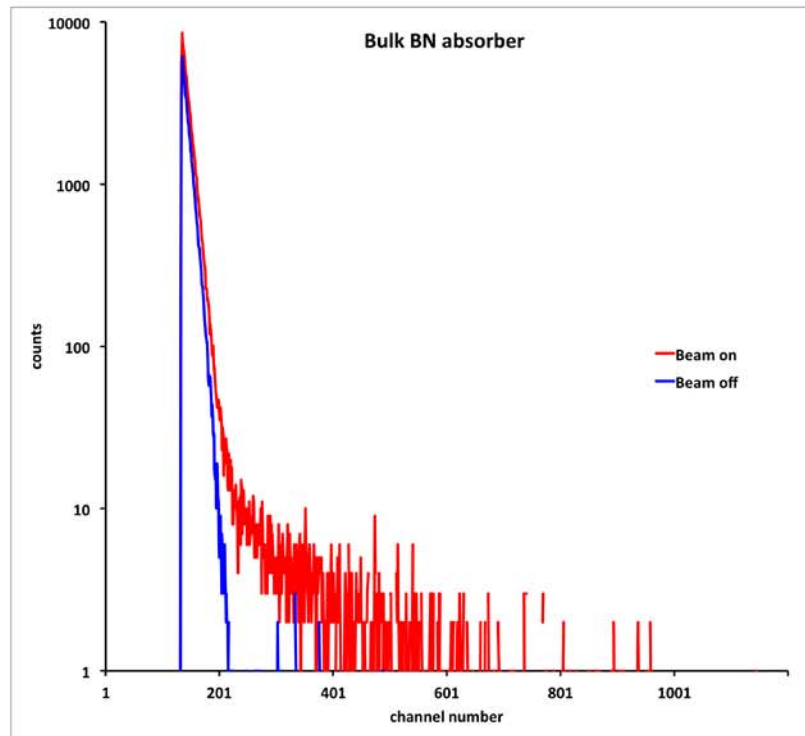
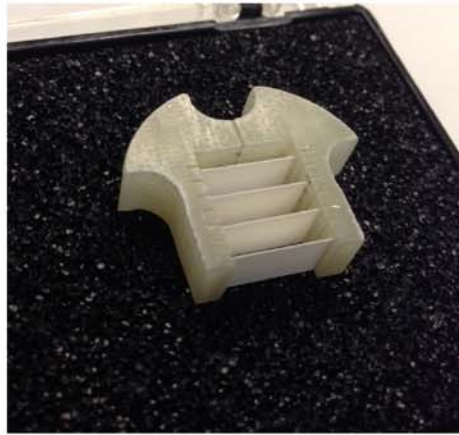


Figure 6.16: *MCA spectrum with bulk BN absorber.*

In an attempt to improve the detection efficiency thin strips of G10 were coated with BN powder. The BN was hand ground with a mortar and pestle and mixed with a few drops of acetone and glue. The mixture was then brushed in thin layers onto G10 sheets 5 mil thick. The coating was found to survive rapid thermal cycling but it was difficult to control the thickness of the coating. For B film detectors the optimal thickness for multi-layer configurations is just a few microns [113]. Figure 6.17 shows the new configuration with four BN planes. The thickness of each BN layer is estimated at a few tens of microns.



**Figure 6.17:** *G10 mount with four BN-coated planes. The neutron beam is normal to the plane surfaces.*

Figure 6.18 shows that the multi-layer approach had a detrimental impact on the detector since no neutron pulses could be detected. Examination of the electric field simulation showed why this could be the case. Figure 6.19 shows a simulation of the detector electrodes with planes of dielectric inside the gap (mimicking the planes of BN-coated G10) using the Ansoft Maxwell software package. A closeup of the small gap between the dielectric and the electrode surface reveals a strong local field which may lead to microdischarges, Fig. 6.20. The disruption in the field lines caused by



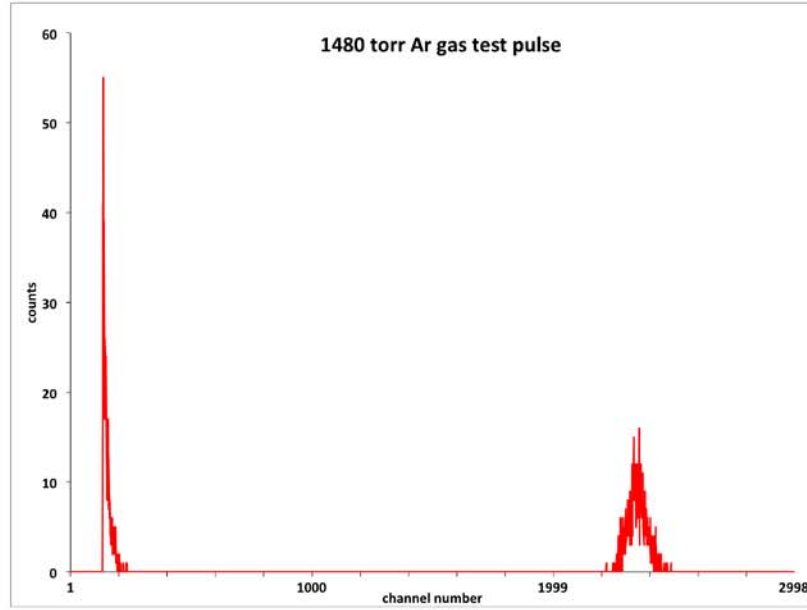


**Figure 6.18:** *MCA spectrum of test pulses in 1480 torr argon gas in MIS beam line with two BN-coated planes in the detector. No neutron pulses were visible.*

the dielectric will also disrupt the trajectories of ionization charges and can be the reason why no pulses were observed in the multi-layer configuration.

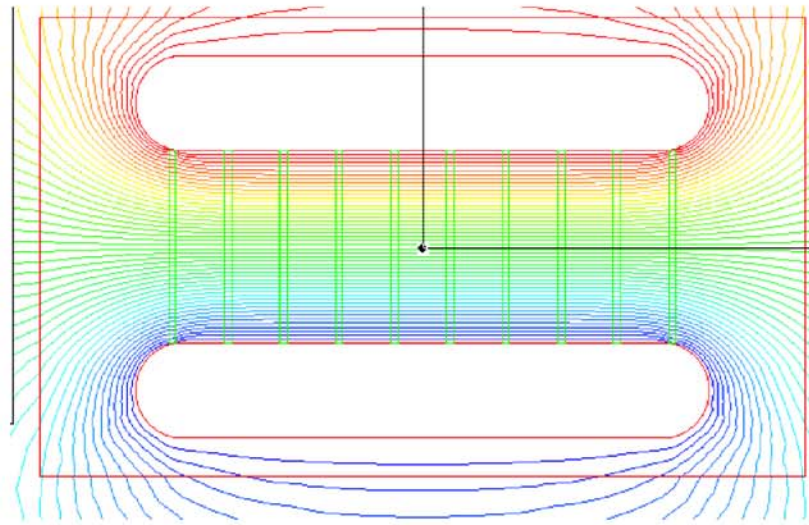


**Figure 6.19:** *Ansoft Maxwell simulation of macroscopic view of electrodes with dielectric planes (in green) inside the gap.*

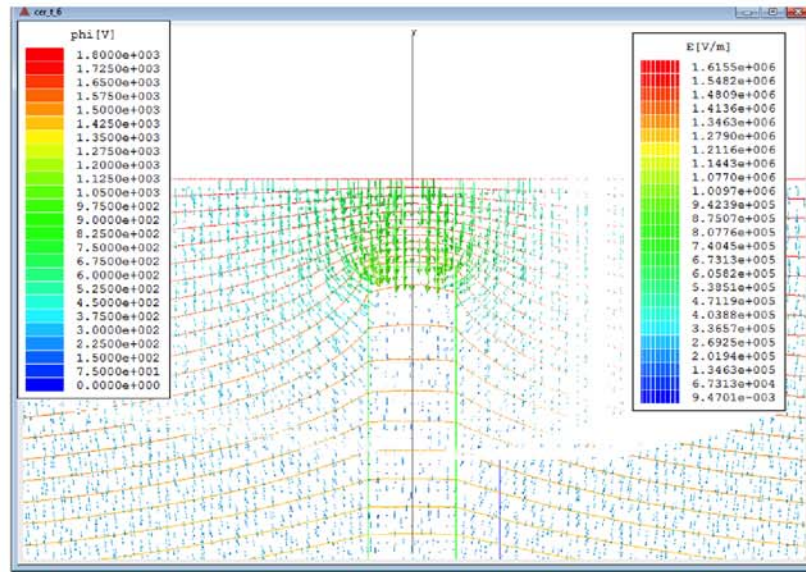


**Figure 6.20:** *Ansoft Maxwell simulation of close up of one dielectric edge (in green) and the small gap between the dielectric plane and electrode surface.*

## 6.5 Liquid-based ionization detection

The use of liquid ionization detectors (LIDs) is not new and their use has been motivated by advantages like much higher density and lower diffusion [93]. A greater concentration of electron-ion pairs also improves the spatial resolution in LIDs. Effective use of LIDs however requires much stricter purity requirements particularly from electronegative contaminants such as oxygen. Traditional media for LIDs have been liquid argon and liquid xenon. Using excellent purity control, it is possible to achieve nearly 100% detector efficiency with proportional mode in liquid xenon [110]. To obtain proportional mode the authors also needed to use exceedingly small wires at  $3.5\text{ }\mu\text{m}$ . The liquid argon calorimeter is the primary LID in regular use for shower detection at high energies [114]. Liquid argon drift [115] and time projection chambers [116] are also in use but require purities better than 1 ppb. Cumbersome cryogenics and often difficult to understand charge transport dynamics have hindered the wider applications of LIDs and there is growing emphasis on room temperature LIDs.

A test of the detector cryostat using the bulk BN sample was performed with liquid nitrogen (LN) at 77 K. While there was no evidence of breakdown inside LN at the voltages tested, and so larger fields could be used than in Ar or He gas, no pulses could be discerned. Figure 6.21 shows the LN-filled cryostat inside the MIS cave. Significant frosting caused leakage and sparking on the high voltage feedthrough and it was necessary to pause the measurement periodically to clean the feedthrough. The noise increased significantly in pulse mode with the introduction of LN, likely due to microphonics from boiling.



**Figure 6.21:** *Detector cryostat filled with liquid nitrogen. Note the abundant frosting which caused a problem with high voltage insulation.*

## 6.6 Discussion & prospects

The most pertinent upgrade to the detector is to forgo BN, with its small concentration of  $^{10}\text{B}$ , and instead use enriched  $^{10}\text{B}$  as is typical for boron detectors. Enriched B powder can be obtained as boron-carbide. While BN is relatively cheap and abundant, enriched B is much more expensive and can be purchased in quantities of at least 100 grams (for around \$ 2000). We were able to obtain about 1 gram of enriched B from LANL. Given the small quantity of available enriched B, all the prototyping

was done with BN until the design could be finalized. Powder enriched B can be applied as a thin layer using powder coating methods. We tested mixing ratios of BN powder, acetone and cyanoacrylate and brush coated strips of G10. Once the optimal mixing ratios, coating thickness and durability were found then samples with the limited quantity of enriched B could be prepared.

A third and most significant redesign of the detector cryostat was planned but numerous setbacks were dealt by repeated problems with LENS equipment. As a result we were unable to have sufficient beam time on LENS in recent months to test the most promising detector upgrades.

The design called for a wire chamber type geometry with a central high voltage wire surrounded by an aluminum cylinder coated with enriched B. A cross section view is shown in figure 6.22. This design carries several important advantages over the planar design:

1. uniform electric field
2. large area of absorber
3. standard wire chamber concept.

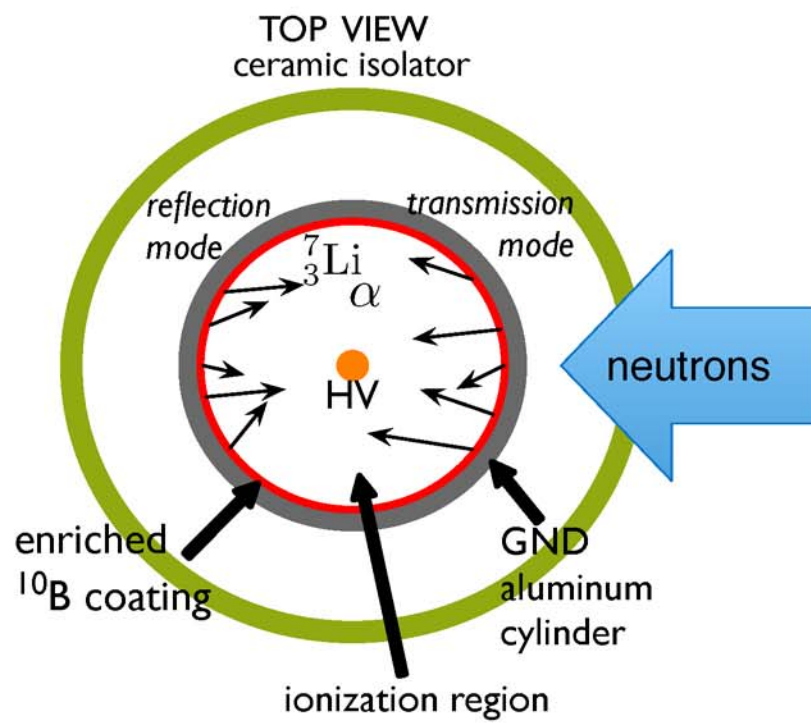


Figure 6.22: *Proposed third generation boron detector.*

## Chapter 7

### Concluding remarks

Research and development for the SNS nEDM experiment are ongoing and the conceptual basis for the experiment, as described in [34], remains promising. The distinguishing features of the SNS nEDM experiment include

- in situ production of ultracold neutrons via superthermal process
- high electric field in He-II
- $^3\text{He}$  co-magnetometer
- $^3\text{He}$  spin analyzer for neutrons
- complementary methods of measuring nEDM signal: free precession and dressed spin.

Here I reported on investigations into the dielectric strength of He-II and a possible third method of measuring the nEDM signal. The motivation for investigating a third method stemmed from the challenges faces by the other methods. For example, the dressing rF field will induce eddy currents in conductors and challenges with maintaining the polarization of  $^3\text{He}$ .



Research in electric field generation remains ongoing with focus on electrode materials. The modular nature of the HV system described in Chapter 4 means that it is well-suited for testing multiple electrode materials with short turnaround. The operation of that system has become systematized and thus inherited by undergraduate researchers. Since the electrodes must be non-metallic (PMMA) and coated with conductive material it is important to test their robustness to thermal cycling and sparking. This consists of measurements of resistivity before and after thermal cycling, measurements of variation of capacitance with temperature (which can indicate flaking off of conductive material) and the ability to maintain high electric fields. Figure 7.1 shows high resolution closeup photos of some of the PMMA electrodes tested in the IU HV system.

Attempts were made to utilize the electron beam evaporator at IU for testing conductive thin films on PMMA. Unfortunately there was no easy way to protect the PMMA from the intense heat of the tungsten filament and hot metallic vapor. Although the evaporator makes extensive use of water cooling (for the source platform, crystal thickness monitor) modifying the water cooling to work the PMMA substrate would be an involved process. Any leaks introduced as a result of the modification would have detrimental effects on the performance of the evaporator apparatus.

A medium scale high voltage system (replacing the large scale system at LANL) coupled to a  $^3\text{He}$  refrigerator has been constructed at LANL, Fig. 7.2. It is capable of testing larger electrodes with adjustable gaps at temperatures comparable to the nEDM experiment (0.4 K) on and off SVP by pressurizing the LHe bath.

Tests of cryogenic light collection have also moved on from small scale to full scale with the intent of demonstrating the generation of a sufficient amount of photoelectrons from neutron capture. In 2009 we demonstrated at IU that the scintillation yield is reduced by about 15% at 50 kV/cm [107] thus it is important to conduct full scale measurements to cross check the loss factors which can impact the viability of

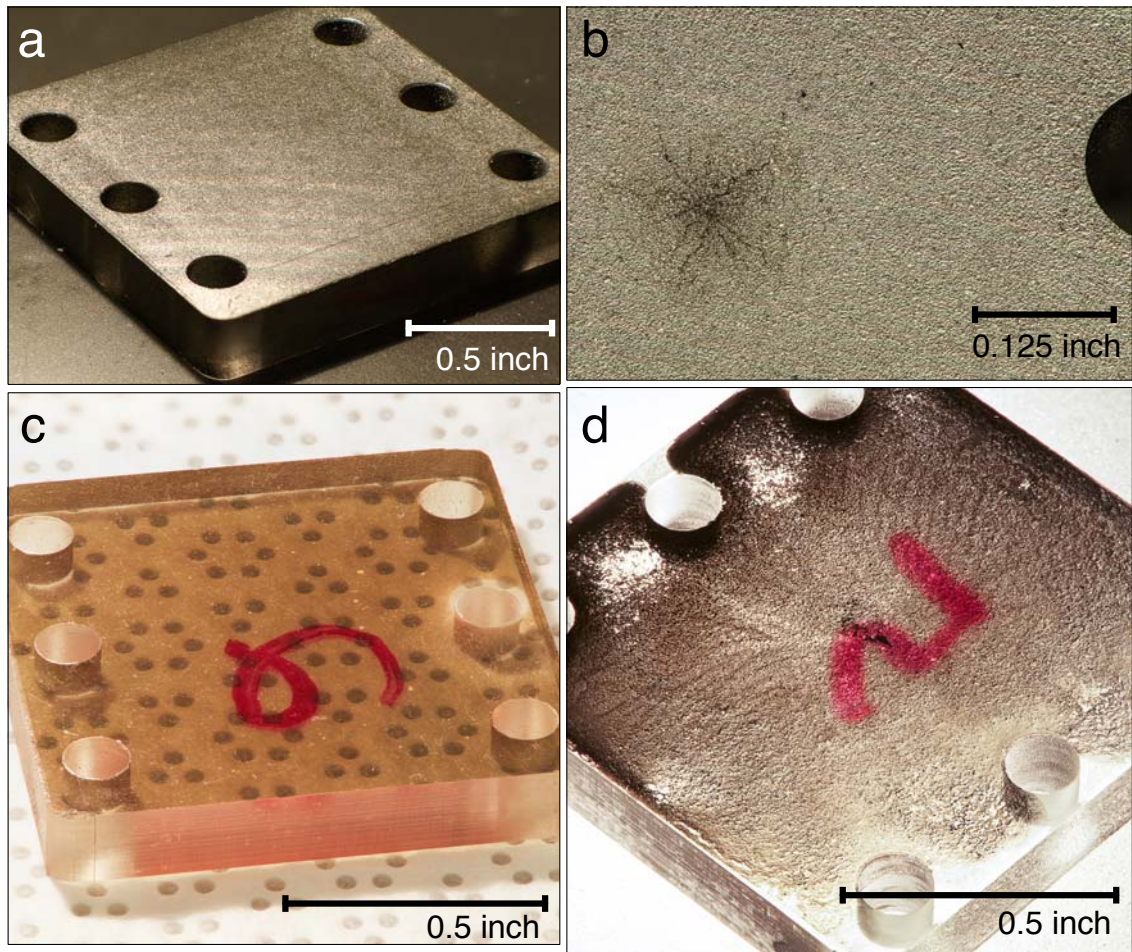


**Figure 7.1:** *High resolution photos of some of the PMMA electrodes tested in small HV system. a) Carbon-coated electrode after thermal cycling in liquid helium. b) Damage to carbon coating from a single spark in superfluid. c) Copper implanted on PMMA. d) PMMA coated with graphite.*

the nEDM signal.

The LHe hysteresis effect first observed in the IU high voltage system caused that experiment to partially branch off from pure nEDM R&D into its own investigation.

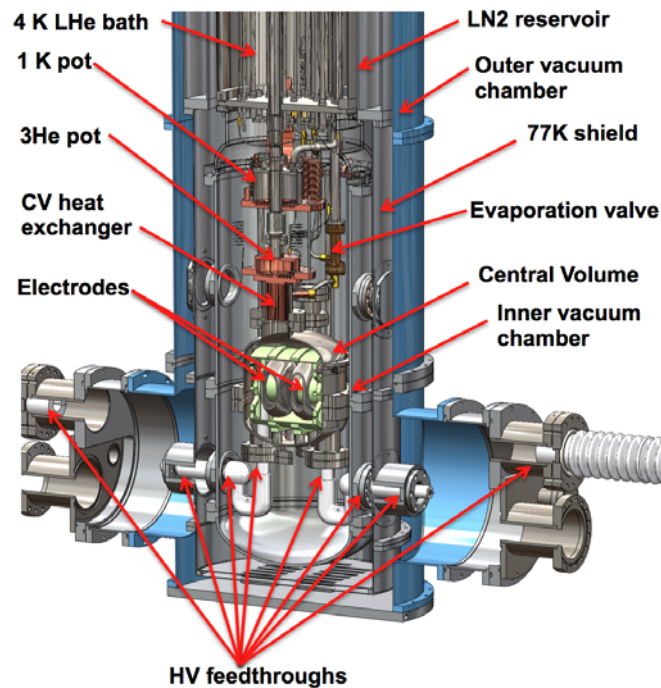


**Figure 7.2:** *Medium scale high voltage test system at LANL.*

Early on during the operation of the experiment we demonstrated the reproducibility of the effect and with each subsequent measurement we were able to eliminate possible sources of misinterpretation. Not surprisingly, the result was met with skepticism by some groups. Detractors seemed to overlook a process fundamental in LHe which is boiling and one fundamental to boiling which is wetting. In the scheme of high voltage these concepts cannot be overlooked. Boiling hysteresis for various liquids has been established long ago so perhaps it should be no surprise that electric breakdown hysteresis is possible.

Some confusion abroad resulted from early breakdown hysteresis data which were made public but without appropriate details. By its very nature, it is difficult to quantify data on electric breakdown and the deduction of boiling hysteresis is largely

phenomenological. Due care should be exercised any time a relatively unexpected and controversial result is observed and we hope during the years the high voltage system was in operation that we have avoided any systematic contamination which could produce apparent hysteresis. It may be that the observed hysteresis occurs only for a limited range of configurations (such as gap size, electrode size, surface roughness) which by coincidence exist in the IU high voltage system. While speculation may continue as to why there should or should not be breakdown hysteresis it will likely remain an open question for some time, but an experiment can be worth a thousand theories. Put another way, the proof of the pudding is in the eating.

Observation of a correlation between the gas Paschen curve and SVP breakdown in LHe combined with the interpretation of the hysteresis result provide fairly strong support for the bubble mechanism of LHe breakdown. The bubble model of liquid breakdown has become more widely accepted as more studies emerge. LHe is a unique system, however, in that it allows one to measure a wide range of pressure dependence of breakdown, ostensibly from 25 bar to near vacuum.

The striking resemblance between the pressure dependence of breakdown in LHe and the pressure dependence in helium gas (viz. Paschen curve) was hard to overlook. Within the bubble model it appears natural that there be some correspondence between breakdown in liquid and the breakdown curve for pure gas. Until now, we have not seen any evidence for this relationship. Perhaps the reason for this has to do with the utility of LHe (liquid in the limit  $P \rightarrow 0$ ) and costs incurred when working with LHe spurred by dwindling helium supplies. Few groups have the means to carry out breakdown studies in LHe for their own sake. Instead, as in this investigation, they tend to be corollary to larger projects and few large projects have need of LHe breakdown studies.

That is not to say that studies of breakdown in LHe are without consequence or practical application. Indeed the apparent confirmation of the bubble mechanism of

breakdown in LHe, and hysteresis in particular, raises new questions. Electric field-induced nucleation is used to assess the boundary of stability of liquids. The effect of electric fields on metastable systems is also an active area of research. LHe has seen widespread application in superconducting magnets.

Studies with boiling in mixtures of  $^3\text{He}/^4\text{He}$  showed that the stability of bubbles was improved with higher  $^3\text{He}$  fractions [117]. In those studies only the  $^4\text{He}$  component was in the superfluid state. It is not known what, if any, effect do varying fractions of He-I have on vapor bubbles in He-II.

Techniques based on the suppression of heterogeneous nucleation and improving wetting have seen recent focus in experimental searches for dark matter. For example, bubble chamber detectors for Weakly Interacting Massive Particles need superheated metastable liquids where a first order phase transition would indicate a detector event [118].

# References

- [1] H. Weyl, *Symmetry*. Princeton University Press, 1952.
- [2] M. Sozzi, *Discrete Symmetries and CP Violation*. Oxford University Press, 2008.
- [3] I. I. Bigi and A. I. Sanda, *CP Violation*. Cambridge University Press, 2009.
- [4] T. D. Lee and C. N. Yang *Phys. Rev.* *104*, 254, 1956.
- [5] C. S. Wu *et al.* *Phys. Rev.* *105*, 1413, 1957.
- [6] T. D. Lee, R. Oehme, and C. N. Yang *Phys. Rev.* *106*, 340, 1957.
- [7] A. Angelopoulos and others CPLEAR *Phys. Lett. B* *444*, 43, 1998.
- [8] F. Halzen and A. Martin, *Quarks and Leptons*. John Wiley and Sons, Inc., 1984.
- [9] A. D. Sakharov *Pis'ma Zh. Eksp. Teor. Fis.* *5*, 1967.
- [10] M. Pospelov and A. Ritz *Annals of Physics*, *318*, 2005.
- [11] E. M. Purcell and N. F. Ramsey *Phys. Rev.* *78*, 807, 1950.
- [12] A. Czarnecki and W. J. Marciano, *Lepton Dipole Moments*. World Scientific Publishing Company, 2009.

- [13] J. M. Pendlebury and E. A. Hinds *Nucl. Instr. Meth. A*, 440, 2000.
- [14] J. H. Christensen *et al. Phys. Rev. Lett.* 13, 138, 1964.
- [15] I. B. Khriplovich and S. K. Lamoreaux, *CP-Violation Without Strangeness*. Springer, 2004.
- [16] B. Aubert and others [BaBar Collaboration] *Phys. Rev. Lett.* 87, 091801, 2001.
- [17] K. Abe and others [Belle Collaboration] *Phys. Rev. Lett.* 87, 091802, 2001.
- [18] S. K. Lamoreaux and R. Golub *J. Phys. G: Nucl. Part. Phys.* 36, 104002, 2009.
- [19] J. H. Smith, E. M. Purcell, and N. F. Ramsey *Phys. Rev.* 108, 120, 1957.
- [20] N. F. Ramsey, *Molecular Beams*. Oxford University Press, 1956.
- [21] P. D. Miller *et al. Phys. Rev. Lett.* 19, 381, 1967.
- [22] C. G. Schull and R. Nathans *Phys. Rev. Lett.* 19, 384, 1967.
- [23] C. G. Schull *Phys. Rev. Lett.* 10, 297, 1963.
- [24] W. B. Dress *et al. Phys. Rev.* 170, 1200, 1968.
- [25] J. K. Baird *et al. Phys. Rev.* 179, 1285, 1969.
- [26] W. B. Dress, P. D. Miller, and N. F. Ramsey *Phys. Rev. D* 7, 3147, 1973.
- [27] W. B. Dress *et al. Phys. Rev. D* 15, 9, 1977.
- [28] Y. B. Zel'dovich *Zh. Eksp. Theor. Fiz.* 36, 1952 (*Sov. Phys. JETP* 9, 1389, 1959).
- [29] R. Golub, D. Richardson, and S. K. Lamoreaux, *Ultra-Cold Neutrons*. Taylor & Francis Group, 1991.

- [30] K. F. Smith *et al.* *Phys. Lett. B* 234, 191, 1990.
- [31] I. S. Altarev *et al.* *Phys. Lett. B* 276, 242, 1992.
- [32] C. A. Baker *et al.* *Phys. Rev. Lett.* 97, 131801, 2006.
- [33] J. H. Christenson, J. W. Cronin, and R. T. W. L. Fitch *Phys. Rev. Lett* 13, 138, 1964.
- [34] R. Golub and S. K. Lamoreaux *Physics Reports*, 237, 1, 1994.
- [35] V. A. Dzuba, V. V. Flambaum, and J. S. M. Ginges *Phys. Rev. A* 76, 034501, 2007.
- [36] “Conceptual design report for the nedm project.”  
<http://www.phy.ornl.gov/nedm/>.
- [37] M. B. (Ed.), *CP Violation in Particle, Nuclear and Astrophysics (Lecture Notes in Physics)*. Springer, 2002.
- [38] J. C. Long *et al.* *arXiv:physics/0603231*, 2006.
- [39] F. Pobell, *Matter and Methods at Low Temperatures*. Springer-Verlag, 2007.
- [40] V. P. Carey, *Liquid-Vapor Phase Change Phenomena*. Taylor and Francis Group, 2008.
- [41] L. I. Dana and H. K. Onnes *Leiden Commun.* 190b, *Proc. Roy. Acad. Sci. Amsterdam* 29, 1061, 1926.
- [42] W. H. Keesom and K. Clusius *Leiden Commun.* 219e, *Proc. Roy. Acad. Sci. Amsterdam* 35, 307, 1932.
- [43] C. Enss and S. Hunklinger, *Low-Temperature Physics*. Springer-Verlag, 2005.



- [44] P. Kapitza *Nature* 141, 74, 1938.
- [45] J. F. Allen and A. D. Misener *Nature* 141, 75, 1938.
- [46] F. London *Nature* 141, 643, 1938.
- [47] L. Tisza *Nature* 141, 913, 1938.
- [48] E. Kuffel, W. S. Zaengl, and J. Kuffel, *High Voltage Engineering*. Butterworth-Heinemann, 2000.
- [49] M. S. Naidu and V. Kamaraju, *High Voltage Engineering*. McGraw-Hill, 1996.
- [50] A. Y. Sonin *Tech. Phys. Lett.* 32, 3, 2006.
- [51] P. Hartmann *et al.* *Plasma Sources Sci. Technol.* 9, 2000.
- [52] F. M. Penning *Proc. R. Acad. Amst.* 34, 1305, 1931.
- [53] S. W. V. Sciver, *Helium Cryogenics*. Springer, 2012.
- [54] M. Blander and J. L. Katz *AIChE Journal*, 21, 5, 1975.
- [55] H. J. Maris *C. R. Physique*, 7, 9, 2006.
- [56] S. F. Jones, G. M. Evans, and K. P. Galvin *Adv. in Colloid and Interface Science*, 80, 1, 1999.
- [57] R. H. S. Winterton *J. Phys. D: Appl. Phys.* 10, 1977.
- [58] J. P. Gallagher and R. H. S. Winterton *J. Phys. D: Appl. Phys.* 16, 1983.
- [59] J. P. Gallagher and R. H. S. Winterton *J. Phys. D: Appl. Phys.* 18, 1985.
- [60] “Mag and aluminum polish from: Mothers polish.”

- [61] “Proprietary electropolishing service provided by: Able electropolishing co. inc.”
- [62] “Electropolishing.” <http://en.wikipedia.org/wiki/Electropolishing>.
- [63] P. Carazzetti and H. R. Shea *J. Micro/Nanolith., MEMS, MOEMS*. 8, 3, 2009.
- [64] A. Béréal *J. Appl. Phys.* 73, 9, 1993.
- [65] K. C. Kao and J. P. C. McMath *IEEE Trans. Elect. Insul. EI-5*, 3, 1970.
- [66] J. Qian *et al. J. Appl. Phys.* 97, 113304, 2005.
- [67] R. P. Joshi *et al. J. Appl. Phys.* 96, 9, 2004.
- [68] D. Lohse *Physics Today*, Feb, 2003.
- [69] T. P. Hong *et al. IEEE Electrical Insulation and Dielectric Phenomena Annual Report*, 2000.
- [70] M. Hara *et al. Research Reports on Information Science and Electrical Engineering of Kyushu University*, 3, 1, 1998.
- [71] W. F. Schmidt *et al. Proceedings of 2002 IEEE 14th International Conference on Dielectric Liquids*, 2002.
- [72] M. Hara *et al. Research Reports on Information Science and Electrical Engineering of Kyushu University*, 3, 1, 1998.
- [73] C. Blank and M. H. Edwards *Phys. Rev.* 119, 1, 1960.
- [74] M. Hara *et al. IEEE Trans. on Dielectrics and Electrical Insulation* 10, 6, 2003.
- [75] P. Taborek and L. Senator *Phys. Rev. Lett.* 57, 2, 1986.

- [76] J. Dupont-Roc *J. Low Temp. Phys.* 126, 1/2, 2002.
- [77] K. S. Ketola, S. Wang, and R. B. Hallock *Phys. Rev. Lett.* 62, 2, 1992.
- [78] D. Ross, P. Taborek, and J. E. Rutledge *Journal of Low Temperature Physics* 111, 1/2, 1998.
- [79] J. Klier *et al.* *Phys. Rev. B* 72, 245410, 2005.
- [80] K. T. A. L. Burm *Contrib. Plasma Phys.* 47, 3, 2007.
- [81] J. Gerhold and M. Hubmann *11th International Conference on Gas Discharges and Their Applications*, 1995.
- [82] J. Gerhold *Cryogenics*, 38, 1998.
- [83] B. Fallou, J. Galand, and B. Bouvier *Cryogenics* 10, 2, 1970.
- [84] J. Suehiro *et al.* *Conference Record of the ICDL 1996, 12th International Conference on Conduction and Breakdown in Dielectric Liquids*, 1996.
- [85] M. Hara *et al.* *Conference Record of the ICDL 1996, 12th International Conference on Conduction and Breakdown in Dielectric Liquids*, 1996.
- [86] J. Suehiro *et al.* *IEEE Trans. on Dielectrics and Electrical Insulation* 3, 4, 1996.
- [87] E. J. Langham and B. J. Mason *Proc. of the Royal Society of London A.* 247, 1251, 1958.
- [88] J. Kestin, *A Course in Thermodynamics*. Blaisdell Publishing Company, 1966.
- [89] G. K. Batchelor, *An Introduction to Fluid Dynamics*. Cambridge Mathematical Library, 2000.

- 
- [90] M. Cooper, “Electric dipole moment of the neutron,” <http://library.lanl.gov/cgi-bin/getfile?30-26.pdf>.
- [91] G. F. Knoll, *Radiation Detection and Measurement*. Wiley & Sons, 2000.
- [92] W. Blum, W. Riegler, and L. Rolandi, *Particle Detection with Drift Chambers*. Springer, 2008.
- [93] W. R. Leo, *Techniques for Nuclear and Particle Physics Experiments*. Springer, 1994.
- [94] A. C. Melissinos and J. Napolitano, *Experiments in Modern Physics*. Academic Press, 2003.
- [95] R. C. Fernow, *Introduction to Experimental Particle Physics*. Cambridge University Press, 1986.
- [96] A. F. Borghesani, *Ions and Electrons in Liquid Helium*. Oxford University Press, 2007.
- [97] J. Classen *et al.* *Phys. Rev. B.* *57*, 5, 1998.
- [98] L. D. Landau *J. Phys. USSR*, *5*, 71-90, 1941.
- [99] D. G. Henshaw and A. D. B. Woods *Phys. Rev.* *121*, 1266, 1961.
- [100] H. Gunther *et al.* *Fizika Nizkikh Temperatur* *22*, 2, 1996.
- [101] G. Careri *et al.* *Phys. Rev. Lett.* *15*, 9, 1965.
- [102] T. Ellis *et al.* *Phil. Trans. Roy. Soc.* *296*, 581, 1980.
- [103] W. I. Glaberson and W. W. Johnson *J. Low Temp. Phys.* *20*, 313, 1975.
- [104] F. Ancilotto, M. Barranco, and M. Pi *Phys. Rev. B.* *82*, 014517, 2010.

- 
- [105] K. W. Schwarz and R. W. Stark *Phys. Rev. Lett* **21**, 14, 1968.
- [106] A. Kent, *Experimental Low-Temperature Physics*. American Institute of Physics, 1993.
- [107] T. M. Ito *et al.* *Phys. Rev. A* **85**, 042718, 2012.
- [108] L. G. H. Huxley and R. W. Crompton, *The Diffusion and Drift of Electrons in Gases*. Wiley, New York, 1974.
- [109] H. Tanuma *et al.* *J. Chem. Phys.* **113**, 5, 2000.
- [110] R. A. Muller *et al.* *Phys. Rev. Lett.* **27**, 8, 1971.
- [111] D. I. Garber and R. R. Kinsey *Brookhaven National Laboratory report BNL 325*, 1976.
- [112] “The stopping and range of ions in matter simulation software.”  
<http://www.srim.org/>.
- [113] Z. Wang and C. L. Morris *Nucl. Instr. Meth. A*, **652**, 2011.
- [114] W. J. Willis and V. Radeka *Nucl. Instr. and Meth.* **120**, 221, 1974.
- [115] W. A. Huffmann, J. M. LoSecco, and C. Rubbia *IEEE Trans. Nucl. Sci NS-26*, **64**, 1979.
- [116] P. J. Doe, H. J. Mahler, and H. H. Chen, “The liquid argon time projection chamber,” *AIP Conf. Proc. No. 108*. AIP New York, 1984.
- [117] H. Abe *et al.* *J. Fluid Mech.* **619**, 2009.
- [118] “Chicagoland observatory for underground particle physics.”  
<http://www-coupp.fnal.gov/>.

# Maciej Karcz

Indiana University  
Center for Exploration of Energy and Matter  
2401 N Milo B. Sampson Lane Bloomington, IN 47408  
Tel: 847-477-2378 (cell)  
Email: *MKARCZ@indiana.edu*

## Education

DEGREE	MAJOR	INSTITUTION
Ph.D. (2014)	Physics	Indiana University, Bloomington
M. S. (2008)	Physics	Indiana University, Bloomington
B. S. (2006)	Theoretical Physics/Applied Mathematics	Loyola University Chicago

## Awards & Honors

- Travel Award, International Nuclear Physics Conference, Vancouver, 2010
- Departmental Honors, Physics Dept., Loyola, 2006
- Dougherty Research Award, Physics Dept., Loyola, 2006
- Mulcahy Research Scholar Award, Loyola, 2005-2006
- Mulcahy Research Scholar Award, Loyola, 2003-2004
- Fr. Gerst Memorial Award for Excellence in Physics, Loyola, 2003
- Pacific Northwest National Laboratory Summer Fellowship, 2003
- Presidential Scholarship, Loyola, 2002-2006
- Dean's List Recognition, eight semesters, Loyola

## Research Experience

- Indiana University, R&D for the SNS nEDM Experiment (Research Associate, 2007-2014)

- Loyola University, undergraduate research (2005-2006)
- Indiana University, REU (2005)
- Loyola University, undergraduate research (2003-2005)
- Loyola University and Pacific Northwest National Laboratory, undergraduate research (2003)
- United States Particle Accelerator School, San Francisco (Associate Instructor, 01/2010)
- Indiana University, Bloomington (Associate Instructor, 08/2006–12/2008)